A Gas Emission Setup to Evaluate Wideband Sub-mm Spectrometers

For Frequency Calibration and Long Integration Analysis

M.J. Gouwerok

Delft University of Technology

TU Delft

A Gas Emission Setup to Evaluate Wideband Sub-mm Spectrometers

For Frequency Calibration and Long Integration Analysis

by

M.J. Gouwerok

to obtain the degree of Master of Science
at the Delft University of Technology,
to be defended publicly on Thursday, September 30, 2021 at 10:00 AM.

Student number:	4382242	
Project duration:	November 23, 2020 – September 30, 2021	
Thesis committee:	Dr. K. Karatsu,	TU Delft, supervisor
	Dr. A. Endo,	TU Delft
	Prof. dr. ir. J.J.A. Baselmans,	TU Delft
	Dr. A.J.L. Adam	TU Delft

An electronic version of this thesis is available at `http://repository.tudelft.nl/`.

Cover image: The interacting galaxy system IC1623, or VV114, located about 300 million light-years away. The two galaxies are merging, and are very bright in the infrared spectrum. The system has been used for first light observations of the DESHIMA prototype. Credit: NASA, ESA, the Hubble Heritage Team (STScI/AURA)-ESA/Hubble Collaboration and A. Evans (University of Virginia, Charlottesville/NRAO/Stony Brook University)

TU Delft

Preface

Welcome to this thesis. The work presented here focusses on a gas emission setup to evaluate wideband submillimeter spectrometers. The need for such a setup is motivated by the desire for a full laboratory assessment of the DESHIMA instrument. The DESHIMA instrument is a new type of spectrometer for astronomical observations which employs microwave kinetic inductance technology. The motivation for DESHIMA and the gas emission setup is further described in the introduction chapter.

It was an insightful experience to dive deep into a subject with only a broad understanding at first. The combination of nanotechnology with astronomy, and the enthusiasm of the group, motivated me to start this research. Among many subjects, the research covered the physics of optical resonance, the analysis of noise, and the workings of microwave kinetic detectors. I experienced first hand the challenges of experimental work, including the importance of reproducible results and the difficulty in aligning optical systems. More than I expected, I thoroughly enjoyed learning about the endless possibilities and open-source packages with programming in Python. However, probably the most valuable lesson I got to embrace during this work is not included in the rest of this thesis. It was the insight that any piece of information, even when seemingly impossibly difficult at first, can be understood when taking the time for it to sit down and read it carefully. This showed to be a valuable catalyst for taking in new knowledge, which I hope to take with me to new challenges in the future.

It has been an interesting year. My expectations were to experience research in the academia among experienced members. To both learn about a career in research, alongside performing research. Unfortunately, the work was mainly done from home due to the pandemic. This reduced the opportunities for contact and low-key sparring about new findings and insights, which I normally enjoy and value. Nevertheless, I learned more than I would have anticipated and look back on a valuable educational time that led to the work presented here.

One of the highlights during the project was the opportunity to join the 19th International Workshop on Low Temperature Detectors, organized by NIST. It was an insightful experience to view the work of similar groups all over the globe, and to talk to other researchers. I got to present and discuss my intermediate results, which lead to some new insights into my own work.

On a final note in this preface, I would like to thank the MKID subgroup of the Terahertz Sensing Group for their pleasant (digital) workplace and enjoyable meetings. Especially, I would like to thank Kenichi for the daily supervision and interesting conversations whenever I encountered a challenging issue during my research.

I spent quite some time and energy on the work presented here, and hope you enjoy it, learn from it, and are able to use it in your future work.

M.J. Gouwerok
Delft, September 2021

Abstract

A gas-cell-based calibration setup was designed to evaluate the wideband response of sub-millimeter spectrometers like DESHIMA (DEep Spectroscopic High-redshift MApper). The use of low pressure gas emission spectra allowed for accurate calibration of the absolute frequency response, and to test the detectability of faint emission spectra with long integration times. This is important to understand and evaluate systematic errors and noise profiles of sub-millimeter astronomical spectrometers before their telescope campaigns.

The setup consisted of a low pressure (~mbar) gas at room temperature in a high vacuum ($<10^{-3}$ mbar) chamber in front of a 77K N_2 background. A double-winged rotating chopper was used for signal modulation of the on- and off-source paths to reduce the low-frequency noise profile. The setup has been able to successfully detect the emission spectra of nitrous oxide at 30 mbar and methanol at 1 mbar in the frequency range of 332 to 377 GHz with the prototype DESHIMA spectrometer. Our models showed that lower pressures should be detectable over similar averaging times. The standing spectrum showed to be too irregular for detecting spectral lines in a single measurement. A second measurement was required to subtract the standing features, which extended the total time required beyond the current system stability.

Detailed analysis into optical resonances has shown the importance of anti-reflective (AR) coatings on the main optical interfaces to improve the detectability of the emission spectra. We adapted sub-wavelength pyramid gratings milled into TOPAS windows to reduce a standing wave in the output spectrum of the gas cell setup. Stability of the setup was shown for observation times of up to $\sim 10^3$ seconds before environmental noises became dominant. Extensive stability testing has shown the impact of key components in the setup. A two-stage post-processing algorithm was developed to successfully reduce instabilities in the data by removing linear drifts and by removing the common profile over simultaneous read-out data.

Keywords: Evaluation of sub-millimeter detectors, optical resonance in light spectrometry, frequency stability analysis, DESHIMA

Contents

1 Introduction

To understand the history of our universe, it is of great interest to investigate and trace back the evolution of current day celestial objects. The origin and evolution of objects such as galaxies and their stars can be used to validate and inspire the theoretical models we have today. Since radiation from celestial objects reaching us is limited by the speed of light, we can look back in time depending on the distance between a celestial object and us. Every frequency band of radiation one can observe from the universe shows different processes happening. Each band requires different techniques for detecting the radiation at desired sensitivities, requiring a wide range of detectors for astronomical observations.

In October 2017 at a high altitude plateau in Chile, the first-light observation by DESHIMA was performed on Saturn. DESHIMA combines multiple superconducting microwave inductance detectors (MKID) on a single superconducting chip to detect spectra in the far infrared range. Combining MKID technology with astronomy allowed for unprecedented wideband instantaneous spectroscopy on this part of the electromagnetic radiation of the universe. The sub-millimeter band where DESHIMA is focused on is especially interesting for the formation of stars. Current research and development is focused on DESHIMA 2.0 to obtain scientifically competitive observations to better understand the origins of galaxies and stars.

To obtain the best results with on-site measurements, a range of calibration measurements are required to understand and optimize the instrument performance. This research is concerned with one of such calibration measurements, a gas cell setup to detect low pressure gasses. By using gas emission spectra, one can accurately determine the frequency response and offsets, and test the detectability of low pressure emission spectra. This work continues on the gas cell setup by Zhang [63], who developed a setup capable of detecting an overall frequency offset, but with several challenges limiting the full potential of a gas emission measurement setup for DESHIMA. This work addresses those challenges to improve the effectiveness of the setup to evaluate DESHIMA or sub-millimeter detectors alike.

The next section will cover the scientific motivation of the DESHIMA detector and the motivation for the gas emission measurement. This thesis will continue along the conventional research report outline of theory, methods, and results. The theory chapter aims to give the reader a concise but full overview of the theoretical concepts behind the DESHIMA instrument and the stability of the gas emission setup. The gas emission setup and the data-processing algorithms are described in detail in the experimental setup and data processing chapters. The performance of the gas emission setup as an evaluation tool for sub-millimeter spectrometers is reviewed in the results and discussion chapter. The current limits of the setup and the impact of several key components are analysed in detail. The conclusion chapter brings all other chapters together to summarize the main findings. In the concludion, the limits of the presented gas emission setup for evaluation of sub-millimeter detectors are discussed. Several suggestions for further research are given to improve the setup and its ability to evaluate detectors for longer integration times.

The presented work in this dissertation was done as part of the final thesis project to obtain the degree of Master of Science in Applied Physics at the Experimental Astronomy research group, part of Terahertz Sensing at the Delft University of Technology.

1.1. Scientific Motivation for DESHIMA

The space inside a galaxy in between stars is filled with matter and called the interstellar medium. Once the density in a region of the interstellar medium is sufficiently high, molecules start to form. These regions of high density are called molecular clouds. If the mass of a molecular cloud reaches a certain limit, the Jeans limit, it collapses under its own gravitational force. This collapse results in a cluster of new stars. The dust particles, chemical components, and reactions during this collapse and star forming process are absorbent of mainly ultraviolet to optical light and emitting far infrared to microwave light. The development of sub-millimeter detectors is therefore of interest to investigate the processes related to the formation of stars.

1.1.1. Sub-millimeter Wave Detection of Star Formation

The typical spectral lines originating from interstellar matter have been accurately measured. By analysing the redshift of expected spectral lines in the observations of far away objects, one can estimate the age of the respective radiation.

Ionized Gas, Molecular Clouds and Spectral Lines

Large clouds of ionized gasses can be found in the interstellar medium. These clouds are well detectable in the sub-millimeter range, as several spectral lines of the abundant carbon, nitrogen, and oxygen ions have clear spectral lines. Especially the CII, OI and OIII lines are bright lines indicative of galaxies [49].

Denser regions where molecules start to form are typically indicative of early star formation. Dihydrogen (H_2) and carbon monoxide (CO) are the first and second most abundant molecules in molecular clouds. The spectral lines of H_2 are typically hard to detect, as the radiative transitions are weak due to a lack of dipole moment. Furthermore, the emitted photons are in the ultraviolet range and are easily absorbed by other matter present before reaching the observer on Earth. Although less abundant, the spectral lines due to the rotational transitions of CO are bright and well detectable at microwave frequencies. Therefore, the presence of CO is primarily used to detect and inspect molecular clouds [22].

Redshift and Cosmic Time

Due to the intrinsic expansion of the universe, all space is scaled at a rate described by Hubble's law. Hubble's law is typically expressed as

$$v = H_0 D \tag{1.1}$$

where v is the recessional velocity (the effective velocity between source and observer), H_0 is the Hubble parameter at the time of measurement and D the proper distance between the observer and source. Note that both H_0 and D are dependent on the cosmic time and are to be taken at the same time. For electromagnetic radiation travelling over cosmological distances through expanding space, the wavelength observed is expanded relative to the wavelength emitted. This expansion is characterized as

$$z = \frac{\lambda_{observed}}{\lambda_{emitted}} - 1 = \frac{v_{rs}}{c} \sim \frac{v}{c} \tag{1.2}$$

where the redshift parameter z is defined as the expansion in the observed wavelength $\lambda_{observed}$ relative to the original emitted wavelength $\lambda_{emitted}$, which can also be represented as the redshift velocity v_{rs} relative to the speed of light c. The redshift velocity is approximately equal to the recessional velocity for small redshift $z \ll 1$, but for larger redshifts the relation is nonlinear and dependent on the describing model used [12]. Since the redshift can be related to an elapsed period in cosmic time, it is a crucial parameter in describing the history of the universe. The detected redshift of a celestial object can be correlated to the approximate cosmic age of the object.

Limitations of Today's Sub-millimeter Detectors

The evolutionary processes related to star formation are typically found in the redshift range $z+1 \sim$ 1-10 [18]. Therefore, the spectral lines of a molecular cloud of unknown redshift can be in a wide band of the sub-millimeter spectrum. For example, the CII spectral line at 158μm ($\sim$ 1.9 THz) could end up at observed wavelengths of up to $\sim$ 1580 μm (190 GHz). Most of the currently available sub-millimeter detectors can observe a bandwidth of up to ~10 GHz at a time, with exceptions up to ~35 GHz [17]. This places a limitation on the redshift determination with the currently available detectors.

1.1.2. The DESHIMA Instrument

The operating concept of DESHIMA (Deep Spectroscopic High-redshift Mapper) has proven itself to be of scientific relevance after a successful 'first light'-campaign in 2019 [18]. The DESHIMA instrument was installed to the ASTE (Atacama Submillimeter Telescope Experiment) telescope and aimed at several celestial objects to test its performance. It was capable of detecting the CO(3-2) line emission from the luminous infrared galaxy VV 114 at 339.0 ± 1.0 GHz. This is consistent with the rest frequency 345.796 GHz and a redshift of $z = 0.02$. The detector obtained a SNR of ~9 in 12.8 minutes. See Figure 1.1 for the spectrum results. From additional long integration sensitivity measurements of up to $t_{on} \sim 10^3$, it was found that the instrument is limited only by the atmospheric photon noise and coupling efficiency from the source signal to detector. The instrument sensitivity was found to reach a noise equivalent power (NEP) of $\sim 3 \cdot 10^{-16}$ W Hz$^{-0.5}$ under typical optical loading.

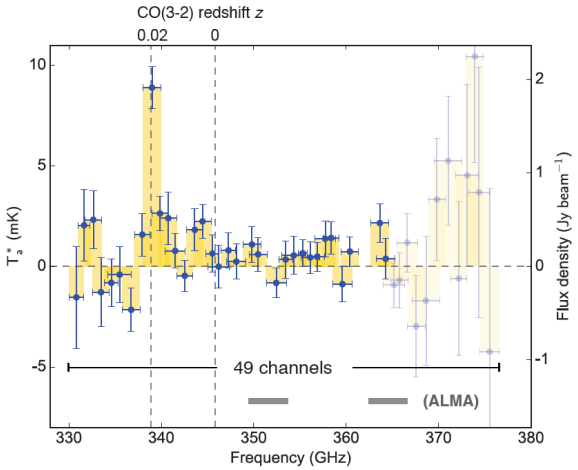

Figure 1.1: The spectrum of VV114 as detected by the DESHIMA instrument mounted inside ASTE. The CO(3-2) emission line from the luminous infrared galaxy VV 114 was found at 339.0 ± 1.0 GHz. This is consistent with its rest frequency 345.796 GHz and its redshift of $z = 0.02$. The detector obtained a SNR of ~9 in 12.8 minutes. Typical instantaneous ALMA bandwidths are indicated to illustrate the wideband operation of the DESHIMA instrument. Image by [18].

DESHIMA 1.0 Chip Layout

The on chip design of the prototype DESHIMA instrument consists of an array of microwave kinetic inductance detectors (MKIDs), which require superconducting operating conditions. See Figure 1.2 for an overview of the chip as described in [17]. The chip is made of a 100 nm NbTiN film on top of a c-plane sapphire substrate. An antenna is coupled to a THz transmission line. The transmission line is coupled to a filterbank of 49 narrowband channels covering the frequency range 332-377 GHz at a constant spectral resolving power of $F/\Delta F = 380$. From right to left the design center frequencies F_j are given as

$$F_j = 332\,(1 + \Delta F/F)^j \text{ GHz}. \tag{1.3}$$

For DESHIMA 1.0 the filters are meander line resonators. They were used for their second harmonic transmission ($\sim \lambda$), as the fundamental mode showed worse transmission. Note that these filters are not suited for scaling to larger detector bandwidths, as multiple harmonics could then be transmitted. See Figure 1.3 for the wideband transmission of the filterbank of the DESHIMA 1.0 instrument. The filters are arranged from high to low frequency. Each filter is subsequently coupled to a NbTiN-Al hybrid MKID. See section 2.1 for the operating concept of (hybrid) MKIDs in more detail. Each MKID is made of a quarter wave resonator patterned in the superconducting film. These resonators resonate at microwave frequencies dependent on the quarter wave resonator design. The MKIDs are grouped into seven groups (g) of seven MKIDs (i) with the resonance frequencies f_r as

$$f_r' = 5.6 \text{ GHz} + (g + 7i)\Delta F \tag{1.4}$$

$$f_r = \begin{cases} f_r' + 0.1 \text{ GHz} & f_r' > 6.0 \text{ GHz} \\ f_r' - 0.1 \text{ GHz} & f_r' < 6.0 \text{ GHz} \end{cases} \tag{1.5}$$

where ΔF is the equal step size of 16.7 MHz. This separation maximizes the difference in resonance frequencies of neighbouring MKIDs to minimize cross-talk. Furthermore, three wideband MKIDs are placed both before and after the filterbank and coupled to the transmission line for checking of signal transmission through the chip. An additional four MKIDs are placed behind the wideband MKIDs and not coupled to the transmission line, which function as blind MKIDs. Finally, two additional blind MKIDs and two MKIDs fabricated either of full NbTiN or Al are placed elsewhere on the chip for health and performance check purposes. All MKIDs are connected to a microwave read-out line, on which the multi-tone readout electronics is connected [56]. Incident radiation on the chip is transmitted through the THz line and absorbed in the Al strip of the respective MKID coupled to the bandpass filter. The absorbed radiation changes the resonance frequency of the respective MKID, which is detected as a phase change in the read-out.

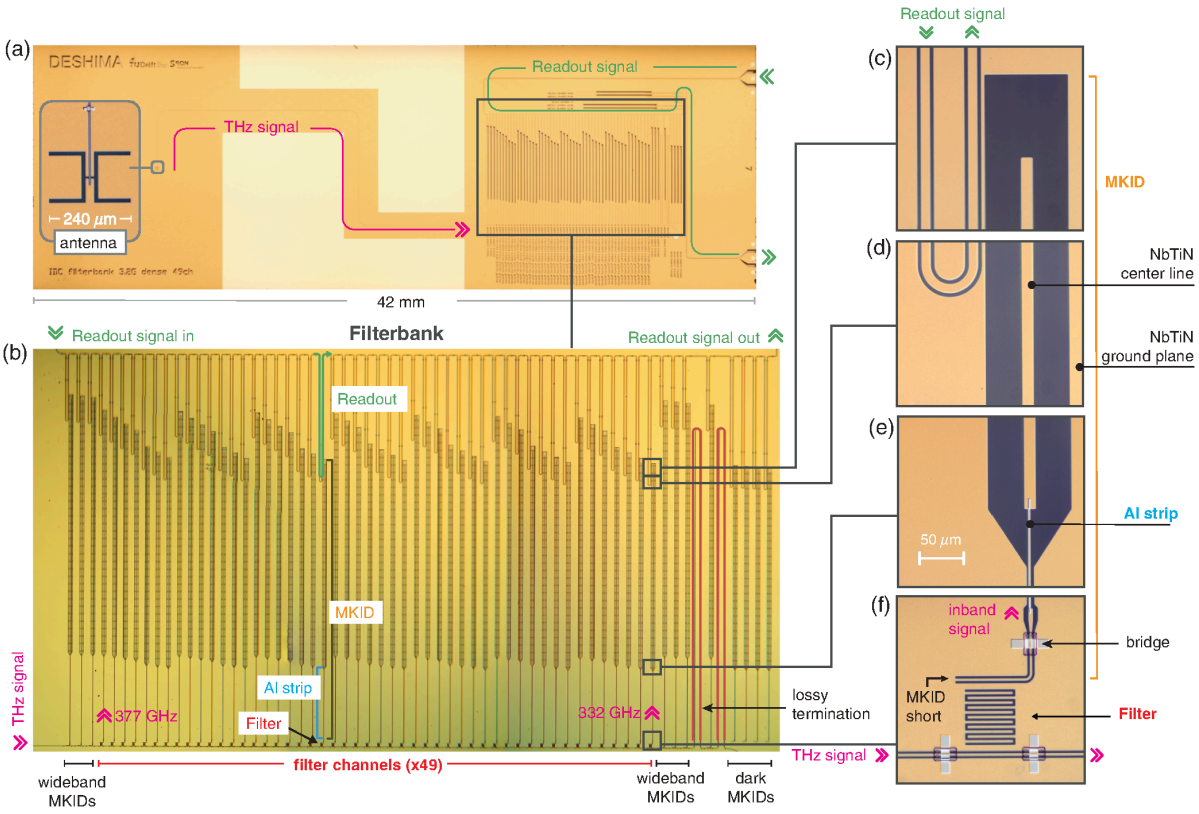

Figure 1.2: Overview of the on chip layout of the DESHIMA spectrometer. **a** Full chip overview. An antenna is coupled to a THz transmission line, which guides the absorbed signal to the read-out side of the chip. The THz transmission line is coupled to a filterbank of 49 channels over a range of 377-332 GHz, with each bandpass filter coupled to an MKID. Three MKIDs both before and after the filterbank are coupled directly to the transmission line to check the transmission. Four MKIDs are located after the filterbank and wideband MKIDs. They are not coupled to the transmission line and serve as blind MKIDs. In addition, several blind and health checking MKIDs are located to the top of the chip out of frame. A microwave read-out line passes all MKIDs. As each MKID operates at a different resonance frequency, the MKIDs can be multiplexed with a single read-out line. **c-f** A single MKID consists of a quarter wave resonator made of a NbTiN center strip connected to a shorted strip via an Al strip. Image from [17].

A Scalable Design: DESHIMA 2.0

The on-chip design of DESHIMA allows for a relatively easy upscaling to a larger bandwidth by adding additional MKIDs. The total bandwidth is limited by the superconducting gap frequencies of NbTiN and Al as [17]

$$F_{gap} \sim \frac{3.52 k_B T_c}{h} \tag{1.6}$$

where k_B is the Boltzmann constant, h the Planck constant and T_c the critical superconducting transition temperature. Above this frequency, the transmission losses will become too large for operation as superconducting material. Below this frequency, the superconducting properties limit the material to be an efficient absorber. For NbTiN the critical temperature is $T_{c,NbTiN}$ = 15K, which results in $F_{gap,NbTiN} \sim$ 1.1 THz. For Al $T_{c,Al}$ = 1.25K, therefore $F_{gap,Al} \sim$ 90 GHz. For proper operation, the THz frequencies to be detected have to

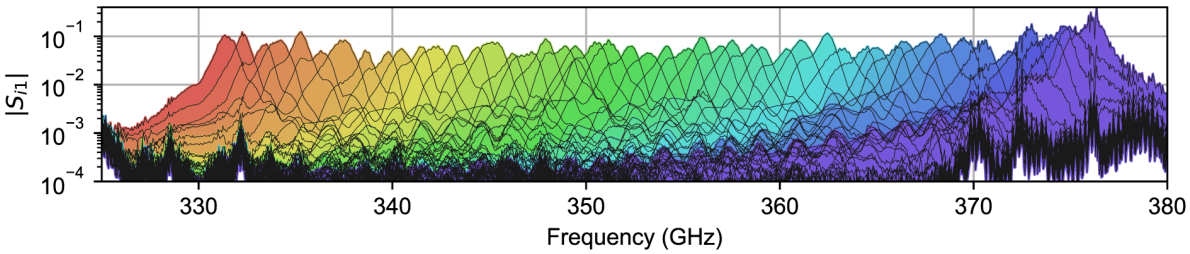

Figure 1.3: Wideband transmission of the DESHIMA 1.0 prototype filterbank. The detected transmission of all sub-millimeter filters connected to MKIDs are superposed for the frequency range of operation (332-337 GHz). Image from [17].

be within 90 GHz < F < 1.1 THz. Combined with a large bandwidth antenna, the on chip spectrometer could scale to ~1000 channels with a spectral resolving power of $F/\Delta F \sim 1000$ [17].

Current research and development is focused on the DESHIMA 2.0 instrument, which is scheduled to be deployed to ASTE in mid 2022. The DESHIMA 2.0 spectrometer chip will have a wide 220-440 GHz bandwidth with 347 channels at a spectral resolving power of $F/\Delta F = 500$ [52]. DESHIMA 2.0 needs a new filterbank design, as the second harmonic meandering resonator is unsuited for the wideband operation. A half-wave microstrip resonator is designed to operate in the fundamental mode, which allows for a wider range of operation sufficient for the DESHIMA 2.0 instrument. See Figure 1.4 for the wideband filter transmission.

The noise equivalent power during observation is expected to be NEP = $8.3 \cdot 10^{-17}$ W Hz$^{-0.5}$ [17]. Several sub-millimeter galaxies observed by the Herschel telescope have been selected as targets to verify the performance of DESHIMA 2.0. The performance goal is to observe the Herschel sub-millimeter galaxies with optical power coupled to the detector of $\sim 10^{-18}$ W at a signal-to-noise ratio of ~5 in 8 hours of continuous integration, and even fainter galaxies in 60 hours of segmented integration.

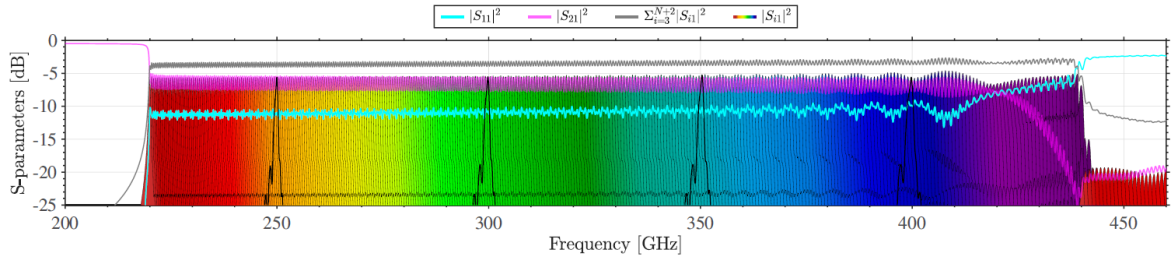

Figure 1.4: Wideband simulated transmission of the DESHIMA 2.0 filterbank. The simulated transmission of all sub-millimeter filters connected to MKIDs are superposed for the frequency range of operation (220-440 GHz). Several transmission profiles are highlighted with a black line to better illustrate the performance. Image from [44].

1.2. Motivation for an Emission Line Calibration Setup

The key applications of the DESHIMA instrument are as a redshift determination machine and as a fast wideband spectral imager [18]. When the instrument is used as a redshift determination machine, one is interested in the absolute frequency shift of spectral lines. An offset in frequency detection could cause systematic errors in determining the observed redshift. In addition, for its wideband spectral imaging application, it is of interest to evaluate the wideband performance and sensitivity limits. For both applications, it is of importance to calibrate the instrument wideband response for any offsets. Therefore, in order to understand and evaluate all possible errors of the DESHIMA instrument before the next telescope campaign, it is desirable to map the unique instrument response over its full spectrum for long integration time measurements with a lab based calibration setup. To compare the performance in lab with on site measurements, a calibration setup should ideally be able to generate a comparable signal in both intensity and frequency range. This requires a high stability of the calibration system over typical integration time measurements.

Missing Area in Available Calibration Measurements

Responsivity and frequency calibration measurements have already been established for the DESHIMA instrument, using blackbodies of known temperatures and a controllable terahertz source at sub-millimeter wavelengths, respectively [17]. See sections 3.2.2 and 3.2.1 for more information on these calibration measurements. However, the terahertz source used in the frequency calibration is expected to have an absolute frequency offset. This limits the accuracy of redshift determination. Furthermore, lab based tests of a faint source are of interest to test the overall instrument performance.

1.2.1. The Gas Cell Setup

To tackle both calibration and evaluation challenges, Zhang [63] designed an experimental setup around a known gas at low pressure. The emission spectra of gasses and their main spectral lines have been well analysed and documented at high accuracy. The detected emission line can be compared to the documented value to accurately determine the overall frequency offset of the instrument. Furthermore, by lowering the gas pressure, a faint source comparable to on-site measurements can be mimicked to test the detectability of the spectral lines. The emission of a gas is assumed to follow blackbody radiation $B(\nu, T)$ multiplied by the gas transmittance over frequency $t(\nu)$. In front of a background with radiation I_{bg}, the typical irradiant power I after the gas can be described as

$$I = B(\nu, T) \cdot (1 - t(\nu)) + I_{bg} \cdot t(\nu), \tag{1.7}$$

where ν is the frequency of the radiation, and T the temperature of the gas, generally at room temperature. See Appendix B.1 and B.2 for more information on the radiative transfer calculations through the setup. By controlling the pressure, one can alter the absolute values of the absorption peaks in the transmittance over frequency.

The use of a gas cell in combination with a sub-millimeter detector is not unique to this experiment. Wehres *et al.* designed an emission spectrometer at sub-millimeter range using a gas cell setup and a heterodyne receiver [58]. They achieved a stable setup up to 300 seconds and a flat output spectrum. However, their instantaneous band of operation was limited to 5 GHz. The work presented here is unique in facing the additional challenges for an instantaneous band of ~40 GHz with DESHIMA 1.0, and eventually ~200 GHz when DESHIMA 2.0 is available.

Gas Cell Setup Layout by Zhang

The previous setup by Zhang consisted of a low pressure CH_3OH gas at room temperature as a source in front of a liquid nitrogen background. A second nitrogen background was used as a representative off-source path. The paths were modulated with an optical chopper to reduce any low frequency noises in the setup and detector. See Figure 1.5 for a schematic overview of the gas cell setup by Zhang. The setup successfully determined an absolute frequency offset of the DESHIMA filterbank at $\Delta f = -0.92$ GHz for 1 mbar methanol. However, the setup still had unknown error sources, limiting the evaluation of the DESHIMA instrument for long integration times.

Zhang found both methanol (CH_3OH) and nitrous oxide (N_2O) to be good candidates within the frequency range of DESHIMA. Specifically, nitrous oxide was found to be an excellent candidate, as it has several clean spectral lines that scale well to lower pressures. At the time, only methanol was available. In this work, nitrous oxide will be primarily used. See Figure 1.6 for simulated spectra at typical low pressures used. The

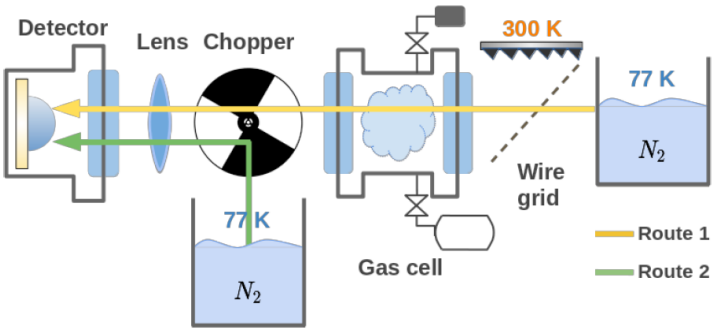

Figure 1.5: The gas cell based setup by Zhang. The chopper alternates the gas cell signal (yellow) and the liquid nitrogen background signal (green). This signal modulation method attempts to filter out the slow fluctuations of the background to improve the detectability of the emission lines originating from the low pressure gas. The wire grid is rotatable, which allows for controlled (partial) reflection of the 300K blackbody for responsivity calibration purposed. Image from [63].

spectra of atmospheric air are also included. See the work by Zhang for more information as to why these gasses were chosen [63].

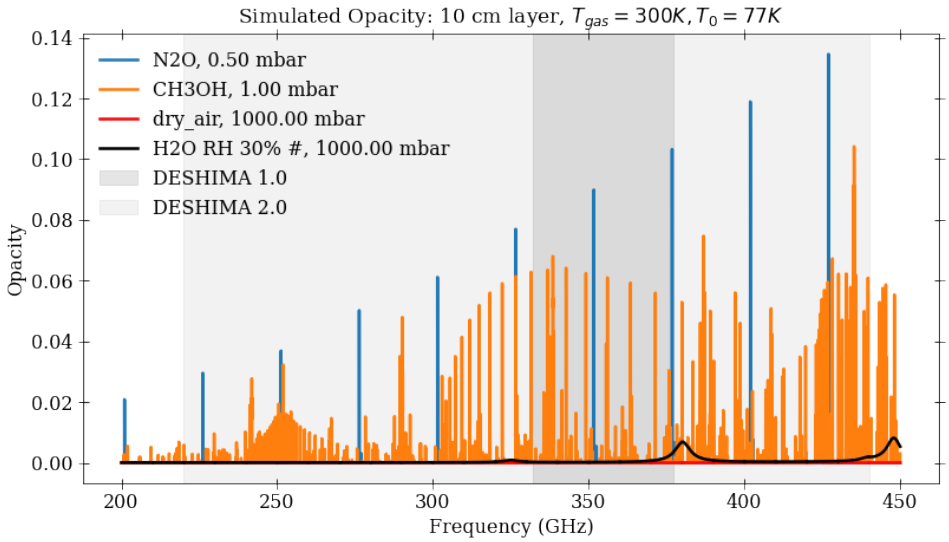

Figure 1.6: Simulated emission spectra of nitrous oxide and methanol at typical pressures used. The spectra of dry and humid air are included for comparison with the direct environment. Notice how the effect of the surrounding environment is negligible compared to nitrous oxide and methanol at these frequencies. The frequency ranges of the prototype DESHIMA 1.0 and the next generation DESHIMA 2.0 instruments are indicated. The spectra were simulated with the AM Atmospheric software package [42]. The simulations were done for 10 cm thick layers in front of a 77K blackbody brightness temperature background.

1.2.2. Optimizing the Gas Cell Setup

The main goal of this thesis project is to adapt the available gas cell setup by Zhang to evaluate the frequency response of the DESHIMA instrument for long integration tests. This translates to continuing on Zhang's work by further optimizing the setup and reducing the erroneous behaviour. Once the erroneous behaviour is reduced to a level where the system is sufficiently stable over typical integration times, the setup becomes a viable instrument to evaluate the DESHIMA instrument's detectability of faint source signals. The main two challenges in the latest design by Zhang were a standing wave in the output spectrum and the short noise stability of the setup, described in more detail below.

Standing Wave in the Output Spectrum

The standing wave can be clearly seen in the frequency spectrum of an empty gas cell measurement, see figure 1.7 by Zhang. Zhang suggested possible causes for the standing wave to be a misalignment between

the chopper and the cryostat window or due to reflections inside the system. The standing wave makes it impossible to detect emission spectra with a single measurement, and requires an additional empty gas cell measurement to find the emission spectrum as difference. However, the additional measurement requires a noise stability for the enite duration of both measurements. Furthermore, with the precise origin of the standing wave unknown, the standing profile might give a multiplicative error to all results, and not be solely additive. Any emission spectrum obtained by subtracting two measurements can still be altered by the multiplicative error.

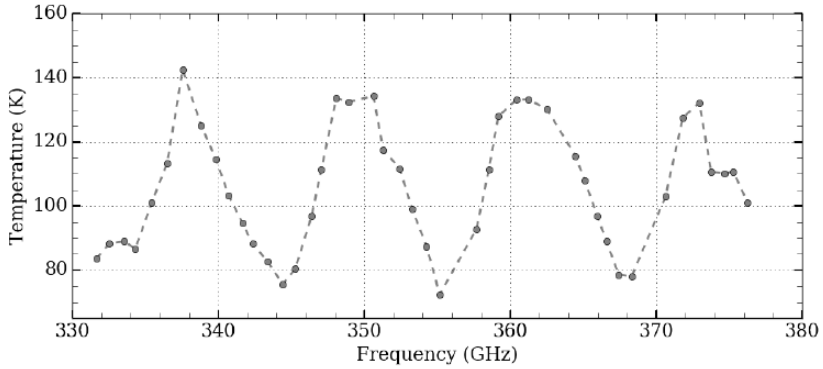

Figure 1.7: The measured brightness temperature spectral profile for the gas cell setup by Zhang with an empty gas cell. The profile shows a distinct standing wave [63].

Short Noise Stability of the Setup

The noise stability of the previous setup was insufficient for long integration time evaluations of the DESHIMA detector. Endo *et al.* showed that the DESHIMA instrument has a stable noise for at least the first 800 seconds of integration. However, noise analysis by Zhang, see figure 1.8, shows that the measurement variance of the gas cell setup does not improve after 10 to 20 seconds for some MKIDs. Zhang suggests the two separate optical paths with different liquid nitrogen backgrounds to be a possible cause for errors. The chopper modulation technique assumes the optical paths to have identical background fluctuations, which might not be sufficiently true for the separated backgrounds paths. Extra focus will therefore be on analysing the differences between the two paths, such as the backgrounds used.

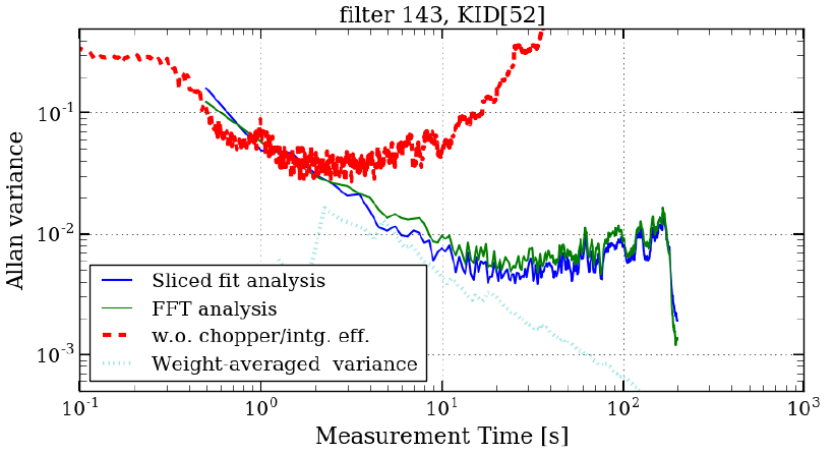

Figure 1.8: Allan variance analysis of a 'bad performing' MKID over a 1000-second measurement by Zhang. The variance stabilizes at ~20 seconds. When no optical chopper was used the performance was worse with the system becoming instable after only two seconds. The modulated signal by the optical chopper was demodulated in two ways, by fitting an expected chopping profile to the data or by taking the maximum FFT value per time slice. These methods showed similar results.

Improving the Gas Cell Setup

In order to improve on the setup by Zhang, two evident sub-goals are to address the above challenges. The standing wave is investigated in this thesis by focussing on optical resonances inside the setup, with an aim

to reduce the most limiting resonances. A detailed noise analysis was performed in this work to better understand the impact of certain aspects of the setup, to adept the limiting components and improve the stability over time. The required integration time for the DESHIMA 2.0 telescope campaign is up to 8 hours of continuous measurement. Therefore, the gas cell setup requires a noise stability of a similar timescale to be able to evaluate the DESHIMA instrument. An important consideration, when investigating the noise stability of the setup, is the certainty one has that any instabilities found do not originate in the detector itself. As described above, the DESHIMA prototype was found to be stable for at least 800s of integration. Therefore, any instabilities found up until that point will be assumed to be due to the setup and not due to the detector itself.

2

Theory

This chapter aims to give the reader an overview of the background theory behind the main concepts of this work. The chapter begins with the theoretical workings of a microwave kinetic inductance detector (MKID) and how it reacts to incident radiation. The chapter continues with an overview of typical noises considered in the analysis of the gas cell setup and the mathematical tools used to analysis them. As discussed in 1.2.2, the gas cell setup showed a distinct standing wave profile. Section 2.3 covers the theory behind optical resonance, with a focus on the influence it has on the DESHIMA frequency spectrum. Section 2.4 concludes this chapter with an overview of anti-reflective (AR) coatings for interfaces with sub-millimeter radiation to counter optical resonance in the setup.

2.1. Microwave Kinetic Inductance Detectors

The current preferred technology for astronomical observations is the use of cryogenic detectors. By operating near the absolute zero temperature, cryogenic detectors can use the benefits of superconducting physics combined with low thermal noises. One of the current state-of-the-art cryogenic detectors is the microwave kinetic inductance detector (MKID). MKIDs allow for high sensitive observations, and relative ease of multiplexing the readout of multiple MKIDs onto a single transmission line. The DESHIMA instrument is one of the pioneering instruments that implements an array of MKIDs into an on-chip spectrometer for astronomical observations [18].

This section will cover how MKIDs work and react to incident light. For an overall source for this section, as well as a good read for in depth information on MKIDs and their applications, see the dissertations by Gao, Mazin, Szypryt and de Visser [14, 21, 38, 51].

Athermal Detectors and Superconductors

Athermal detectors are detectors that detect photons by counting the quasi particles generated by an incident photon. For example, a charge-coupled device (CCD) measures the quasi particles generated when a photon excites an electron to the conduction band of a semiconductor. The minimum photon energy that can be detected is limited by the band gap energy of the respective semiconductor. This is where superconductors bring a significant advantage. For a superconductor, the band gap energy is typically $\sim 10^4$ times smaller, allowing for the detection of photons that are $\sim 10^4$ times less energetic [51].

2.1.1. Superconductance, Cooper Pair Breaking and Quasiparticles

Superconductors have zero resistance for constant electrical currents below a critical transition temperature. The current in a superconductor is carried by Cooper pairs instead of electrons. Following BardeenCooper-Schrieffer theory, Cooper pairs can be considered as a pair of electrons with opposite spin and momenta. The binding energy of Cooper pairs is found as [38]

$$2\Delta \approx 3.5 k_B T_c, \tag{2.1}$$

where k_B is the Boltzmann constant, T_c is the critical superconducting transition temperature, and Δ is the superconductor gap energy. This energy gap can be assumed equal to the Fermi energy Δ_0 as long as the temperature of the superconductor is well below the T_c.

Cooper pairs break down into quasiparticles upon absorption of the binding energy. Since the binding energy is relatively low, only at temperatures near the absolute zero are a notable amount of Cooper pairs present. The density of thermally excited quasiparticles n_{qp} can be calculated for a temperature T as

$$n_{qp}(T) \approx 2N_0\sqrt{2\pi k_B T\Delta_0}e^{-\Delta_0/k_B T}, \tag{2.2}$$

where N_0 is the single-spin density of electron states at the Fermi energy of the conductor [38].

Aside from thermal energy, an incident photon can as well cause Cooper pairs to break into quasi particles. If the energy of the incident photon is larger than the superconductor gap energy,

$$h\nu > 2\Delta, \tag{2.3}$$

then the photon can break a Cooper pair. Here h is the Planck constant and ν the frequency of the photon. With sufficient energy, a photon cause a cascade of multiple Cooper pairs breaking and quasi particles being generated. See as well Figure 2.1a for an illustration of an incoming photon breaking a Cooper pair. The number of excess quasiparticles generated due to an incident photon of energy $h\nu$ can be found as

$$N_{qp} \approx \frac{\eta h\nu}{\Delta}, \tag{2.4}$$

where η is the efficiency at which photon energy is converted to quasiparticles, determined at $\eta \approx 0.40$ [23]. For a high number of incident photons with a total radiant power P, the change in quasiparticle density can be found as

$$\delta n_{qp} \approx \frac{\eta P\tau_{qp}}{\Delta}, \tag{2.5}$$

where τ_{qp} is the quasiparticle lifetime. Two quasiparticles can recombine into a Cooper pair while emitting a phonon [38]. The average time for quasiparticles to fall back to Cooper pairs is given by this lifetime.

Under continuous optical load a steady state quasiparticle density will arise due to continuous Cooper pair breaking by the incident photons and recombining quasiparticles. The increased quasiparticle density under a continuous optical load shortens the quasiparticle lifetime. The lifetime is expected to scale as $\tau_{qp} \propto P_{opt}^{-1/2}$, with P_{opt} the optical loading power. This inverse square root dependency has been measured for the typical MKID type used in this thesis by [34]. From Equation 2.5 one can see that the change in quasiparticle density would then scale as $\delta n_{qp} \propto \sqrt{P_{opt}}$. This is of importance for the readout responsivity discussed in the next sections.

2.1.2. MKIDs: Quasiparticles and Surface Impedance

The breaking of Cooper pairs and generation of quasiparticles inside a superconducting film changes the surface impedance of the film. MKIDs operate by detecting this change of surface impedance. To show how the change in quasiparticles relates to a change in surface impedance, it is convenient to consider the surface conductance. The complex surface conductance can be represented as

$$\sigma = \sigma_1 - j\sigma_2. \tag{2.6}$$

Gao [21] derived the change of the real and imaginary parts of the surface conductance due to a change in quasiparticle density in a superconducting film as

$$\frac{d\sigma_1}{dn_{qp}} = \sigma_n \frac{1}{N_0\hbar f}\sqrt{\frac{2\Delta_0}{\pi k_B T}}\sinh(\xi)K_0(\xi), \tag{2.7}$$

$$\frac{d\sigma_2}{dn_{qp}} = -\sigma_n \frac{\pi}{2N_0\hbar f}\left[1+\sqrt{\frac{2\Delta_0}{\pi k_B T}}e^{-\xi}I_0(\xi)\right], \tag{2.8}$$

where I_0 and K_0 are the first and second modified Bessel functions of zeroth order, ξ is the coherence length of the impure superconducting film. N_0 is the single spin density of states and σ_n is the normal (non-superconducting) state conductance. The frequency f denotes the oscillation frequency of the superconducting film when considered a resonating circuit, as explained in the next section. Note, these equations are derived on several assumptions which require the following conditions to hold:

$$\hbar f \ll \Delta, \quad k_B T \ll \Delta, \quad e^{-\frac{E-\mu^*}{k_B T}} \ll 1, \tag{2.9}$$

where μ^* is the effective chemical potential when treating the quasiparticles as a Fermi gas following the Fermi-Dirac distribution. For a typical aluminium MKID these conditions hold up to 10 GHz.

Furthermore, Gao derived that the fractional change in surface impedance Z_s relates to a fractional change in surface conductance as

$$\frac{\delta Z_s}{Z_s} = \gamma \frac{\delta \sigma}{\sigma}, \tag{2.10}$$

with γ a factor depending on the superconducting film;

$$\gamma = \begin{cases} -1/2 & \text{Thick film, local limit} \\ -1/3 & \text{Thick film, extreme anomalous limit} \\ -1 & \text{Thin film, local limit} \end{cases}. \tag{2.11}$$

The local limit holds for $\xi_0 \ll \lambda_{\text{eff}} \vee l \ll \lambda_{\text{eff}}$, the extreme anomalous limit for $\xi_0 \gg \lambda_{\text{eff}} \wedge l \gg \lambda_{\text{eff}}$. The film is considered thin if the film thickness $d < l_\infty \ll \lambda_{eff}$, where l_∞ is the electron mean free path in the bulk case and λ_{eff} the effective penetration depth of the film.

Equations 2.7, 2.8 and 2.10 can be combined into

$$\frac{\delta Z_s}{|Z_s|} = \kappa |\gamma| \delta n_{qp}, \tag{2.12}$$

$$\kappa = \frac{\delta\sigma/|\sigma|}{\delta n_{qp}} \approx \frac{1}{\pi N_0}\sqrt{\frac{2}{\pi k_B T \Delta_0}}\sinh(\xi)K_0(\xi) + j\frac{1}{2N_0\Delta_0}\left[1+\sqrt{\frac{2\Delta_0}{\pi k_B T}}e^{-\xi}I_0(\xi)\right]. \tag{2.13}$$

These equations are an approximation of how a shift in quasiparticle density relates to a fractional impedance shift.

2.1.3. MKID as an LC Resonance Circuit

An MKID is typically made of a quarter wave resonator patterned in a superconducting film capacitively coupled to a transmission line. This can also be considered a microwave parallel LC resonator circuit, see Figure 2.1b for the respective network diagram. The circuit resonates at a certain frequency depending on the surface impedance. As seen in the previous section, the breaking of Cooper pairs into quasi particles slightly changes the surface impedance of the superconducting film. This change of surface impedance translates to a lowered resonance frequency and transformed complex transmission of the LC circuit.

MKID Transmission as a Function of Frequency

The complex forward transmission of the LC circuit can be approximated as a function of frequency f around the resonance frequency f_r as [21]

$$t_{12} = 1 - \frac{Q_r/Q_c}{1 + 2jQ_r\frac{f-f_r}{f_r}}, \tag{2.14}$$

where Q_r is the total quality factor of the resonator and Q_c the quality factor of the capacitive coupling to the transmission line. These are related as

$$\frac{1}{Q_r} = \frac{1}{Q_c} + \frac{1}{Q_i}, \tag{2.15}$$

where Q_i is the internal quality factor of the resonator, combining all other losses.

From 2.14 the power transmission as a function of frequency around the resonance frequency is derived as

$$\left|t_{21}(f)\right|^2 = 1 - \frac{1/Q_r^2 - 1/Q_i^2}{1/Q_r^2 + 4\left(\frac{f-f_r}{f_r}\right)^2}, \tag{2.16}$$

which follows a Lorentzian profile, see Figure 2.1c. The phase angle as a function of fractional frequency shift was as well derived as,

$$\theta = -\arctan 2Q_r\frac{f-f_r}{f_r}, \tag{2.17}$$

see Figure 2.1d.

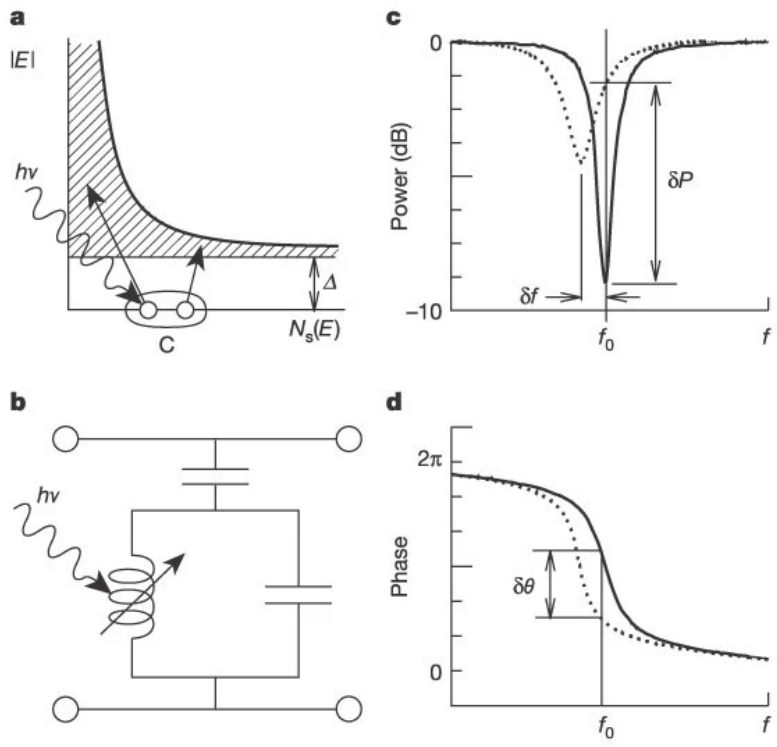

Figure 2.1: Several illustrations of the basic operations of microwave kinetic inductance detectors (MKIDs). Image by [13] **a** A photon with energy $h\nu > 2\Delta$, with Δ the superconducting gap energy, breaks Cooper pairs into quasiparticles. The quasiparticle density of states N_s is plotted as a function of quasiparticle energy E. **b** The MKID represented as an LC resonator capacitively coupled to a transmission line. The Cooper pair breaking and quasiparticle generation due to the incident photon result in a change in surface impedance (mainly inductance). **c** The power transmission of the MKID resonator circuit. The change in surface inductance causes a shift in resonance frequency f_0. The change in resistance causes wider and shallower resonance dip. **d** The change in complex transmission seen in the phase angle instead of the power intensity.

Above equations can as well be related to the change in quasiparticles. The change in complex transmission profile due to an increase in quasiparticles can be described as

$$\delta t_{21}|_{f=f_r,Q_c=Q_i} = \frac{1}{4}\frac{\delta n_{qp}}{n_{qp}}\left[1 + j\frac{\mathrm{Im}(\kappa)}{\mathrm{Re}(\kappa)}\right], \tag{2.18}$$

derived by Gao for a hybrid MKID under static operation. Static operation can be assumed, as the typical signal modulation is ~10 Hz for the DESHIMA instrument, which is considerably low.

This can be rewritten to a change in internal quality factor and resonance frequency following Equation 2.14 and 2.15 as

$$Q_i^{-1} = \alpha^* |\gamma| \mathrm{Re}(\kappa) n_{qp} \frac{2l_s}{l_r}, \tag{2.19}$$

$$\frac{\delta f_r}{f_r} = -\frac{\alpha^*}{2}|\gamma| \mathrm{Im}(\kappa) \delta n_{qp} \frac{2l_s}{l_r}, \tag{2.20}$$

where l_s and l_r are the length of the sensor strip and total length of the quarter wave resonator (including the strip). Note how the fractional shift in resonance frequency $\frac{\delta f_r}{f_r}$ primarily depends on the change in quasiparticle density δn_{qp}. In section 2.1.2 it was shown how the change in quasiparticle density scales with optical loading power as $\delta n_{qp} \propto \sqrt{P_{opt}}$, which translates to the fractional resonance frequency shift to scale similarly as

$$\frac{\delta f_r}{f_r} \propto \sqrt{P_{opt}}. \tag{2.21}$$

The resonance frequency of a single MKID under no optical or thermal load is dependent only on the design parameters. As long as each MKID has a unique resonance frequency and a sufficiently wide frequency band for its resonance shifts, multiple MKIDs can be coupled to the same transmission and read out line and function simultaneously. This allows for thousands of MKIDs to be coupled to the same transmission line.

MKID Resonator Response in the Complex Plane

Generally, the complex transmission of an MKID is measured and plotted in the complex plane. A frequency sweep shows the resonance circle in the complex plane, which is used to obtain the relevant MKID operation parameters. The amplitude and phase angle of the measured complex transmission (here denoted as S_{21}) can be read out respective to the circle's center as [14]

$$A = \frac{\sqrt{(\mathrm{Re}\,(S_{21}) - x_c)^2 + \mathrm{Im}\,(S_{21})^2}}{1 - x_c} \approx \frac{\mathrm{Re}\,(S_{21}) - x_c}{1 - x_c}, \tag{2.22}$$

$$\tan(\theta) = \frac{\mathrm{Im}\,(S_{21})}{x_c - \mathrm{Re}\,(S_{21})}, \tag{2.23}$$

where x_c is the center point of the complex circle on the real axis. Using either the amplitude or the phase angle data, one can fit the fractional frequency shift formulae as described in Equations 2.16 and 2.17. Other parameters, such as the quality factors, can as well be derived from complex transmission. See Figure 2.2 for a typical complex plane plot of the resonance circle. Note the typical noise illustrated in the figure. One can see that the noise changes both in phase angle and amplitude. The noise representations in the complex plane can inform the user of the origin of the noises. Amplifier noise for example shows equal response in amplitude and phase angle. Noise sources in the MKID capacitance or inductance typically only show a response in phase angle [38].

2.1.4. Fundamental MKID Noise Behaviour

Radiation detection with an MKID detector is limited by several fundamental noises.

Generation-Recombination Noise

The random process behind the generation and recombination of quasiparticles and Cooper pairs result in a fundamental noise level. The noise equivalent power (NEP) due to the generation-recombination noise can be described as [14]

$$\mathrm{NEP}_{gr} = \frac{2\Delta}{\eta_{pb}}\sqrt{\frac{N_{qp}}{\tau_{qp}}} \propto N_{qp} \tag{2.24}$$

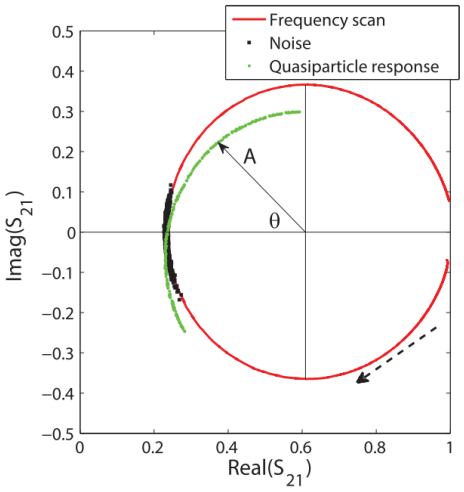

Figure 2.2: Complex plane representation of the MKID transmission. The complex transmission of an MKID is typically detected and plotted in the complex plane for further processing. A frequency sweep (red) shows the resonance circle of the MKID. A change in quasi particles affects the resonance of the MKID and changes the resonance circle (green). Typical noise of an MKID is as well illustrated (black).

where N_{qp} is the equilibrium number of quasiparticles in the resonator. Note that the NEP will increase with thermal or optical load as it increases the number of quasiparticles. In the limit where the number of quasiparticles is dominated by optical load, the noise can be written as a function of optical loading power P_{opt} as

$$\mathrm{NEP}_{gr} \approx \sqrt{\frac{2P_{opt}\Delta}{\eta_{pb}}}. \tag{2.25}$$

Photon Noise

The randomness in the arrival times of photons results as well in a fundamental noise in the detected output. For an MKID operating with millimeter waves the photon noise NEP is [60]

$$\mathrm{NEP}_{ph} = \sqrt{2P_{opt}hF(1+\eta_{opt}B)} \quad \text{with} \quad B = \frac{1}{e^{hF/k_BT_{BB}}+1}, \tag{2.26}$$

where F is the frequency of the millimeter wave, B the photon occupation number per mode, T_{BB} the blackbody temperature of the respective radiation, and η_{opt} the efficiency from emission to detection of one mode. Using $hFmB \approx P/\Delta F$, where ΔF is the bandwidth of the bandpass filter coupled to the MKID, the photon noise can be rewritten to

$$\mathrm{NEP}_{ph} = \sqrt{2P_{opt}\left(hF + \frac{P_{opt}}{\Delta F}\right)}. \tag{2.27}$$

Combined Noise Equivalent Power

The combined total NEP of both generation-recombination noise and photon noise can be found using

$$\mathrm{NEP}_t^2 = \mathrm{NEP}_{gr}^2 + \mathrm{NEP}_{ph}^2 \tag{2.28}$$

to be [18]

$$\mathrm{NEP}_t = \sqrt{2P_{opt}\left(h\nu + \frac{P_{opt}}{\Delta F}\right) + \frac{4P_{opt}\Delta}{\eta_{pb}}} \tag{2.29}$$

2.2. Noise Analysis

Any output of a measurement will be prone to unwanted modifications, collectively combined into the term 'noise'. These modifications can occur anywhere in the setup from background to readout and even during storage of measured data. Due to the typically unknown origin of noises, the behaviour of noise is generally classified by how the noise modifies the signal and by its statistical properties. The scope of this thesis is to improve the stability of the gas cell setup, to evaluate sub-millimeter detectors. The main interest in noises therefore lies in the identification of noises to eliminate them.

2.2.1. Coloured Noises

The key types of noise concerned within this thesis work are the coloured noises. The coloured noises are uncorrelated random signals, classified based on their distinct frequency dependency in the power spectral density profile of the signal. Note that the frequency concerned in this section are related to the sampling over time. These are not to be confused with radiation frequency and emission spectra. The colours of power law noises are rough analogies to the spectrum of light at the respective colours. White, pink, red, blue, and purple noise all follow a power law PSD profile $\sim f^{\alpha}$ with α at 0, -1, -2, 1, 2, respectively. Note that when a white noise signal is integrated or differentiated, the resulting signal has a red or purple profile, respectively. Below, three specific noise types are highlighted as they are of special interest in this thesis.

Gaussian White Noise

In this thesis, mainly a Gaussian white noise will be concerned, although white noise can be of any distribution. The combination of many natural background noise sources typically take on a white Gaussian noise form. Furthermore, thermal noise, or JohnsonNyquist noise, is as well a noise with a white Gaussian profile. It is present in all electronics due to the thermal motion of charge carriers. Gaussian white noise has the advantage of a stable average over time, which translates to a reduced impact on the read-out stability when averaging over long time intervals.

Flicker Noise

Flicker noise is a noise present in almost all electronics following a 1/f profile, due to a variety of processes. Flicker noise is typically characterized by its 'knee' or cut-off frequency where the flicker noise reaches the white thermal noise floor. The flicker noise is mostly dominant and of concern before the cut-off frequency, after which thermal noise takes over. Flicker noise typically has a Gaussian distribution. Flicker noise is dominant at low frequency and can have a large impact for long integration measurements.

Random Walk Noise

If a red noise has a Gaussian distribution, it is typically called Random Walk, Brownian or Brown noise. Note that Red noise is as well found when a white noise signal is integrated.

2.2.2. Stability over Integration Length

For the typical detectors being evaluated by the gas cell setup, such as DESHIMA, the background noises are assumed to have a Gaussian distribution. Gaussian noises converge to a mean value when averaging the noise over time. This allows the observation of relatively weak sources when integrating a signal over long time intervals. In reality, the measured signal is typically prone to non-Gaussian noises, causing limitations on the continued averaging of weak signals. It is of interest to know how the error in the measured signal is affected for different lengths of integration time. This allows for a better understanding and identification when and where deviations from a white Gaussian noise integration show up.

To obtain the dependency on integration interval length, the standard deviation value for different slice lengths of the total measurement could be compared. However, standard deviation assumes the signal to be Gaussian. The estimator for standard deviation does not converge for some noise types, such as flicker noise. David Allan came up with a solution to this problem, where one compares each data point to only its subsequent samples, instead of all samples in a slice. This allows the estimator to converge for noises such as flicker noise [1].

2.2.3. Allan Deviation Analysis

Allan deviation is a tool to analyse the frequency stability over integration length. It is generally used in a graph to visualize the change in Allan deviation over an increasing integration interval. This section will cover several implementations of Allan deviation and its successors. An overall source for this section as well as an

advised overview for further reading into frequency analysis is the Handbook of Frequency Stability Analysis, written by Riley for The National Institute of Standards and Technology, see [47].

Fractional Frequency and Phase Deviation
Allan deviation can be calculated from time and frequency data, by either using phase deviation data or fractional frequency data. Here, only calculations based on frequency data are given, since the read-out data of DESHIMA is used as fractional frequency data. The fractional frequency data $y(t)$ is defined as

$$y(t) = \frac{f(t) - f_0}{f_0}, \tag{2.30}$$

where f_0 is the nominal resonance frequency. The fractional frequency is essentially the relative frequency shift with respect to the nominal frequency. Note that a single fractional frequency sample is obtained from a time interval of phase data.

The fractional frequency data can be converted to phase deviations over time and vice versa by integration or differentiation. This is sometimes done to improve computation speeds. Note that these phase deviations over time are not the same as the phase of the resonance circle for the MKID read-out. All computations in this thesis were done using the AllanTools package [57], see Appendix F.2.

Allan Variance and its Confidence interval
The Allan variance (AVAR) is defined as

$$\text{AVAR} \quad \sigma_y^2(\tau) = \frac{1}{2(M-1)} \sum_{i=1}^{M-1} \left(y_{i+1} - y_i\right)^2 \tag{2.31}$$

where σ_y^2 is the Allan variance for the measurement interval of length τ consisting of M fractional frequency samples y_i. Essentially, the Allan variance is half the mean of the squared difference of subsequent fractional frequencies. The Allan deviation (ADEV) is defined as the square root of Allan variance,

$$\text{ADEV} \quad \sigma_y(\tau) = \sqrt{\sigma_y^2(\tau)}, \tag{2.32}$$

similar to standard deviation and standard variance.

Allan deviation is generally not given as a single value, but as a plot of the Allan deviation versus increasing averaging interval. As discussed earlier, the different kinds of power law noises can be discerned based on their power spectral density profile. This power law dependency translates roughly as $\mu = -\alpha - 1$, with α being the exponent of the power spectral density behaviour $S_y(f) \sim f^\alpha$, and μ the exponent in the Allan variance behaviour $\sigma_y^2(\tau) \sim \tau^\mu$. Therefore, Allan deviation follows $\sigma_y(\tau) \sim \tau^{\mu/2}$. See Table 2.1 and Figure 2.3 for the typical power law behaviour of the different noise types. White Gaussian, flicker (pink Gaussian) and random walk (red Gaussian) noises are considered in either phase modulation (PM) or frequency modulation (FM) in the figure and table. Any drifts over time in the fractional frequency data will cause an upward $\mu \sim 2$ slope. Note that the use of PM and FM follows typical literature notation. All noises can be described as FM noises, as the phase notation can be converted to frequency notation by integration. Here the noises will be distinguished based on μ to avoid confusion with the MKID phase read-out. For measurements in this thesis, the PM noise profiles were not encountered.

The confidence interval (error bar) of an Allan deviation value is typically found as $\pm\sigma_y/\sqrt{M}$. Note, this is not the confidence interval of the mean value of the dataset. If the noise type is known, a multiplicative factor (Kn) can be applied for a more accurate confidence interval. These factors can be calculated based on the bias function of the Allan deviation compared to the standard deviation.

Interpreting Power Law Noises in Frequency Stability
David Howe has done extensive research into Allan variance. Multiple sources used and referenced in this thesis have been written by him. He has also published a paper on how to interpret the typical power law noises in a frequency analysis of a resonating system [31].

White Gaussian and Flicker PM Noise: μ = -2
White Gaussian and flicker phase modulated noise are typically not due to the resonance mechanism, but

Noise Type	α	μ	**Kn**
White PM	2	-2	0.99
Flicker PM	1	-2	0.99
White FM	0	-1	0.87
Flicker FM	-1	0	0.77
Random Walk FM	-2	1	0.75

Table 2.1: The exponents of the power law profiles for the power spectral density (α) as well as for the Allan variance (μ). The last column shows the multiplication factor one can apply to the confidence interval once the noise type is determined. White Gaussian, flicker (pink Gaussian) and random walk (red Gaussian) noises are considered in either phase modulation (PM) or frequency modulation (FM) following typical literature notation. For measurements in this thesis, the PM noise profiles were not encountered

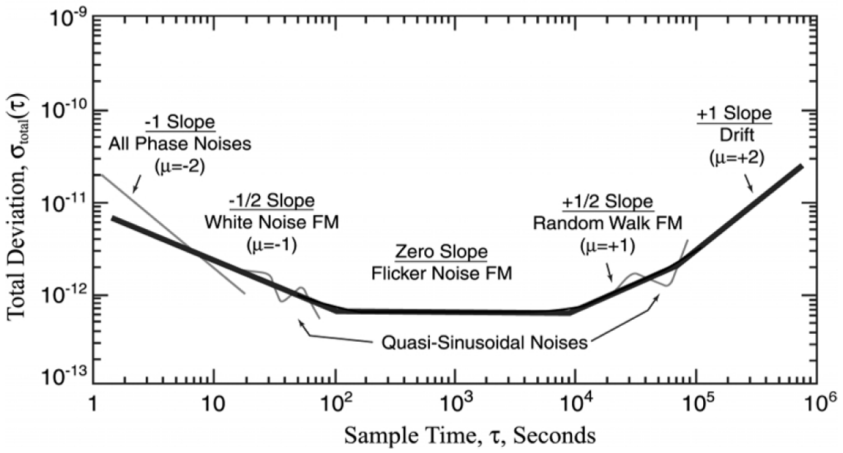

Figure 2.3: Allan deviation versus averaging interval length, showing the typical noises seen in frequency analysis. Notice how drifts in the fractional frequency data will result in a $\mu \sim 2$ slope. The plot also illustrates the quasi-sinusoidal oscillations believed to be due to discrete sampling. Note that correlated noises also show up as oscillating disturbances. Image from [31]. Not shown is the end of data error occurring with computed Allan deviations. The profile would drop at high averaging intervals. Its impact depends on the deviation type.

due to the read-out electronics, specifically the amplifiers. The noise generally finds its origin in several subsequent amplifications. It can be reduced by optimizing the read-out electronics, using high quality components, or increasing the power supplied to the resonator's frequency source (if possible for white Gaussian noise).

White and Flicker FM Noise: μ = -1, 0
White and flicker frequency modulated noised are common noises. White noises are typical for standard oscillators. Flicker frequency modulated noise is not well understood and is even present in high quality resonators.

Random Walk FM Noise: μ = +1
Random walk frequency modulated noise is typically related to the physical environment of the resonance mechanism. Any changes, such as vibrations, mechanical shocks or temperature changes can cause the noise.

Improved Allan Deviation Alternatives
Since the introduction of Allan deviation (ADEV), several new alterations to calculate the deviation value have been proposed. The current advised standard is to use overlapping Allan deviation (OADEV) as it allows for improved confidence intervals by using overlapping separated samples for comparison instead of the direct subsequent samples [47, 50]. Overlapping Allen variance (OAVAR) is defined as

$$\text{OAVAR} \quad \sigma_y^2(\tau) = \frac{1}{2m^2(M-2m+1)} \sum_{j=1}^{M-2m+1} \sum_{i=j}^{j+m-1} \left(y_{i+m} - y_i\right)^2 \tag{2.33}$$

where m is the averaging factor, which controls the range of overlap. For optimal results, the range of overlap should be the entire averaging interval $\tau = m\tau_0$, where τ_0 is a single sample interval. However, even when using overlapping Allan deviation, it is generally only trustworthy for averaging intervals up to 10% of the total measurement time. After this point, end of data error will significantly underestimate the deviation value [28]. Furthermore, (overlapping) Allan deviation is prone to show quasi-sinusoidal behaviour at long averaging times, as illustrated in Figure 2.3. These quasi-sinusoidal profiles are believed to be errors caused by finite sampling and processing.

A more computationally intensive version of overlapping Allan deviation is total deviation (TOTDEV), which reflects the measured data in its phase form at both ends of the total measurement. This increases the 'range of trust' (reliable averaging intervals) up to 50% of the total measurement time [29]. Essentially, the total measurement data is extended circularly. Total variance (TOTVAR) is defined as

$$\text{TOTVAR} \quad \sigma_y^2(\tau) = \frac{1}{2(M-1)} \sum_{i=1}^{M-1} \left(y^*_{i+j+1} - y^*_{i+j}\right)^2 \tag{2.34}$$

and looks similar to the calculation of Allan variance. However, here y^* denotes the complete virtual array with the reflected data at both ends and the original data at its center [27]. Total deviation is an unbiased estimator of Allan deviation if the noise is white or flicker PM ($\mu = -2$), or white FM ($\mu = -1$). Care has to be taken that total deviation underestimates the Allan deviation for flicker FM ($\mu = 0$) and random walk FM ($\mu = +1$) at high averaging times compared to the total measurement length T. The bias function is given by

$$B_{Total}(\tau) = \frac{\sigma^2_{Total}}{\sigma^2_{Allan}} = 1 - a \cdot \frac{\tau}{T}, \quad 0 < \tau \leq \frac{1}{2}T, \quad a = \begin{cases} \ln(2)/3 & \text{flicker FM} \\ 3/4 & \text{random walk FM} \end{cases} \tag{2.35}$$

Note, the total deviation value is at maximum ~6% and ~21% lower than the Allan deviation value for flicker FM and random walk FM, respectively.

Total deviation will be the Allan-like deviation of choice within this thesis, as it allows for a good range of trust without needing unreasonable computational power for the data analysis. A notable mention is Thêo1 [30], which is a new class of statistical analysing tools that operates comparable to Allan variance. It has a range of trust of up to 75% of the total measurement time. Thêo1 is not used in this thesis due to the unworkable computation times.

2.2.4. On/Off Signal Modulation to Reduce Low Frequency Noise

It is key to find ways to reduce the effect of noises and experimental errors by proper calibrations and zero-measurements. An effective method to reduce low frequency noise is by on/off source signal modulation. On/off source signal modulation is done by quickly alternating the on-source signal with the off-source signal, and subtracting the off-source data from the on-source data. Any noises dominant at frequencies lower than the frequency at which the on- and off-source signals are alternated will be effectively subtracted out. Or, from a signal processing perspective, one can think of the chopping as shifting the low frequency information to a higher carrier band around the chopper frequency. Any low-frequency noises are effectively filtered by taking the amplitude of the carrier signal, like a bandpass filter around the carrier frequency. See section 4.1 for more information on the demodulation method used.

On/off source signal modulation is widely used in astronomy and in electronic signal processing. In astronomy, its typical use is to filter out the slow fluctuations and 1/f noise due to the atmospheric or deep space background [26]. It is generally executed by chopping an on- and off-source optical signal before reaching the detector. In electronic signal processing, on/off signal modulation can be used to limit the impact of flicker noise [19], since flicker noise is especially dominant at lower frequencies due to its 1/f power spectral density dependence. Flicker noise is typically present in read out electronics and reduced by electronically chopping the signal, for example by multiplication with a square wave. Optically chopping should reduce the flicker noise in the read-out electronics as well.

An 1/f noise profile has also been found to be present in the frequency read-out of superconducting resonators such as MKIDs. Current belief is that two level systems are present in dielectric material on the resonator superconducting surface. Interactions of with the two level systems cause a 1/f noise called two-level-system (TLS) noise [8]. The on/off source modulation should as well reduce the impact of TLS noise at frequencies lower than the chopping frequency.

2.3. Optical Resonance

The distinct standing wave profile in the output spectrum of the gas cell setup is indicative of resonances. Optical resonance is therefore of high interest within this thesis. Optical resonances typically occur when partially reflective interfaces are placed after each other, as they allow for incoming radiation to interfere with phase shifted radiation. In order to better understand these resonances and to be able to identify possible components causing the distinct standing wave, this section dives into the theory behind the Fabry-Pèrot etalon. The Fabry-Pèrot etalon is the simplest form of an optical resonator, consisting of two parallel partially reflecting interfaces.

2.3.1. Fabry-Pèrot Etalon: Resonance Causing a Standing Wave

Fabry-Pèrot etalons consist of two partially reflective interfaces at a certain spacing. Electromagnetic radiation travelling through the interfaces will be partially 'stored' in the cavity in between the interfaces due to the partial reflections. Depending on the properties of this cavity (e.g., refractive index and optical length) the 'stored' radiation will interfere with incoming radiation. The transmitted radiation through the etalon will take on a periodic wavelike spectrum. This spectrum effect has been used in several optical fields such as telecommunications or spectrometry for its filtering properties. For this thesis, however, the main interest is in reducing the impact of Fabry-Pèrot etalons. Any subsequent partially reflecting interfaces inside the measurement setup can essentially be considered as a Fabry-Pèrot etalon with its spectrum altering effects. Therefore, Fabry-Pèrot resonance is certain to affect the transmission spectra of the setup.

Deriving the Transmission Profile of a Fabry-Pèrot Etalon

There are several ways to derive the total power transmission coefficient for a Fabry-Pèrot etalon. Here the derivation is primarily done in wavelength space as it allows for ease of comparison with measured spectra and for defining spectrum related properties. See as well [33] for a concise overview of the basics of Fabry-Pèrot etalons and other ways to derive the transmission.

The resonance profile occurs due to the phase shifted reflected radiation interfering with incoming radiation. The phase shift is related to the optical path difference. This optical path difference (OPD) for parallel incoming radiation can be found as

$$\mathrm{OPD} = 2nl\cos\theta, \tag{2.36}$$

where n is the refractive index inside the etalon of length l and θ is the internal angle of propagation respective to the normal of the interface. See Figure 2.4 for an illustration of the path difference.

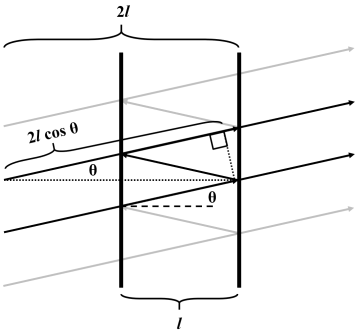

Figure 2.4: Illustration of the path difference between a direct path and a parallel reflected path in a Fabry-Pèrot etalon. Each reflection results in a path difference inside the etalon of $2l\cos\theta$, where l is the etalon length and θ the propagation angle relative to the normal of the partially reflecting interfaces.

The phase difference caused by a single round trip in the etalon can be found using the optical path difference as

$$\Delta\phi = \frac{2\pi}{\lambda}\cdot\mathrm{OPD} = \frac{2\pi}{\lambda}\cdot 2nl\cos\theta \tag{2.37}$$

$$= \frac{2\pi f}{c}\cdot 2nl\cos\theta, \tag{2.38}$$

where λ, f and c are the vacuum wavelength, frequency and speed of light of the incoming radiation. A single round trip results in a total field of direct and reflected radiation inside the etalon as,

$$E_1 = \left(1 + r_1 r_2 e^{i\Delta\phi}\right) E_0, \tag{2.39}$$

where E_0 is the direct field and r_1 and r_2 represent the field reflection coefficients for the first and second interface. For unlimited round trips where all reflections are interfering with each other the total field can be considered as a series inside the etalon as

$$E_\infty = \left(1 + r_1 r_2 e^{i\Delta\phi} + r_1^2 r_2^2 e^{i2\Delta\phi} + r_1^3 r_2^3 e^{i3\Delta\phi} + \ldots\right) E_0. \tag{2.40}$$

This series can be written into a geometric series, which converges since $\left\| r_1 r_2 e^{i\Delta\phi} \right\| < 1$ as

$$E_0 \sum_{j=0}^{\infty} \left(r_1 r_2 e^{i\Delta\phi}\right)^j = \frac{1}{1 - r_1 r_2 e^{i\Delta\phi}} E_0. \tag{2.41}$$

The transmission coefficient t of the interfaces can be defined as $t^2 = 1 - r^2$, assuming no losses and uniform s- and p-polarised light. By including the transmission coefficients from passing through both interfaces, the final transmitted radiation field after the etalon can be written as

$$E_{trans} = \frac{t_1 t_2}{1 - r_1 r_2 e^{i\Delta\phi}} E_{inc}. \tag{2.42}$$

The transmitted intensity I_{trans} can now be found based on the incoming intensity I_{inc} as

$$\begin{aligned} I_{trans} &= E_{trans} E_{trans}^* = \frac{t_1^2 t_2^2}{\left(1 - r_1 r_2 e^{i\Delta\phi}\right)\left(1 - r_1 r_2 e^{-i\Delta\phi}\right)} E_{inc} E_{inc}^* \\ &= \frac{t_1^2 t_2^2}{1 + r_1^2 r_2^2 - r_1 r_2 \left(e^{i\Delta\phi} + e^{-i\Delta\phi}\right)} E_{inc} E_{inc}^* = \frac{t_1^2 t_2^2}{1 + r_1^2 r_2^2 - 2 r_1 r_2 \cos\Delta\phi} E_{inc} E_{inc}^* \\ &= \frac{T_1 T_2}{1 + R_1 R_2 - 2\sqrt{R_1 R_2}\cos\Delta\phi} I_{inc}, \end{aligned} \tag{2.43}$$

where the equation was rewritten in terms of power reflectivity $R = r^2$ and transmittance $T = t^2 = 1 - r^2$. Using the double angle formula, $\cos 2\alpha = 1 - 2\sin^2\alpha$, the relative transmittance can be rewritten to its better known form

$$\begin{aligned} \frac{I_{trans}}{I_{inc}} &= \frac{T_1 T_2}{1 + R_1 R_2 - 2\sqrt{R_1 R_2}\left(1 - 2\sin^2\Delta\phi/2\right)} = \frac{T_1 T_2}{1 + R_1 R_2 - 2\sqrt{R_1 R_2} + 4\sqrt{R_1 R_2}\sin^2\Delta\phi/2} \\ &= \frac{(1 - R_1)(1 - R_2)}{\left(1 - \sqrt{R_1 R_2}\right)^2 + 4\sqrt{R_1 R_2}\sin^2\Delta\phi/2}. \end{aligned} \tag{2.44}$$

Free Spectral Range of a Fabry-Pèrot Etalon

Equation 2.44 can now be used to better understand the resonance profile. For maximum transmission the equation shows that $\sin^2\Delta\phi/2 = 0$ has to hold and for minimum transmission $\sin^2\Delta\phi/2 = 1$. For maximum transmission one finds

$$\frac{\Delta\phi}{2} = k\pi \quad \text{with } k \text{ any integer}, \tag{2.45}$$

$$k\pi = \frac{\pi}{\lambda} 2nl\cos\theta, \tag{2.46}$$

$$k\lambda = 2nl\cos\theta = \text{OPD}. \tag{2.47}$$

Here, it can be seen that any wavelength that can fit an integer times inside the optical path difference will result in maximum transmittance. The free spectral range is defined as the separation in wavelength space of subsequent resonance peaks in the Fabry-Pèrot etalon transmission spectrum. The free spectral range $\Delta\lambda$ can be found as

$$\Delta\lambda_{FSR} = \lambda_{m-1} - \lambda_m = \frac{\text{OPD}}{m-1} - \frac{\text{OPD}}{m} = \frac{\text{OPD}}{m(m-1)} = \frac{\lambda_m}{m-1} \tag{2.48}$$

$$= \frac{\lambda_m^2}{m\lambda_m - \lambda_m} = \frac{\lambda_m^2}{\text{OPD} - \lambda_m}. \tag{2.49}$$

If the wavelength spectrum of interest is centered around center wavelength λ_c and OPD $\gg \lambda_c$, this can be approximated to a periodicity in the spectrum as

$$\frac{\lambda_c^2}{\text{OPD} - \lambda_c} \approx \frac{\lambda_c^2}{\text{OPD}} = \frac{\lambda_c^2}{2nl\cos\theta}. \tag{2.50}$$

Similarly the free spectral range in frequency space can be derived as

$$\Delta f_{FSR} = f_{m+1} - f_m = \frac{c}{\lambda_{m+1}} - \frac{c}{\lambda_m} = \frac{(m+1)\,c - mc}{\text{OPD}} = \frac{c}{\text{OPD}} = \frac{c}{2nl\cos\theta}. \tag{2.51}$$

Note that these formulae for the free spectral range can as well be used to identify an etalon length and refractive index from a measured spectrum that shows a wavelike profile. This is of interest for this thesis work to identify the origin of the standing wave as described in section 1.2.2.

2.3.2. Reflectivity of an Interface

The transmission of a Fabry-Pèrot etalon as described in Equation 2.44 is dependent on Fresnel power reflectivity R and transmission T. For a single interface separating two media of refractive indices n_1 and n_2, the Fresnel power reflection coefficient for s- and p-polarised light can be derived from the Fresnel equations as

$$R_s = \left(\frac{n_1\cos\theta_i - n_2\cos\theta_r}{n_1\cos\theta_i + n_2\cos\theta_r}\right)^2, \tag{2.52}$$

$$R_p = \left(\frac{n_1\cos\theta_r - n_2\cos\theta_i}{n_1\cos\theta_r + n_2\cos\theta_i}\right)^2, \tag{2.53}$$

with angle of incidence θ_i and angle of refraction θ_r. These angles are dependent on each other through Snell's law, see Equation 2.56. For uniform s- and p-polarised light the overall reflectivity is the average of both polarizations, as

$$R = \frac{R_s + R_p}{2}. \tag{2.54}$$

For normal incidence this simplifies to

$$R = R_s = R_p = \left(\frac{n_1 - n_2}{n_1 + n_2}\right)^2. \tag{2.55}$$

This equation clearly shows the dependency of reflectivity on the difference between refractive indices. In order to minimize the optical resonance of a Fabry-Pèrot etalon, one has to minimize the reflections. To minimize the reflection of an interface, the squared difference in refractive indices between both sides of an interface has to be minimized.

A window as a Fabry-Pèrot cavity

A window can typically be considered as a homogeneous medium of single refractive index with parallel interfaces separating two other media. A single window can therefore be considered as a Fabry-Pèrot etalon as it has two partially reflecting interfaces, see Figure 2.5 illustrating a window as a Fabry-Pèrot etalon. The angle of propagation inside the window is the angle of refraction due to the first interface. This angle can be found using Snell's law and the angle of incidence as

$$\sin\theta_{inside} = \frac{n_{medium-1}}{n_{window}}\sin\theta_{incidence}. \tag{2.56}$$

2.3.3. Resonance Spectrum of a Window

The gas cell concerned in this thesis has windows separating a low pressure gas from the outside air. One can assume $n_{air} \approx n_{gas} \approx 1.00$. The refractive index for the window materials, high-density polyethylene (HDPE) and TOPAS, can be approximated as $n_{window} \approx 1.52$ within DESHIMA 1.0's frequency range. Using these refractive indices, the typical reflectivity for a single window interface (close to) normal incidence can be calculated as $R \approx 0.0452$, using Equation 2.55. Using Equation 2.44 and the phase shift based on frequency by Equation 2.38 the overall frequency spectra due to a typical window can be calculated. Figure 2.6 shows

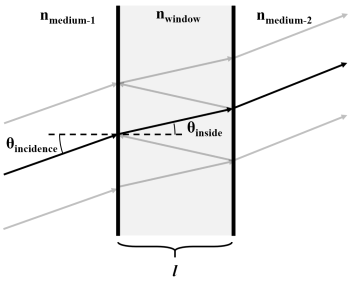

Figure 2.5: Illustration of a typical window behaving as a Fabry-Pèrot etalon of length l. The window with refractive index n_{window} separated two media with refractive indices $n_{medium-1}$ and $n_{medium-2}$. The angle of propagation inside the window θ_{inside} can be found using Snell's law of refraction and the angle of incidence $\theta_{incidence}$.

these spectra for a window of thickness 8 and 10 mm, including the effect of tilt or a lower reflectivity by applying an anti-reflective coating. The calculated spectra visualize the dependencies seen in the equations. An increasing window thickness reduces the free spectral range. A tilt increases the free spectral range (but is unnoticeable within the frequency range of the figure, except for its cumulative shift). A lowered reflectivity reduces the resonance intensity.

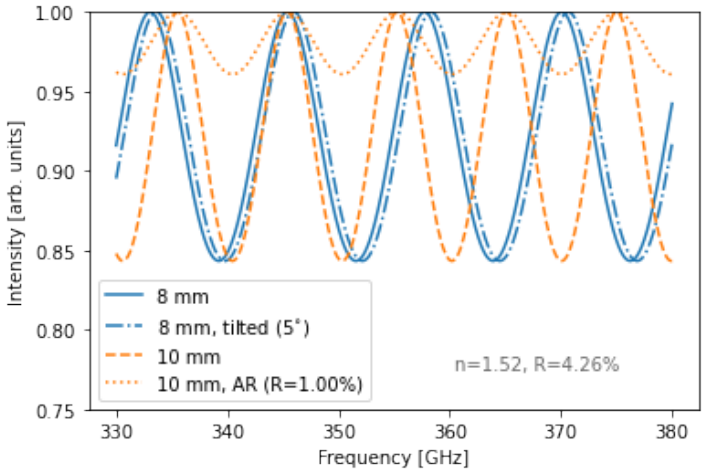

Figure 2.6: Calculated intensity spectra for the Fabry-Pèrot transmission of a window (n = 1.54, R = 4.26%) for the frequency range of DESHIMA 1.0. Notice how an increasing window thickness reduces the free spectral range. A tilt of the window increased the free spectral range, but it is unnoticeable within the frequency range plotted here except for its cumulative shift. A lowered reflectivity by applying an anti-reflective (AR) coating reduces the resonance intensity.

Note that the setup considered in this thesis is sensitive to a single polarization due to a linear polarizer in front of the detector, which only transmits radiation with horizontal polarization. The interfaces considered in this chapter and specifically the angles of incidence and refraction are all considered in the vertical plane. This is perpendicular to the polarization transmitted to the detector. Therefore, one has to consider that only s-polarised light is detected, which might counter some of the assumptions made. However, the impact of this negligible, since only small angles are considered. At small angles, the transmittance and reflectivity is expected to be similar to normal incidence and not strongly dependent on the polarization.

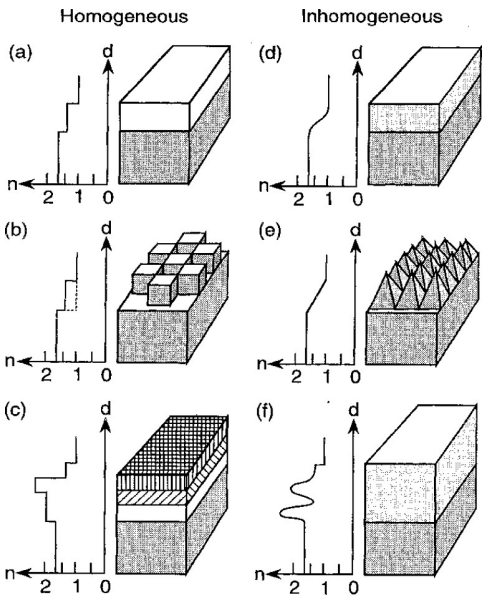

Figure 2.7: The different types of anti-reflective coatings divided into six groups based on two main properties, layer type and refractive index homogeneity of a layer. Each type has an indicative graph of how the refractive index could change over the depth of the anti-reflective coating. **(a), (b), (c)** Layers with a homogeneous refractive index, either single layered, patterned or multilayered, respectively. **(d), (e), (f)** Inhomogeneous refractive index in a layer, again either single layered, patterned or multilayered. Image from [15].

2.4. Anti-Reflective Coating

The previous section showed that to limit the optical resonances, one has to limit the reflectivity of interfaces (Equation 2.44). The reflectivity of an interface was shown to depend directly on the squared difference in refractive indices of the two media separated by the interface (Equation 2.55). In order to minimize the reflectivity of an interface, the 'step' in refractive indices needs to be reduced. Different methods to achieve this are covered in this section, with a focus on the frequency range of DESHIMA.

2.4.1. Types of Anti-Reflective Coatings

Since the reflectivity scales with the square of the step size of refractive index, any segmentation of the total step in refractive index from the starting medium to the intended medium will result in a lowered reflectivity. There are several ways to implement a smoother transition in refractive index. Here, the typical methods are introduced based on two main properties. The first one being the type of layering, either single-layered, multi layered or patterned. The second being the homogeneity of the refractive index of a layer, either homogeneous or inhomogeneous. These resulting six main categories are illustrated in Figure 2.7 by [15], where an indicative graph of how the refractive index would change over depth is also included. In general, designing an optimal anti-reflective coating is limited by the availability of materials with the necessary refractive indices within the operating frequency range. For further reading and a good overview of currently available types of anti-reflective coatings, as well as an overall source for the information here, see the review paper by [46].

Single Layer Coating

The simplest form of an anti-reflective coating is a single layer with a refractive index in between the start and target index applied on the interface. This aims to divide the total step in refractive index into two smaller ones, resulting in a reduced Fresnel reflection. Usually a material of $n \sim \sqrt{n_1 n_2}$ is taken to optimize the reduction of reflectivity with a single layer, since it allows for the minimal squared differences in refractive indices.

A special type of single layered anti-reflective coating is a quarter wave layer. This is a layer with an optical thickness of a quarter of the design wavelength. The reflections caused by both interfaces of the layer will destructively interfere. This eliminates the reflections that would otherwise cause the resonance profile. A quarter wave layer requires a very accurate layer thickness compared to the other anti-reflective implementations, since a different thickness will result in the destructive interference happening at different wavelengths. It is difficult to fabricate quarter wave layers that are useful for broadband operation.

Multiple Layered Coatings
Instead of dividing the step of refractive index once with a single layer, one can as well use multiple layers to smoothen the difference in refractive index even further. For optimal performance, one would then use $n_i \sim (n_1 n_2)^{i/m}$ as the refractive index of the i^{th} layer of a total of m layers, as to minimize the squared differences in between subsequent layers.

Inhomogeneous Layers
Some materials have an inhomogeneous refractive index, which can effectively operate as a gradient increase of refractive index, smoothing the refractive index even more than for any discrete amount of layers. These materials can as well be used in a stack of multiple layers to reach a target refractive index from the start index as smooth as possible.

Effective Medium Theory
In addition to layers of materials with the right physical properties, the effective refractive index can as well be custom-made. This is based on effective medium theory. When light interacts with periodic structures much smaller than its wavelength it will not diffract due to the gratings, but behaves regarding the overall 'effective' medium properties at the scale of its wavelength. For materials with inhomogeneities of sub-wavelength dimensions, the effective refractive index will take the form of the average [45]. An important requirement for the periodic grating structure is that the grating needs to be of sub-wavelength dimensions as to only allow the zeroth order diffraction to transmit through the grating. When higher orders are present, the grating will diffract in its conventional way, causing unwanted effects.

Effective medium theory has many applications. For example, the refractive index of a porous material with cavities of sub-wavelength size will take on an effective refractive index based on the material, the porosity, and the contents of the cavities. Sub-wavelength custom-fabricated gradient textures into an interface also results in an effective gradient transition between the two media. Effective medium theory allows for a range of possibilities regarding anti-reflective coatings.

2.4.2. Anti-Reflective Coatings for Terahertz Radiation

The implementation of anti-reflective coatings is limited by the availability of materials for the respective radiation spectrum of operation. Two well-used materials for optical components for terahertz radiation are high-density polyethylene (HDPE) and TOPAS, which have a similar refractive index in DESHIMA's frequency range at $n \approx 1.54$ [32]. To apply a single layered anti-reflective coating for the air interface, one would need a material with a refractive index of $n \sim \sqrt{1.54} \approx 1.24$.

Layered Coatings for Terahertz Radiation
Single layered coatings with a refractive index ~ 1.24 are unavailable for terahertz radiation [6]. Quarter-wave layers have been successfully made for terahertz radiation, but do not allow for the wideband operation of DESHIMA [59]. Coatings consisting of multiple homogeneous layers have been made and have shown interesting results for >1 THz, but not at the low terahertz range DESHIMA operates in [9]. Inhomogeneous layers that form a smooth transition between air and the transmission medium are unknown. Therefore, for this thesis work, the focus has been on a fabricated gradient texture employing the effective medium theory to obtain a smooth transition in refractive index.

An honourable mention for an anti-reflective coating using multiple layers onto HDPE for terahertz radiation is the work of Hargrave *et al.* [25]. They designed a multilayered coating of silicon and porous polytetrafluouroethane (PTFE) for which simulation show promising results for large coatings up to ~380 mm in diameter. However, the fabrication is complicated, and the simulated results are still showing a distinct standing profile in the transmission spectrum.

Fabricated Structures as Anti-Reflective Coating
A lot of research has been done on fabricated coatings for terahertz radiation. A conventional shape has been a one-dimensional or two-dimensional pyramid shape, but other grating shapes have been tested extensively [10, 41, 45, 46]. It was found that exponential or Klopfenstein tapered profiles performed better than the conventional linear (pyramid) taper [62]. However, linear profiles are still widely used due to a less complex and cheaper fabrication process. Anti-reflective coatings for terahertz radiation have also been made for materials unfit for direct milling, by bonding fabricated layers onto the optical component [20] or 3D-printing directly onto the surface [5].

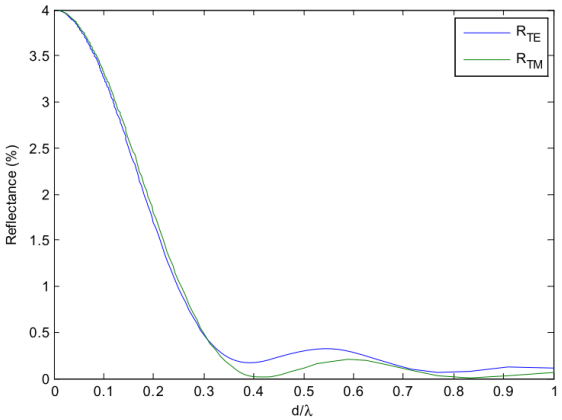

Figure 2.8: Reflectance versus the relative depth of a one-dimensional grating structure simulated by RCWA. Above $\sim 0.4d/\lambda$, the reflectance is reduced to <0.5% from the uncoated 4%. Note that the polarization of the incident radiation is not expected to be of distinct influence. Image from [6].

2.4.3. One-Dimensional Pyramid Grating as Anti-Reflective Coating

In this thesis work, a one-dimensional pyramid grating was used as an anti-reflective coating, since previous design experience with one-dimensional pyramid gratings was available in our group. Literature as well shows that a one-dimensional pyramid grating should work within DESHIMA's frequency range. The previous experience and the relevant literature are addressed in the next subsections. For more information on the final designed grating, see section 3.1.6. 'One-dimensional' relates to the directionality of the milled profile onto the window surface. It is important to note here that a two-dimensional pyramid profile is supposed to perform better according to simulations by Raguin *et al.* [45]. However, this would require the development of a new fabrication process.

Brückner *et al.* have done extensive computational and experimental research into one-dimensional pyramid gratings. They found that the sub-wavelength structures act as a bandpass filter, with the bandwidth depending on the periodicity and thickness of the structure. Furthermore, they found it to be important that the depth of the gratings is of comparable dimension as the wavelength in order to be 'recognized' by the incoming radiation. The incoming radiation would effectively treat too little depth as surface roughness instead [7]. In their work on one-dimensional pyramid gratings, they determined the requirement for the spatial grating period Λ to be

$$\Lambda \leq \frac{\lambda}{n_{air} + n_{window}}, \tag{2.57}$$

for an arbitrary angle of incidence. For angles close to normal incidence, the more relaxed $\Lambda \leq \lambda / n_{window}$ could be used. The period is therefore limited by the smallest wavelength of the design spectrum of operation. Based on computational modelling using Rigorous Coupled Wave Analysis (RCWA) they calculated the reflectance of the interface over increasing depth relative to wavelength, see Figure 2.8. The simulation in the figure also shows no strong polarization dependence in the transmitted profile, even though the grating itself is dimensional. From this modelling, their advice for the grating depth is to have

$$d > \lambda \tag{2.58}$$

for optimal performance, although the reflectance is reduced quite effectively already for $d > 0.4\lambda$ for both polarizations. Furthermore, Brückner advises an aspect ratio of $d/\Lambda = 2$ for sufficient mechanical stability and producibility by single-point diamond turning.

Previous Experience with One-Dimensional Pyramid Gratings in TOPAS

Extensive trials in fabricating one-dimensional pyramid gratings in a flat TOPAS sheet has already been performed by the Electronic and Mechanical Support Division (DEMO) at Delft University of Technology. These were commissioned by Campo *et al.* within our group for other sub-millimeter related research. Campo *et al.* (2019) [3] tried several methods to fabricate a one-dimensional pyramid grating into a 20x20x4.5 mm flat TOPAS sheet to fabricate a polarizer lens for sub-millimeter radiation [2]. Several methods with gear cutters were attempted, but resulted in fractured and uneven pyramid tips. The best approach was found by using a

rotating drill tip instead of a gear cutter. The caveat was that the drill tip required an additional 100 µm gap in between the pyramids. See figure 2.9 by Campo *et al.* for the results of several of the methods tried. With their best practices, Campo *et al.* were able to fabricate a one-dimensional pyramid grating of periodicity Λ = 550+100 µm, with drill angle $\alpha = 9.3°$ and depth $d \approx 1.3$ mm. Campo found no strong polarization dependent transmission for the one-dimensional pyramid grating, which agrees with the simulations of Brückner.

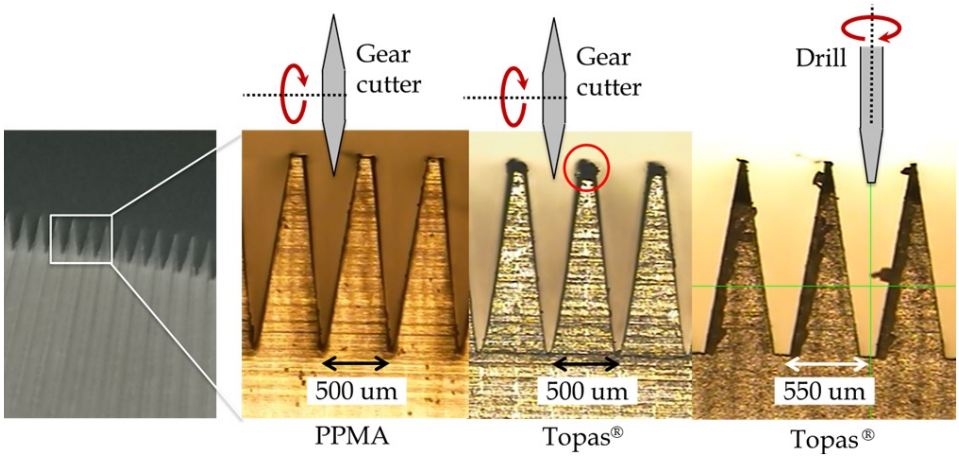

Figure 2.9: Images showing the results of several trials of creating a one-dimensional pyramid grating of sub-millimeter dimensions. Image by Campo *et al.* [3]. (a) Close-up of the one-dimensional pyramid grating. (b) Grating cut with a gear cutter in PPMA, which was deemed to be too soft for cutting the grating for the entire surface. (c) Grating cut with a gear cutter in TOPAS. Notice the fractures at the tips due to the fragility of TOPAS and the hard handling of the material by the gear cutter. (d) The final results for their optimum approach by Campo *et al.* A rotating drill with a flat 100 µm tip resulting in gaps of similar width.

An additional risk found by DEMO during and since these fabrication processes with TOPAS is the high risk of cracks. Internal stresses of TOPAS seem to be released during the fabrication steps. Even when resting in storage, the material was prone to crack over time. See figure 2.10 for several photographs of the typical cracks that occurred during fabrication and idle storage.

Figure 2.10: Several photos of a 2x19x24 inch 5013-L TOPAS sheet used for fabricating sub-millimeter optical components. Smaller pieces were cut from the corner. Over time during idle storage cracks appeared. The red zoomed section shows the sheet label with product information. The green zoomed section shows the corner where smaller pieces were cut from.

3

Experimental Setup

This chapter aims to cover all relevant operating information behind the gas cell setup and its measurements. The iterative research of increasing the setup stability over time required the testing of several versions of components into several versions of the combined gas cell setup.

- Section 3.1 will cover the lay-out of the setup. The technical details and different alterations of each component will be discussed. The section concludes with an overview of the setup versions used.
- Section 3.2 Measurement will cover the different types of measurements done with the setup. The executing procedures as well as the purposes of several calibration measurements are explained. The main gas emission spectrum measurement is covered. System stability measurements are also included.

3.1. Setup Overview

The measurement setup can be summarized into three main sections: (1) a gas source emitting the signal of interest, (2) a background to compare the source signal against, and (3) the detector to quantify the signal for further analysing. The gas source is made up of a low pressure gas at room temperature, chosen for an interesting emission spectrum in the frequency range of the detector used. The background is a blackbody submerged in liquid nitrogen for a stable emission reference. The detector used is the DESHIMA instrument, which is located inside a cryostat system. The room temperature gas emission compared to the relatively low flat emission of the background allows for visualization of the gas emission spectrum. The intensity of the gas radiation can be controlled by altering the gas pressure. See Figure 3.1 for a schematic representation of the main functionalities of the setup.

Aside from the gas source, background and detector, additional components are required. The room temperature gas is contained inside a high vacuum stainless steel flange with windows designed for transmission of sub-millimeter radiation. The flange is connected to a pressure control system to control a stable flow of the gas at the desired low pressures. The detector itself is inside a cryostat system to create the necessary low temperature environment for its superconducting properties to work. Multiple mirrors, a lens and an optical chopper are in place for optical coupling of all components. The optical chopper alternates between the on-source path (through the gas cell) and off-source path (alongside the gas cell). A third optical path departing from a room temperature background is present for calibration purposes. This third path can be joined with the main on-source path by changing the respective orientation of the two wire grid polarizers. One rotatable wire grid is located between the cold background and the front of the gas cell. Another is mounted onto the front of the cryostat.

3.1.1. Cryostat Systems

The DESHIMA detector itself is located inside a cryostat to bring it down to sub-Kelvin temperatures. Two cryostats were available in the lab and have been used with this setup. Both cryostats are refrigeration systems made by the company Bluefors. See Figure 3.2 for a photograph of each cryostat.

Hydra Cryostat

A horizontally oriented dilution cooler is available in the lab and primarily used with the gas cell setup. This system can be operated under different tilt angles and can reach temperatures as low as 20 mK at the detector.

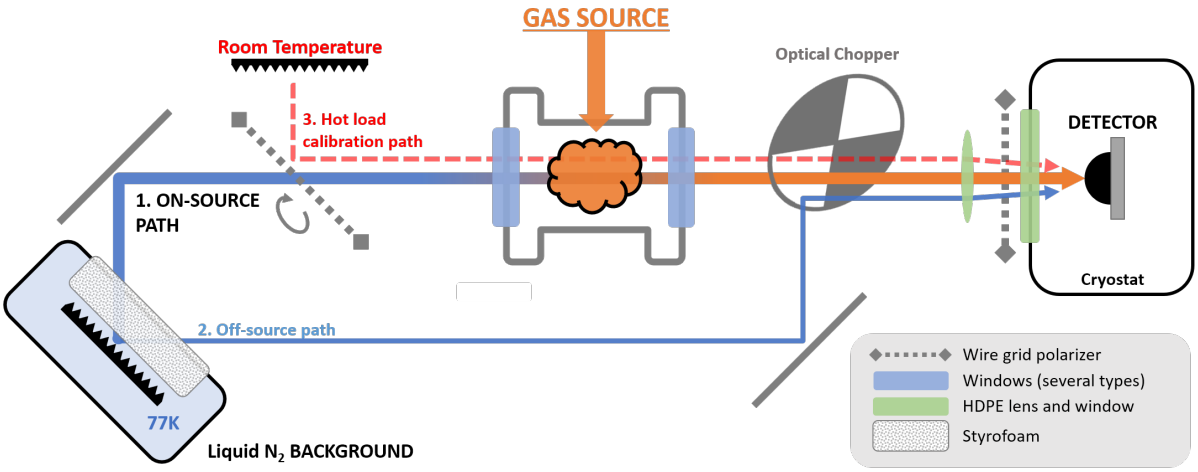

Figure 3.1: Schematic overview of the gas cell setup. The setup aims to detect the emission spectrum of a gas of interest using three optical paths. (1.) The on-source path (gradient blue orange) contains the room temperature gas inside a stainless steel flange at controllable low pressures. The gas emission is visible against the cold background. This background is a blackbody submerged in liquid nitrogen boiling at 77K. (2.) The off-source path (blue) is a direct path to the cold background. These two paths are rapidly alternated by the optical chopper. (3.) The hot load calibration path (red) is a path used for calibration purposes. The combined radiation of the transmitted on-source path and the reflected hot load calibration path can be controlled by altering the relative orientation of the two wire grid polarizers. The combined emission radiation is measured by the detector located in a cryostat system. To couple the radiation properly through the setup, several mirrors are used. The gas cell has removable windows. Different window designs and materials can be used. The setup is coupled to the detector in the cryostat by an HDPE lens. Note that the adjacent optical paths through the gas cell and after the chopper overlap in reality and are shown separately to discern the different paths.

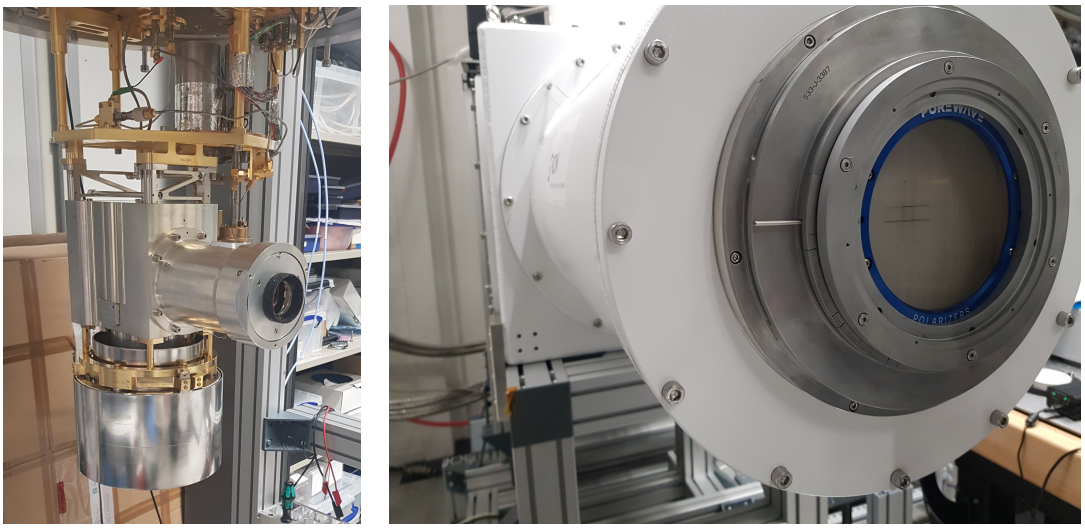

(a) (b)

Figure 3.2: Photographs of the two cryostat systems available in the lab to be used with the gas cell setup. (a) The vertical 'Beast' system with its outer casing removed. One can see the magnetic shield at the bottom and the optics aperture at the front. (b) The horizontal 'Hydra' system at close view. One can see the wire grid mounted in front of the cryostat, with the HDPE window directly behind the grid.

This cryostat is generally referred to as 'Hydra' and used at 100 mK with the DESHIMA prototype. It does not have a dedicated cold optical system for DESHIMA. Instead, a 'snout' has been designed for the DESHIMA detector to be mounted on. This snout brings the detector to the focal point of the coupling lens outside the cryostat system for improved optical coupling. The snout has been prone to resonate inside the cryostat, presumably affecting the read-out results. Later measurement runs have the snout removed to counter this resonance at the cost of lower optical coupling. See Figure 3.3 for several photographs of the snout.

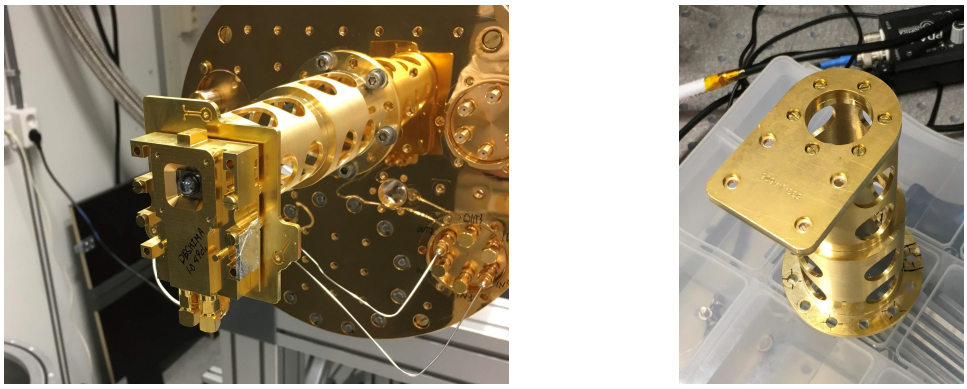

(a) (b)

Figure 3.3: Photographs of the snout used in the Hydra cryostat to bring the DESHIMA chip to the focal point of the lens of the gas cell setup for optimal optical coupling. **a** DESHIMA mounted on the snout, attached to the internal cryostat framework. **b** The snout component.

Beast Cryostat

A second cryostat is available in the lab. This sorption cooler is vertically oriented and has a dedicated optical system for DESHIMA inside the outer cooling compartment for optimal coupling to the detector. This cryostat is generally referred to as 'Beast' and can reach temperatures as low as 230 mK at the detector. This system was not used in this work, but several measurements by Zhang that are used for comparison have been obtained using this system.

Cryostat Quasi-Optical Filterstack

Both cryostat systems have a similar filter configuration, separating the DESHIMA detector from the outside environment. This filterstack creates an effective pass-band of 0 to 950 GHz. It filters stray light and forms an optical aperture into the sealed cryostat system. See [24] for in-depth information on the filterstack configuration. The filterstack consists of the following six layer types (ordered from outside to detector):

- HDPE window: An 8 mm thick high-density polyethylene (HDPE) window allowed for an airtight aperture with the outside environment, while retaining good transparency for sub-millimeter radiation.
- Thermal shader: A thermal shader by QMC Instruments Ltd. was placed to reduce the heating of the next filter layers. The shader consists of a thin metal layer on top of a thin polypropylene layer. It transmits sub-millimeter radiation with a sufficiently flat power spectrum, but reflects shorter wavelengths.
- RT-MLI: The Radio-Transparent Multi-Layer Insulation (RT-MLI), see [11], is a stack of several styrofoam layers which are to absorb radiation above 1 THz while transmitting radiation below 1 THz.
- Goretex sheets: Two Goretex foam sheets are to block radiation at visible light frequencies and also reduce infrared radiation. These further complement the RT-MLI in reducing the thermal load onto the subsequent metallic mesh low-pass filters.
- Several metallic mesh low-pass filters with sharp cut-off profiles in the low terahertz frequency range are used next to the Goretex sheets to limit the transmission to the frequency range of interest. These metallic meshes follow the design by [55] and can be conductively cooled to limit thermal radiation from the meshes themselves.
- Optional additional band-pass filters can be placed in the aperture of the inner cryostat stage to further reduce the radiation load onto the detector.

3.1.2. Wire Grid Polarizers

The setup contains two wire grid polarizers. One is located in between the gas cell and the background at a tilted angle to the optical path. Another is mounted onto the optical opening of the 'Hydra'-cryostat, or inside the cold optics in case the 'Beast'-cryostat is used. See Figure 3.4 for a side view of the gas cell setup, showing both wire grids.

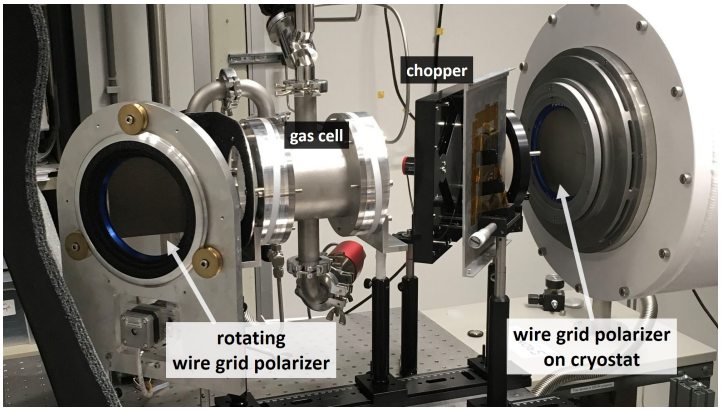

Figure 3.4: Side view of the gas cell setup. This view shows the rotating wire grid at the left of the photograph. One can see the casing with an electrical motor to rotate the wire grid. Behind the rotating grid, the room temperature blackbody can be seen mounted onto the gas cell. At the right of the photograph, one can see the wire grid mounted onto the 'Hydra'-cryostat. In between the gas cell, optical chopper, a mirror, and the lens can be seen.

Polarization Dependent Transmission of Wire Grids

The wire grid polarizer is one of the simplest linear polarizers. It consists of fine parallel equally spaced metallic wires in a plane. The spacing should be smaller than the wavelengths used. Electromagnetic waves with their polarization perpendicular to the metallic wires are propagated, while polarizations parallel to the wires are reflected. In practice, a small amount of radiation will be absorbed by the wires, but this is considered negligible for the scope of this setup.

Two Wire Grid Polarizers for a Controllable Background

The wire grid mounted on the aperture of the cryostat is aligned with the polarization of the antenna in the DESHIMA instrument. It serves as a polarization filter, only transmitting light of the antenna's polarization and limiting other polarization from entering the cryostat setup. The second polarizer is located in between the gas cell and the cold background, with its plane at 45°to the optical path. This wire grid is inside a frame that allows the grid to be rotated, controlled by a Raspberry Pi board. It serves as a beam splitter, transmitting light from the liquid nitrogen background and reflecting light from the blackbody at room temperature alongside the main optical path. The ratio of hot and cold background light depends on the rotational angle of the wire grid relative to the wire grid mounted onto the cryostat. The two wire grids together allows for a controllable background brightness temperature, which is useful to calibrate the frequency shift of the MKID's resonating frequency to a brightness temperature. For more information on this calibration measurement, see subsection 3.2.2. For more information on the formulae behind it, see subsection 4.2.

3.1.3. Optical Lens

An optical lens is located in between the cryostat polarizer and the optical chopper. The lens couples the radiation passing trough the setup to the detector inside the cryostat. The radiation through the setup is assumed to be parallel to the optical axis. The lens is placed a distance equal to its focal length from the detector. The lens is made of high-density polyethylene (HDPE) with a focal length of $f = 208.12$ mm and has an effective diameter of 82 mm.

3.1.4. Optical Chopper

An optical chopper is located between the gas cell and the coupling lens. It combines both optical paths the gas cell path and the background path by alternating transmission and reflection at its aperture. See Figure 3.5 for a schematic representation and a photograph of the optical chopper used. The optical chopper

consists of a rotating reflecting circular disc with a diameter of 70 mm in a 200x200 mm casing. The disc has two opposing quarters as windows with linear edges. An aperture of 70 mm is located in one of the quadrants of the chopper casing. The angular frequency of the chopper can be controlled. When the chopper is placed at 45° to the optical path, the chopper can be used as an instrument to alternate two optical paths.

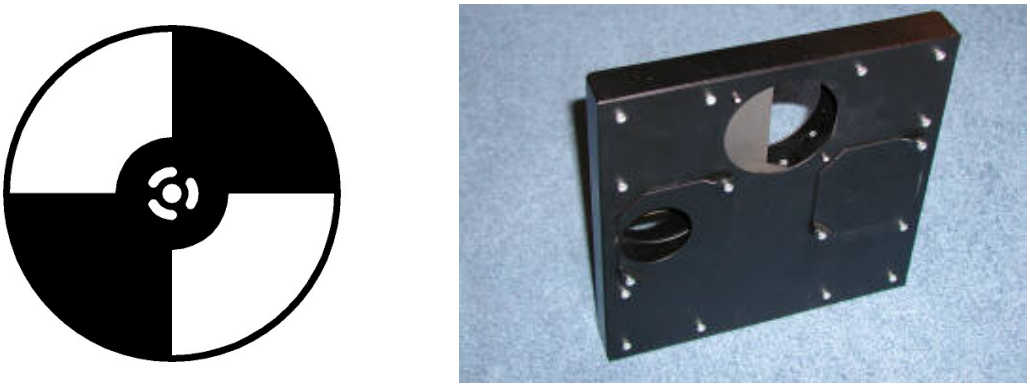

(a) (b)

Figure 3.5: **a** Schematic illustration of the two-winged disk used as the optical chopper. **b** Photograph of the disk inside its casing. Apertures in the casing of several sizes can be seen. Note, one side of the casing was removed in operation with the gas cell setup to increase the effective aperture. Both images are from the manufacturer Scitec Instruments Ltd.

For the chopper type used in this experiment, the expected transmission profile can be calculated based on the design angles [16]. The angle of the windows α and angle of the wings γ are equal $\alpha = \gamma = \pi/2$ rad. The casing aperture angle is approximately $2\delta \approx \pi/3$. One can find the characteristic time intervals for full reflection t_0, full transmittance τ and the overlapping interval τ_t as

$$t_0 = \frac{\gamma - 2\delta}{\omega}, \tag{3.1}$$

$$\tau_t = \frac{2\delta}{\omega}, \tag{3.2}$$

$$\tau = \frac{\alpha - 2\delta}{\omega}, \tag{3.3}$$

where full coverage of parallel radiation was assumed onto the casing aperture. If one would place the chopper in a Fourier plane of the setup, the transmission profile would resemble a top hat profile. For the typical experiment with 10 Hz chopping, one would have $t_0 = \tau \approx 1/120$ s and $\tau_t \approx 1/60$ s, resulting in a trapezoid-like profile, see Figure 3.6.

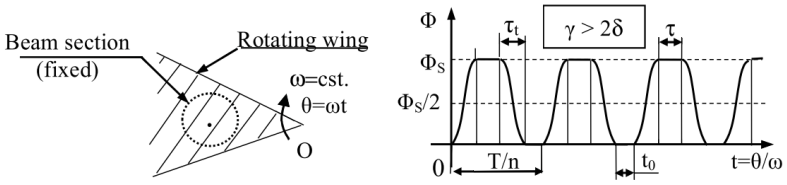

Figure 3.6: Expected trapezoid-like transmission profile for a chopper with n linear wings of angle span γ larger than its circular aperture of angle span 2δ. The profile shows a rotation with period T and the characteristic time intervals: full reflection t_0, full transmittance τ and the overlapping interval τ_t. Cropped image of original by [16].

To investigate the chopping frequency stability over time, the instantaneous frequency was calculated for run 890 using the Hilbert transform demodulation, see section D.1. This instantaneous frequency is an accurate representation of the chopping frequency when the instantaneous frequency is average over slices longer than the chopping period (~0.1s). Figure 3.7 shows the 2-second-mean of the instantaneous frequency over time. The chopper frequency averaged over time for run 890 showed a mean frequency of 10.365 ± 0.008 Hz. The chopper frequency is considered sufficiently stable.

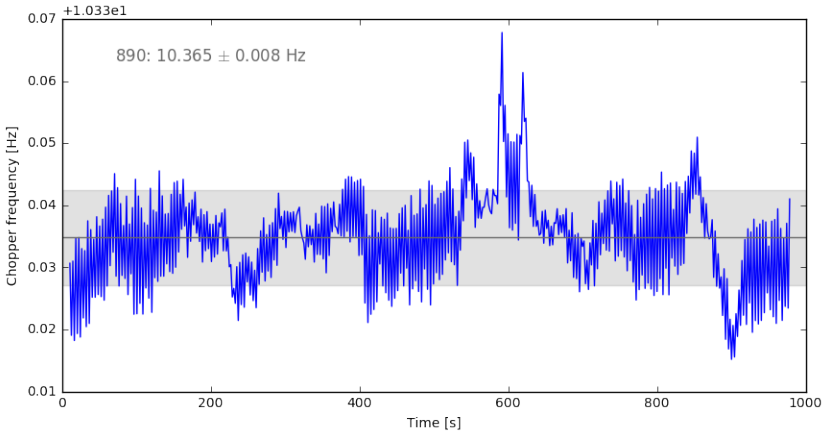

Figure 3.7: Chopper frequency over time during the 1000s empty gas cell run 890. The chopper frequency is obtained by taking the mean of every two second data slice of the instantaneous frequency obtained using Hilbert transform demodulation. The chopper frequency over run 890 showed a mean frequency of 10.365 ± 0.008 Hz.

3.1.5. Gas Cell and Window Holders

The gas cell forms the central part of the setup, as it contains the gas of interest. The gas cell consists of a 100 mm long stainless steel cylinder with a 100 mm diameter. In the middle of the cylinder three openings are located at 90° to each other for in- and outflow of the gas and pressure measurement. Both ends of the cylinder have flanges of 160 mm with threaded holes to mount the window holders. The flanges have a groove for a rubber O-ring for high vacuum sealing. The window holders each consist of two stainless steel discs with another groove and O-ring in between. Clamping the window in between the two discs allows for a 5° inward orientation to limit reflections in the gas cell cavity. The windows can also be mounted vertically by clamping the window directly in between the gas cell cylinder and the stacked discs. See Figure 3.8 for several photographs of the stainless steel gas cell and window holders.

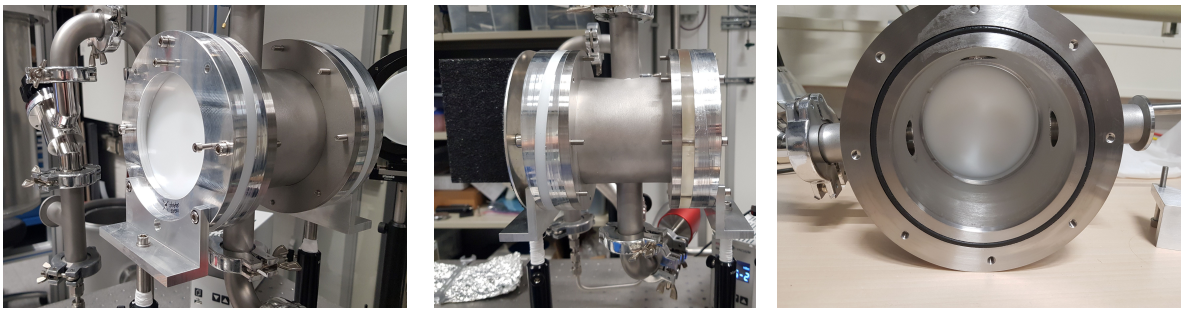

(a) (b) (c)

Figure 3.8: Photographs of the stainless steel gas cell. (a) Angled side view of the gas cell with HDPE windows mounted at 5° opposing each other. One can see parts of the pressure control mounted onto the gas cell. (b) Side view of the gas cell. On its left side, an HDPE window mounted at an angle. On its right side, a TOPAS windows mounted vertically. One can see the room temperature blackbody mounted onto the left side of the gas cell. (c) Front side without the window holder and window. The rubber O-ring and screw holes for high vacuum sealing are visible. One can look inside the gas cell cylinder and see the three openings at 90° to each other for the pressure control.

3.1.6. Gas Cell Windows and Anti-Reflective Grating

For the windows of the gas cell, two alterations were used: a circular flat 8 mm HDPE window and a 10 mm thick TOPAS window with anti-reflective coating. Both windows have a diameter of 160 mm, equal to the gas cell flanges and window holders. Aside from the gas itself, the windows are the main optical media for the radiation to pass through in the on-source path. Any aberrations caused by the windows will not be cancelled out by the chopping method and will affect the results.

Windows Causing Standing Waves in the Frequency Spectrum
The HDPE windows are believed to be the main cause for the standing wave visible in the spectrum results of the gas cell setup. The reflecting interfaces make the window cavity essentially a Fabry-Pèrot interferometer. See section 2.3 on optical resonance and Fabry-Pèrot cavities. The standing wave was found to be limiting the detectability of low pressure emission spectra with the setup.

Anti-Reflective Pyramid Grating in TOPAS
To counter the reflections causing the standing wave, an anti-reflective (AR) layer was needed for the window interfaces of the gas cell. Conventional applied AR-coatings are limited for sub-millimeter radiation, see section 2.4 for more background theory on anti-reflective options in the sub-millimeter frequency range. A sub-wavelength grating was therefore fabricated into the surface of the windows.

The design of the grating was selected to be a one-dimensional pyramid grating in a TOPAS sheet. This design choice follows on the experience by Campo *et al.* (2019) [3] in fabricating stable one-dimensional pyramid gratings, and the proof of concept that these gratings are effective anti-reflective coatings for sub-millimeter radiation by Brückner (2007) [6].

The gratings were fabricated into TOPAS as previous experience with HDPE found it to be too soft for machining the sub-wavelength structures. TOPAS® is a cyclic olefin copolymer (COC) made by the company TOPAS Advanced Polymers. TOPAS is supplied in several grades, each with different material properties. In both Campo's and this research, TOPAS 5013-L was used. According to the company's documentation [54], this grade is best for the fabrication of optical components.

Pyramid Design Constraints for the Frequency Spectrum of DESHIMA
Brückner *et al.* have done extensive research on gradient gratings as anti-reflective layers for sub-millimeter radiation, including pyramid shaped gratings [6]. Brückner *et al.* proposed the following design criteria for an effective one-dimensional pyramid grating in TOPAS:

$$\Lambda \leq \frac{\lambda}{n_{window}}, \tag{3.4}$$

$$d \gg 0.4\lambda, \tag{3.5}$$

where the grating periodicity Λ should be shorter than the effective wavelength inside the window material, and the grating depth should be larger - preferably much larger - than 40% of the vacuum wavelength. For more information on these criteria and an overview of Brückner's work, see section 2.4.3. DESHIMA 2.0 is designed to have a frequency range of 220-440 GHz. The design criteria for the pyramid grating are therefore roughly

$$\Lambda < 450\ \mu m, \tag{3.6}$$

$$d \gg 550\ \mu m. \tag{3.7}$$

Pyramid Grating Design for the Gas Cell Windows
To follow the previous best practices by Campo, a similar design was adapted for the design criteria by Brückner. This was done by using the same drill tip - and drill angle - and down scaling the design. The design has a drill angle α = 9.3° and gaps of 100 µm in between the pyramids. The pyramids themselves have a base width of 350 µm. Combined, the profile therefore has a periodicity Λ = 350 + 100 = 450 µm. This design resulted in a grating depth of roughly 1 mm. The 450 µm periodicity is at the boundary of Brückner's criterion. This is believed to be sufficient, since the pyramids themselves are of a smaller 350 µm width. The flat 100 µm pyramid base will cause a steep increase in effective refractive index at the grating-sheet boundary. The effects of these gaps are considered not worth additional trials in machining methods. The remaining gradient is expected to still be an improvement compared to no grating.

The high risk of cracks due to internal stresses as found by DEMO limits the surface area size to be milled. A balanced surface area had to be found that covers a sufficient area of the beam profile and has an acceptable low risk of causing cracks. A circular area of 60 mm in diameter centered onto one side of the TOPAS windows was expected to be stable. The drilled surface area divided by the sheet thickness is of the same order of magnitude as for the stable 20x20 mm sheets drilled for Campo's work. GRASP simulations by Zhang showed the diameter of 60 mm to contain the main beam up until a ~30 dB level, allowing for acceptable beam propagation reaching the anti-reflective grating. See Figure 3.9 for a schematic drawing of the final design.

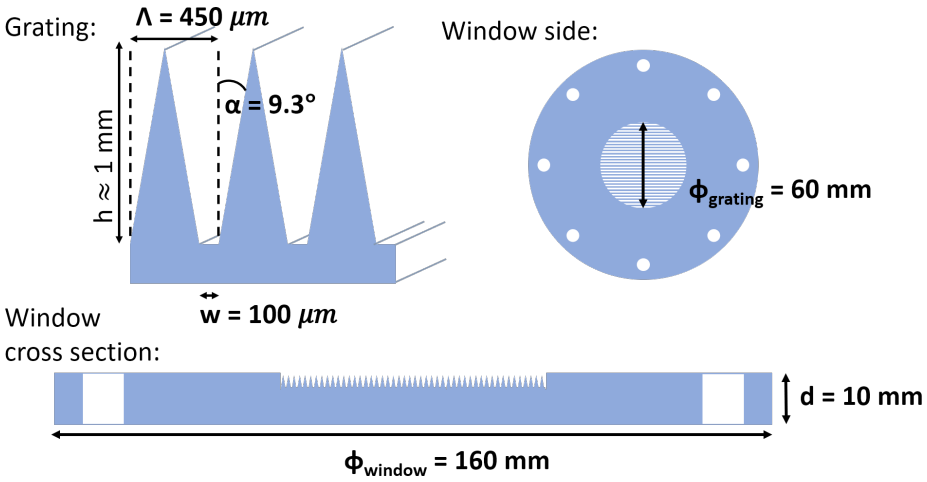

Figure 3.9: Schematic of the pyramid grating design as anti-reflective coating onto the TOPAS windows. **Left**: The one-dimensional pyramid design of spatial period Λ=450 µm following the drill tip angle of α=9.3° and drill tip width of w=100 µm, resulting in a grating height of approximately $h \approx 1$ mm. **Right**: Side view of the design with the grating milled for a centered circular surface of diameter ϕ=60 mm. Note the grating is aligned with opposing screw holes for ease of alignment of the pyramid grating orientation. **Bottom**: Cross-section view of the design. The grating is drilled into the 10 mm thick TOPAS sheet on one side to limit releasing internal stresses that might cause cracks in the sheet during fabrication or idle storage.

After a failed first attempt with the grating on both sides, a second successful attempt was done with less mechanical loads onto the TOPAS material. See Appendix C for the first fabrication trial. The second attempt had the grating in one side only, and several intrusive 'cleaning' steps in the fabrication procedure were skipped. This resulted in an uncracked grated window, which has been used in further testing and experiments with the gas cell setup. The single side grating instead of both sides is believed to still cancel the standing wave profile effectively that would occur in flat untreated windows. Reducing the reflectivity on one side instead of both should still hinder optical resonance inside the window cavity. See Figure 3.10 for photographs of the final windows with grating.

(a) (b)

Figure 3.10: Photographs of the successful trial to fabricate the designed anti-reflective pyramid grating onto the TOPAS window on a single side only. (a) The window showed no cracks after fabricating the grating on one side. The screwing holes used for clamping have red ink next to them. (b) A close up photograph of the grating. The one-dimensional pyramid grating can be seen.

3.1.7. High Vacuum Gas Cell Pressure Control

The gas pressure inside the gas cell is controlled by a high vacuum system, which can be divided into three sections, each connected to one of the three openings in the middle of the gas cell cylinder at 90° to each other. One is connected to the gas supply line with several precision valves in between the supply line and the gas cell. This allows for accurate control of the supplied gas. The second opening is connected to a high vacuum pump. The pump combined with the accurate supply control allows for a stable flow at a desired

pressure. The third opening is connected to a digital pressure gauge, a capacitance diaphragm gauge made by Pfeiffer Vacuum, capable of detecting pressures as low as 10^{-3} mbar. All valves are controlled manually. Therefore, there is no active control and feedback loop of the gas pressure during measurements. A stable pressure is achieved by adjusting the opening of the valves until the desired pressure was seen on the live pressure read-out. This combined high vacuum gas cell pressure control allows for a stable gas flow from atmospheric pressured down to 10^{-3} mbar. The pressure can likely be even lower, but is currently limited by the lower bound of the digital pressure gauge.

Gas Pressure Stability over Time

The pressure of the gas is of influence to the detected output, since the emission brightness temperature of the gas scales with pressure. The stability of the gas pressure is therefore important for the stability of the results. A high fluctuating pressure would directly impact the brightness temperature detected. Figure 3.11 shows the gas pressure over time for two 0.5 mbar nitrous oxide runs. The measurements were started when the pressure seemed stable from the live pressure read-out. However, as one can see in the Figure, the setup was still stabilizing for up to 20 minutes. To minimize the impact of pressure drifts, a stabilization period of 10 to 20 minutes was implemented after the gas pressure seemed stable from the live pressure read-out. The Figure also shows that each run would slightly differ in pressure, since a stable pressure was obtained by manual control of the valves based on the live pressure read-out.

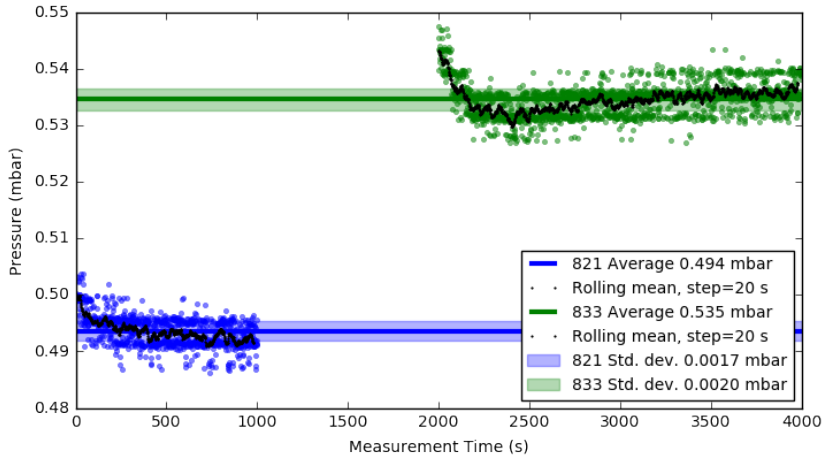

Figure 3.11: Gas pressure over time for run 821 and 833. Both are 0.5 mbar N2O runs of 1000 and 2000 seconds, respectively. The pressure over time shows a stabilization period of up to around 20 minutes after start.

3.1.8. Optical Mirrors

The setup uses two flat aluminium mirrors, one in each optical path. A small circular mirror of ~10 cm diameter is located in the main path directly after the background, reflecting the background onto the rotating wire grid. A larger mirror (175x225 mm) is located in the 'direct' background path, coupling the chopper to the background. Considering the relatively large wavelengths for sub-millimeter radiation, the flatness of both mirrors is assumed to be sufficient. Aluminium mirrors typically allow for >99% reflectivity [39], and the thermal emission is assumed to be flat in the frequency range of DESHIMA. Absorption and re-emission features due to the mirrors are therefore assumed to be negligible. The mirrors were generally aligned once per measurement session to aim both optical paths onto the same spot of the background blackbody.

3.1.9. Hot and Cold Blackbody Backgrounds

There were several hot and cold blackbody backgrounds used in the different versions of the setup. In general, the backgrounds can be divided into two categories: (1) reference backgrounds (hot and cold) used for the on- and off-source optical paths to image the gas emission, and (2) the calibration background (hot) used for the room temperature calibration during the rotating grid measurement.

Reference Background: Liquid Nitrogen High Precision Calibration Target (PT-V1)
The primary background that was used as the reference background for the main optical paths is the liquid nitrogen cooled high precision calibration target (PT-V1) developed by RPG-Radiometer Physics GmbH. This calibration target consists of a blackbody vertically inside a cavity of a white polystyrene foam block, see as well 3.12. The block is inside an aluminium casing which has two open 210x210 mm 'windows' on opposing sides. The polystyrene foam behind the window has an anti-reflective coating to limit any reflections and standing waves in its transmission spectrum. These anti-reflective layers have either slight horizontal or vertical polarization effects according to the supplier. The specifics of the anti-reflective layers or the exact polystyrene material are not given. The supplier claims the polystyrene foam in front of the blackbody to be 100% transmitting for sub-millimeter radiation up to 200 GHz. Higher frequencies have not been teste. The precision of the blackbody brightness temperature when filled with liquid nitrogen is claimed to be differing ~0.1K from the boiling temperature, with a repeatability of 25 mK.

For the gas cell setup, the calibration target its foam is assumed to be fully transmitting for the range of DESHIMA (up to 440 GHz). This is in agreement with research suggesting polystyrene foam to be an excellent candidate for use as a substrate with sub-mm radiation [64].

One can obtain a stable 77K or room temperature background using this calibration target by either filling the cavity with liquid nitrogen or leaving it in room temperature air. Note that the target is designed only for operating with liquid nitrogen at 77K.

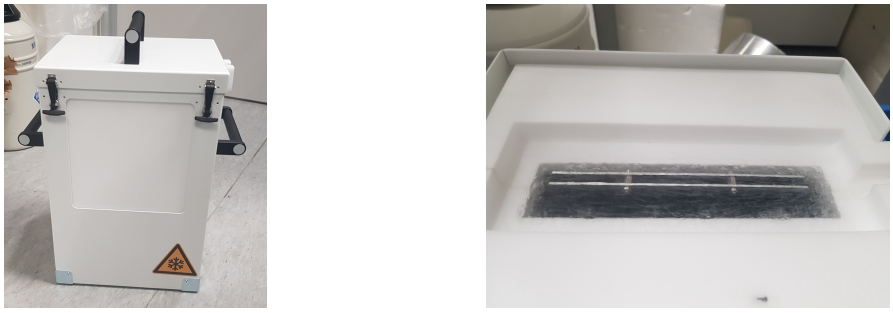

(a) (b)

Figure 3.12: Photographs PT-V1 calibration target. (a) Side view of the target. One can see the open windows in the aluminium casing, showing the polystyrene foam block inside. (b) Top view of the target with the aluminium lid removed. One can see the cavity in the polystyrene foam block with the blackbody background inside. The cavity is filled with liquid nitrogen, which can be seen boiling at the liquid-air interface.

Reference Background: Liquid Nitrogen Buckets
In the adopted version of the setup, the two main optical paths each had their own liquid nitrogen background. These backgrounds consisted of a bucket with a blackbody coating filled with liquid nitrogen. A mirror at 45° to the ground reflected the radiation into the horizontal plane of the setup. These separate backgrounds had the advantage that the setup on the optical table could be spacious and was easier to align, at the risk of having drifts among the background temperatures. For a photograph of the old setup using two buckets with angled mirrors, see Figure 3.13.

When using this background setup, one is using the direct liquid nitrogen to air interface as a background. This interface is rather unstable due to the boiling behaviour at the interface. These instabilities are believed to be of high frequencies and might be of no concern when integrating over several seconds. However, with the chopper alternating the two backgrounds, this could contribute to noises. In addition, the condensation on the mirror directly above the buckets might affect the reflectivity of the mirror. Note that the liquid nitrogen to air has a fundamental 0.8% Fresnel power reflection coefficient, since liquid nitrogen has a refractive index of $n = 1.2$ [4]. Although the reflectivity is low, this could cause additional resonance effects. See the extensive liquid background accuracy analysis by Maschwitz *et al.* [37] and Küchler *et al.* [35] for more information on typical accuracy limiting aspects when using liquid nitrogen as a direct background for the calibration of microwave systems.

Liquid Nitrogen Dissipation and Temperature Drift
One has to consider the dissipation of liquid nitrogen when working with backgrounds dependent on being submerged in liquid nitrogen. The dissipation over time limits the length of a measurement before needing

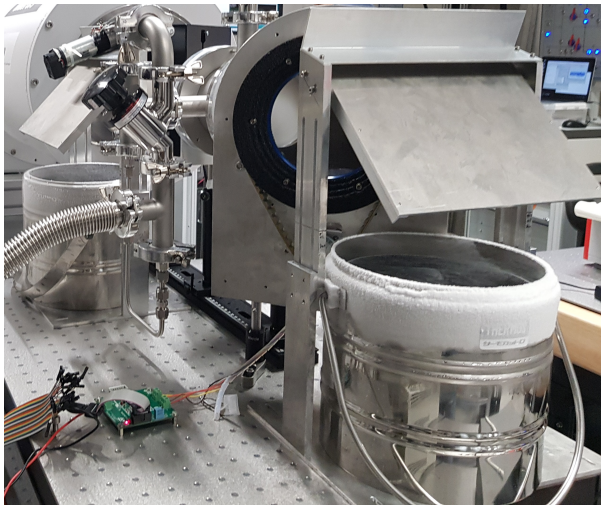

Figure 3.13: Photograph of the previous version of the gas cell setup as designed by Zhang. The photo shows the two separate buckets filled with liquid nitrogen used as backgrounds of the on- and off-source paths. A mirror angled at 45° to the ground was placed above the buckets to couple the backgrounds to the setup.

to refill. Even when refilling the liquid nitrogen regularly, any exposed blackbody partly sticking out above the liquid-air interface will slowly heat and cause the overall temperature to drift upward.

An approximation of a typical temperature drift to expect can be made with the model by Paine *et al.* (2014) [43] for the first 25% of dissipation:

$$\frac{d}{dt}\Delta T = a\left(\frac{d}{dt}\frac{\Delta V}{V_0}\right), \tag{3.8}$$

$$\frac{d}{dt}\frac{\Delta V}{V_0} = \frac{1}{h_0}\frac{dh}{dt}, \tag{3.9}$$

where the rate in temperature change ΔT over time is found to be approximately constant and a factor $a = -1.2$K related to the rate in change of relative volume. The rate of change in relative volume was found to be equal to the rate of liquid nitrogen level dissipation, assuming a vertically consistent shape.

For the calibration target PT-V1 with a starting level of approximately $h_0 \approx 30$ cm and a typical dissipation rate measured as $\frac{dh}{dt} \approx$ -6 cm per 90 min, one could expect a typical temperature drift of ~0.044 mK/s. Note that this is only an indicative value for the temperature drift due to liquid nitrogen dissipation. The assumptions made, and the model used, do not allow for accurate drift calculations.

Reference Background: Eccosorb Sheets

In some experiments, a large sheet of Eccosorb microwave absorber was used as a room temperature background. Several similar sheets of different sizes were available in the lab. The flexibility of these sheet allowed for an easy use and made it ideal for system check and noise measurements, see as well subsection 3.2.4 on these measurements.

Calibration Background: Room Temperature Blackbody Mounted on Gas Cell

The calibration background used for the room temperature calibration during the rotating grid measurement consists of an L-shaped sheet with a blackbody coating. One of the sides has a 95 mm aperture and is mounted directly onto the gas-cell window holder, see Figure 3.8 (b).

3.1.10. Main Setup Versions

This subsection will cover the main two versions of the setup and aims to give a general idea which component alternations were generally used in a combination as a single setup.

Single Background Setup

The most used setup in this research consisted of a single background setup with the Hydra cryostat. This setup was solely used with nitrous oxide (N_2O) gas. The use of a single background allowed for a stable setup

that is less prone to temperature differences occurring among separate backgrounds. The liquid nitrogen PT-V1 calibration target was used as the single background for both on- and off-source optical paths. The Hydra cryostat was used both with and without the snout. The snout allowed for better coupling between detector and setup, but touched the stage casing at times, resulting in read-out errors. The gas cell was used with both HDPE and TOPAS windows. This setup therefore allowed for detailed analysis of the effect of window type and overall stability.

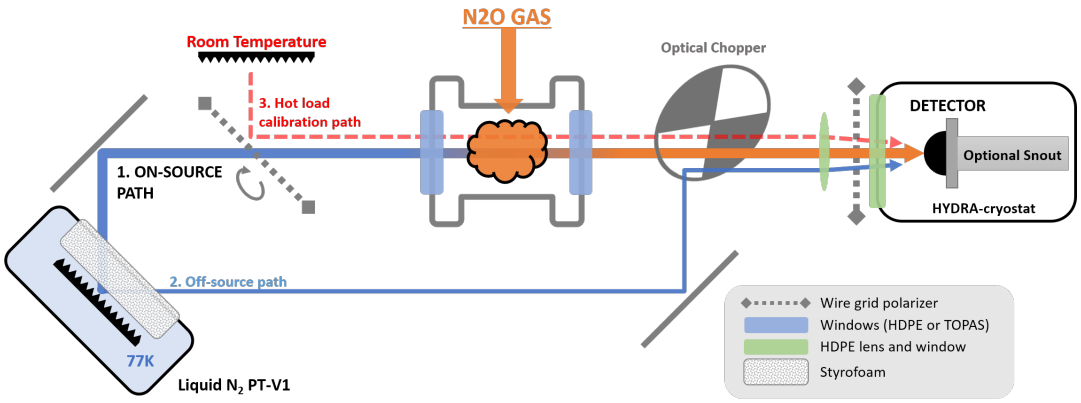

Figure 3.14: Schematic of the single background setup. The PT-V1 allowed for a 210x210 effective background size, which can be used to focus both main optical paths onto. The DESHIMA detector was usually mounted onto a snout for better optical coupling with the lens outside the cryostat system. The setup was solely used with nitrous oxide gas. Both HDPE and TOPAS gas cell windows were used. Note that the adjacent optical paths through the gas cell and after the chopper overlap in reality and are shown separately to discern the different paths.

Double Background Setup

The first measurements as part of this thesis work were done on a double background setup. The double background consisted of two buckets with a blackbody coating inside, filled with liquid nitrogen. The upward radiation was coupled to the setup via mirrors angled at 45°to the ground. Drifts between the separate backgrounds affected the stability of the read-out results. All windows were made of HDPE. Measurements were done with nitrous oxide and the Hydra cryostat with snout. Older measurements by Zhang were also performed with this setup, but used the Beast cryostat and methanol (CH_3OH) gas.

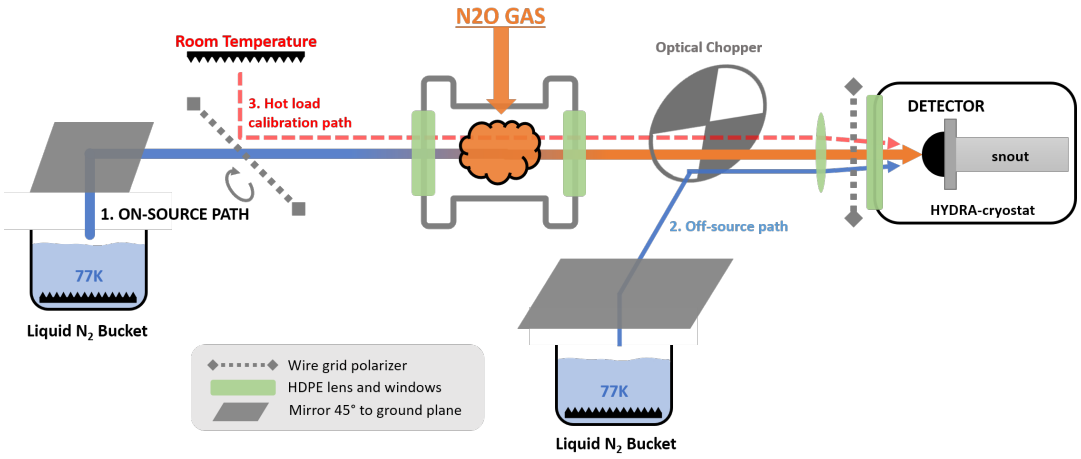

Figure 3.15: Schematic of the double background setup. The two buckets allowed for a flexible setup at risk of temperature drifts between the two main optical paths. The DESHIMA detector is mounted inside the Hydra cryostat with snout for better coupling. This setup was solely used with HDPE gas cell windows. Measurements were done with nitrous oxide. Older measurements by Zhang used a similar setup with methanol gas and the Beast cryostat. Note that the adjacent optical paths through the gas cell and after the chopper overlap in reality and are shown separately to discern the different paths.

3.2. Measurement

Several types of measurements were done with or related to the gas cell setup. A regular measurement to detect the gas emission spectrum can be done once two calibration measurements have been executed. The two calibrations measurements are required to generate a brightness temperature spectrum with the DESHIMA detector. Subsection 3.2.1 will cover the terahertz frequency sweep measurement where the MKID respective filter responses are calibrated. Subsection 3.2.2 will cover the rotating grid calibration used to calibrate the detector response to a brightness temperature. The proceedings of a regular measurement are covered in subsection 3.2.3. Subsection 3.2.4 will cover the proceedings of a stability measurement. This measurement is intended to evaluate the setup stability over time and allows for detailed stability analysis of changes to the setup. For an overview of all measurements done as part of this research, see Appendix A

3.2.1. Terahertz Frequency Sweep Measurement for Filterbank Calibration

The terahertz frequency sweep measurement is a measurement to calibrate the on-chip filterbank central frequencies and their wideband response. These sub-millimeter wave filters are each coupled to the transmission line connected to the twin slot antenna of the detector and a single MKID. See section 1.1.2 for more information on the on-chip design.

This calibration measurement does not use the gas cell setup. A photomixing terahertz continuous wave source (Terabeam 1550 made by Toptica Photonics) is used as the terahertz source sweeping over the DESHIMA frequency range. The minimum power of the Terabeam 1550 is too high, therefore the signal is attenuated by 24-25 dB by passing the beam through a Mylar beam splitter. See figure 3.16 and the DESHIMA design paper by Endo *et al.* (2019) [17] for more information on this filterbank calibration measurement. The obtained frequency response profiles per filter-MKID couple are fitted to a Lorentzian profile to obtain a measured central frequency and quality factor per filter.

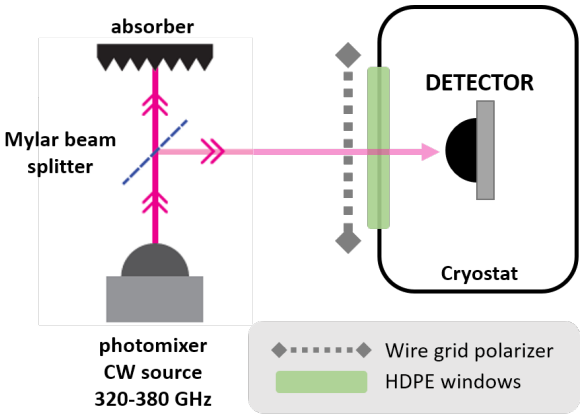

Figure 3.16: Schematic of the terahertz frequency sweep measurement. A photomixing terahertz continuous wave source scans over the DESHIMA frequency band. To reduce the power of the source to typical levels, a Mylar beam splitter is used to couple the line source to the detector in the cryostat system. The image is edited from the original by [17].

The Terabeam 1550 by Toptica Photonics is believed to have a frequency offset of up to 2.0 GHz, as described in the specifications by the company. This limits the accuracy of the terahertz frequency sweep measurement. The gas emission spectra of the cell setup can be used to find this offset and improve the overall filterbank calibration. See section 1.2 as this is part of the motivation behind this research.

3.2.2. Rotating Grid Measurement for Brightness Temperature Calibration

The rotating grid measurement is used to calibrate the MKID response (shifts in resonance frequency) to a brightness temperature.This calibration is performed with the gas cell setup and typically done once before a series of regular measurements. As the name suggests, this calibration measurement is based on altering the relative orientation of the wire grids. There are two wire grids in the setup, one at fixed orientation mounted onto the cryostat and a rotatable one between gas cell and background, see also subsection 3.1.2. The second wire grid is electronically rotated inside its casing. Depending on the angle between the rotating wire grid and the fixed wire grid, the ratio of transmitted light from the cold liquid nitrogen background and the hot room temperature blackbody is controlled. In this way, any brightness temperature between the cold and hot

background temperatures can be achieved. To detect the brightness temperature with little disturbances, no gas is supplied to the gas cell, and the gas cell is brought to high vacuum ($< 10^{-3}$ mbar). The chopper is on at 10 Hz.

This measurement is generally done for 100 seconds with the rotating wire grid at a speed of one rotation per 13 seconds. Extensive fitting to the expected profiles based on theory is done to obtain the response calibration. For more information on the fitting and brightness temperature calculation, see subsection 4.2.

3.2.3. Gas Spectrum Detection

The gas spectrum detection measurement aims to detect the emission spectrum of the supplied gas. This is done by alternating the on- and off-source paths with the optical chopper. The brightness temperature corresponding to the signal of each MKID is obtained by the fitting parameters from the rotating grid measurement. The filter center frequencies corresponding to the MKID detectors are obtained by the terahertz frequency sweep measurement.

A gas spectrum measurement can be done for any length of time, but one has to take care of the liquid nitrogen evaporation. The declining level of liquid nitrogen causes the blackbody background to increase in temperature. Typically, stability measurements up to several hours were realistic on a single liquid nitrogen filling without noticing dominant background temperature drifts due to liquid nitrogen evaporation. Spectrum measurements with gas have been done for measurement times of up to 2000 seconds.

The gas pressure needs time to stabilize for the desired low pressures. Analysis of the pressure behaviour of the gas cell, see section 5.2.3, showed that millibar gas pressures in the gas cell typically need up to 20 minutes to stabilize. The preferred procedure is to first let the gas pressure stabilize before filling the liquid nitrogen and running the measurement. This is to minimize unnecessary liquid nitrogen dissipation.

A measurement without gas was always done directly before or after a gas measurement. This serves as a zero measurement for the spectrum. One can subtract the spectrum without gas from the measured gas spectrum to improve the detectability of the gas emission spectrum. The preferred method is to execute a no gas measurement after the gas measurement, since the stabilization of the pressure towards high vacuum is considerably faster than from vacuum to a specific millibar pressure.

3.2.4. Setup Stability Measurement

Setup stability measurements are executed similarly to gas spectrum measurements, but with no gas supplied, and with the aim to characterize the stability of the system over increasing integration time. Changing certain components or operating conditions and comparing their stability results allowed for detailed analysis of the performance impact. See section 2.2.2 for more information on frequency stability.

4

Data Processing

This chapter will cover all data processing steps applied. This includes demodulation of the on-/off-source optically chopped signal, as well as fitting a brightness temperature to the read-out data of the DESHIMA detector and several stabilizing post-processing steps.

- The data of DESHIMA is saved as relative frequency shifts of the MKID resonant frequencies over time. Any measurement results with the optical chopper will have to be demodulated to find the amplitude of the chopper-modulated signal. The main demodulation method is covered in section 4.1. An alternative demodulation method used to cross-check the performance of the main demodulation method is covered in Appendix D.
- To obtain a brightness temperature from the relative frequency shifts, the rotating grid measurement is used to fit the calibration parameters for further conversion. This fitting process is extensively covered in section 4.2.
- To obtain a spectrum based on the brightness temperature, the data is integrated over time in section 4.3. Several additional data processing methods are applied onto the time data to improve the detectability of the gas emission spectrum.
- Section 4.4 finally covers the comparison of read-out gas emission data to simulations to find the absolute frequency offset error in the terahertz frequency sweep measurement.

All fitting described in this chapter is done using the LMFIT package [40] in python, see Appendix F.1 for more information.

4.1. On/Off Demodulation Using the Fourier Transform

The measurement results are saved as relative frequency shift values over time. A distinct wave-like profile is present due to the optical chopper The top of the chopping envelope represents the on-source signal, and the bottom represents the off-source signal. The signal of interest is contained in the difference between on- and off source signal. To demodulate this chopped data to the data of interest, one has to determine the amplitude of the wave-like profile. The demodulation method used is built on the Fourier Transform. See 4.1 for the basics of the demodulation method.

First, the relative frequency shift values over time are sliced into data segments to obtain a single amplitude value from. A balance has to be found in amplitude sampling resolution (shorter time slices) and amplitude accuracy (longer time slices). After extensive trials with different time slices, a time slice of half a second has found to be giving good results with a data sampling rate of 1200 Hz. This allows for 600 samples to extract a single amplitude sample.

Each data slice of half a second is stabilized by subtracting the minimum value of the respective time slice. This limits the impact of drifts between time slices, as all time slices are brought back to a zero bottom envelope. Note that any drifts within the time slice are not corrected and will affect the outcome of the Fourier Transform.

See Figure 4.2 for the demodulation of real data from a rotating grid measurement (run 887). For regular measurements, the demodulated sliced data are converted to brightness temperature data using fitting parameters obtained by the rotating grid measurement.

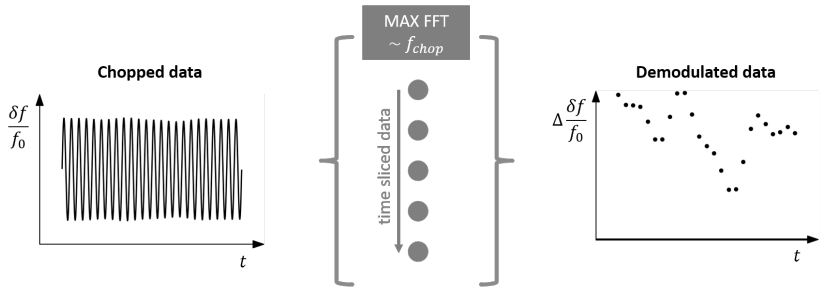

Figure 4.1: Schematic of the demodulation method based on the Fast Fourier Transform. **Left** The optical chopper modulates the signal reaching the detector by rapidly alternating the on-source and off-source path. **Middle** This time-signal is sliced into time segments of which the maximum Fourier transform value around the chopping frequency is taken. **Right** These values are used to find the difference in on- and off-source read-out over time. For DESHIMA the read-out data consists of frequency shifts relative to resonance frequency. The demodulated data is therefore a difference in relative frequency shift.

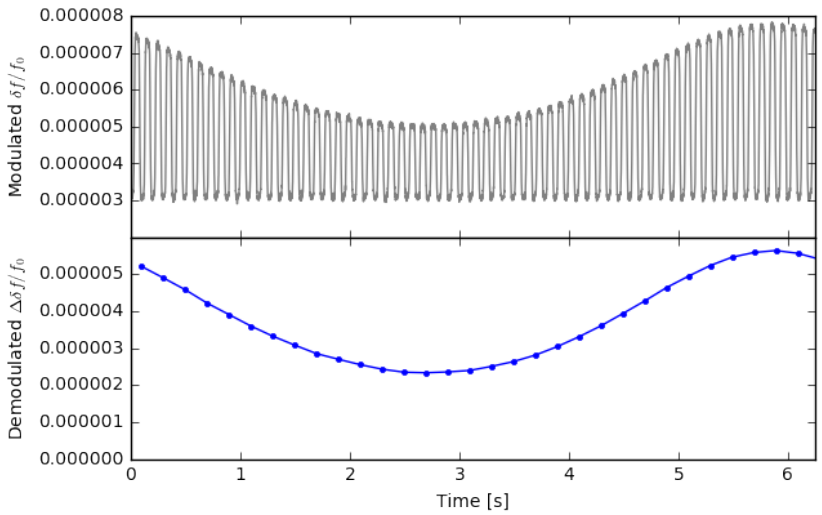

Figure 4.2: Demodulation method based on the Fast Fourier Transform applied on real data. **Top** Modulated data at 10 Hz. One can see a half rotation of the wire grid in the top envelope. **Bottom** Demodulated data. Each time slice of 0.5 seconds (600 samples at 1200 Hz sampling rate) results in a demodulated sample.

An alternative demodulation method based on the Hilbert transform was also developed to cross-verify the performance of this Fourier transform demodulation method. See Appendix D for an overview of how the Hilbert transform can be used and how the two demodulation methods compare.

4.2. Brightness Temperature Fitting to MKID Output

The rotating grid measurement (3.2.2) was done before a series of regular measurements to calibrate the frequency shift of the resonance frequency to a certain brightness temperature. This section will cover the fitting of the measurement data to an expected brightness temperature profile. From this fit, the frequency shift could be correlated to a brightness temperature. The main steps in this process are:

1. The relative frequency shift $\frac{\delta f}{f_0}(t)$ is measured by DESHIMA during the rotating grid measurement.
2. The measured data is demodulated for the optical chopping, resulting in a clean unchopped profile of the difference - further called 'delta' - in relative frequency shifts $\Delta\frac{\delta f}{f_0}(t)$ between the optical paths.
3. The demodulated data is sliced into time segments of approximately one period. Each segment fitted to an expected profile for the rotating grid measurement.
4. The fit parameters are used to calculate a similar brightness temperature profile per segment. These temperature segments are added together, resulting in a brightness temperature vs time $T_B(t)$ for the whole rotating grid measurement.
5. The brightness temperature $T_B(t)$ and the delta relative frequency $\Delta\frac{\delta f}{f_0}(t)$ for the same time data can be combined into a delta relative frequency vs brightness temperature $\Delta\frac{\delta f}{f_0}(T_B)$ dataset. This dataset is fitted to an expected model.
6. The fit parameters of this model can be used to correlate data from later measurements to a certain brightness temperature.

The actual measurement and the demodulation are covered extensively in other sections. Below, steps three to six will be discussed.

Step 3: Fitting the Rotating Grid Measurement to an Expected Profile

The demodulated data is segmented into slices of approximately half a rotating of the wire grid. This is done to account for instabilities in the angular velocity over time. The data of the rotating grid measurement is fitted to an expected periodic profile to determine the angular frequency over time. After extensive fitting trials, roughly one period has shown to be a good balance of sufficient data points for the fitting to work correctly. Below, the derivation of the expected profile and the fitting of the data to this profile is described. Figure 4.3 shows several segments of the rotating grid measurement (run 887) with the expected profile fitted. Typically, several segments would fail the fitting.

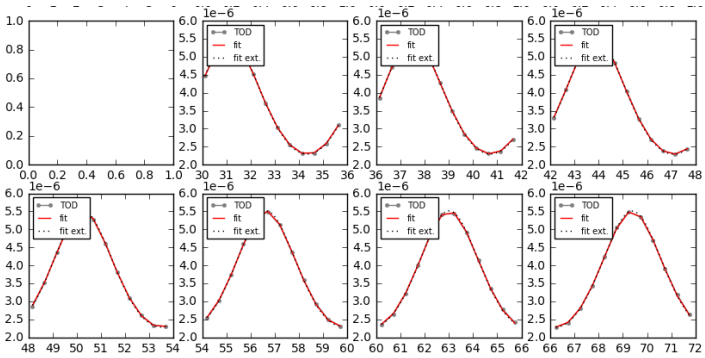

Figure 4.3: Several segments of 6.25 seconds of demodulated data from a rotating grid measurement (run 887). The expected profile is fitted to the data per segment. Some fits would fail. Here, the first segment shown failed and is left blank. The fit parameters were used to calculate a brightness temperature response.

Expected Intensity Profile Propagating through the Setup

The expected relative frequency shift profile is calculated as follows. Consider the simplified optical setup with only the rotatable/beam splitting and fixed wire grids, see also figure 4.4. Since two blackbody backgrounds are used, one can assume the light emitted to be incoherent. This allows the irradiance to be added

directly, simplifying the calculation. At the rotatable wire grid, room temperature radiation from the side is reflected at polarization parallel to the grid, and cold radiation along the main path is transmitted at polarization perpendicular to the grid. At the fixed wire grid, only polarization perpendicular to the orientation of the grid are transmitted. Consider now three sections: (A) the path before the beam splitting wire grid, (B) the path in between the two wire grids, and (C) the path after the wire grid and onto the detector, see again figure 4.4.

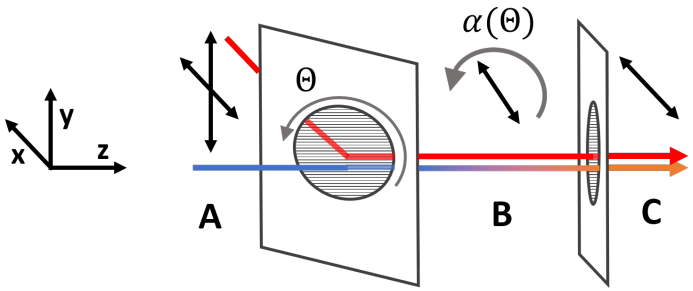

Figure 4.4: Schematic representation of the cold background and hot calibration background radiation paths through the two wire grids in the setup. The rotating wire grids in combination with the second stationary wire grid allows for control over the transmission and reflection of both paths. Section A covers the path before the beam splitting wire grid, where both radiation paths are uniform polarized. Section B covers the path in between the two wire grids, where the transmitted polarization is aligned with the rotating wire grid angle projected onto the propagation plane $\alpha(\theta)$. Section C covers the path after the wire grid and onto the detector, where the polarization is aligned with the second wire grid.

At section A, there are two optical paths, one with uniform polarized light at room temperature intensity, and one with uniform polarized light at liquid nitrogen boiling temperature intensity,

$$\text{Section A:} \quad I_{room}, \angle\forall \quad I_{LN2}, \angle\forall. \tag{4.1}$$

At section B, both optical paths from before the beam splitting wire grid are combined into one. For a beam of uniform polarized light, the transmitted or reflected intensity will be halved by the linear polarizer, assuming an ideal polarizer. In section B the combined intensity is

$$\text{Section B:} \quad \frac{1}{2} I_{room}, \angle(\theta + \frac{1}{2}\pi) \quad \frac{1}{2} I_{LN2}, \angle\theta. \tag{4.2}$$

where the angle θ is the circular orientation of the wire grid polarizer, defined on the half circle domain $[-\frac{\pi}{2}, \frac{\pi}{2})$ due to its symmetry. Polarization parallel to θ (perpendicular to the wires) will be transmitted, and polarization perpendicular to θ (parallel to the wires) will be reflected. However, these angles are in the plane of the wire grid. To correct these angles for the effective angles in the optical path, one applies a projection onto the optical path plane.

$$\theta' = \arctan\left(\frac{y'}{x'}\right) = \arctan\left(\frac{\sin\theta}{\cos\theta\cos\phi_{tilt}}\right) = \arctan\left(\frac{\tan\theta}{\cos\phi_{tilt}}\right), \tag{4.3}$$

where θ' is the effective polarization angle seen from the main optical path, and ϕ_{tilt} is the angle the rotating wire grid plane makes with respect to the main optical path (typically 45°). See figure 4.5 for a schematic drawing of these angles.

At section C, the combined optical path passes the final wire grid and reaches the detector. One can use Malus's Law to calculate the intensity after the second polarizer for linear polarized light as

$$I = I_0 \cos^2 \Delta\theta, \tag{4.4}$$

where $\Delta\theta$ is the relative angle between the incoming linear polarized light and the grid transmission orientation. I_0 is the intensity of the incoming linear polarized light. Effectively, this is the difference in angle between the two wire grids. For no relative angle, the setups result in full transmission for linear polarized light aligned perpendicular to the wires. For section C, one can write:

$$\text{Section C:} \quad I_C = \frac{1}{2} I_{room} \cos^2(\Delta\theta + \frac{1}{2}\pi) + \frac{1}{2} I_{LN2} \cos^2 \Delta\theta \tag{4.5}$$

$$= \frac{1}{2}\left[I_{LN2} + (I_{room} - I_{LN2}) \sin^2 \Delta\theta\right]. \tag{4.6}$$

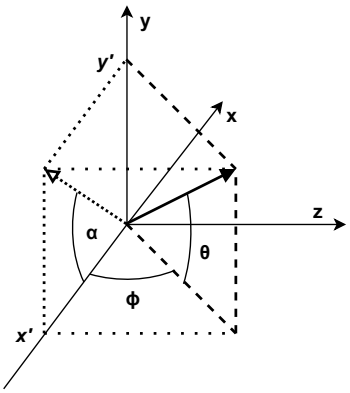

Figure 4.5: Schematic drawing of the xy-plane projection (dotted arrow) of the wire grid orientation (solid arrow) along the optical axis z. The wire grid is tilted with angle ϕ from its perpendicular position to the optical path. The wire grid transmission vector is orientated with angle θ from the horizontal xz-plane. The projection of the wire grid transmission vector has angle α with respect to the x-axis with coordinate (x', y') in the xy-plane.

The above formula gives the expected intensity profile reaching the detector for a relative angle of the two wire grids. Since the wire grid in front of the cryostat remains still, the relative angle $\Delta\theta$ will follow the rotation of the rotating wire grid directly.

Relative Frequency Shift Profile in Detector Output
The relative shift in resonance frequency is related to the square root of the power reaching the MKIDs (Eq. 2.21), which is directly related to the intensity of the incoming light and the brightness temperature:

$$\frac{f - f_0}{f_0} = \frac{\delta f}{f_0} \sim \sqrt{P} \sim \sqrt{T}. \tag{4.7}$$

The expected profile to be seen in the relative frequency shift output of DESHIMA is therefore similar to the square root of the expected intensity profile reaching DESHIMA:

$$\frac{\delta f}{f_0} \sim \sqrt{\frac{1}{2}\left[I_{LN2} + (I_{room} - I_{LN2})\sin^2\Delta\theta\right]}. \tag{4.8}$$

The Fitting Model for the Output of the Rotating Grid Measurement
Combining the expected fit profile of equation 4.8 and the projected angle of equation 4.3, the fitting model to determine the angular frequency is derived to be

$$\theta = \omega \cdot x + \phi_0 \tag{4.9}$$

$$\alpha = \arctan\left(\frac{\tan\theta}{\cos\phi_{tilt}}\right) \tag{4.10}$$

$$Const. = \left(y_{min} + y_{offset}\right)^2 \tag{4.11}$$

$$Ampl. = \left(y_{max} + y_{offset}\right)^2 - \left(y_{min} + y_{offset}\right)^2 \tag{4.12}$$

$$y = \sqrt{Ampl. \cdot \sin^2(\alpha) + Const.} - y_{offset} \tag{4.13}$$

where ω, ϕ_0, ϕ_{tilt}, y_{min}, y_{max} and y_{offset} are the resulting fit-parameters. These fit parameters are chosen for their ease of finding the optimum initial values. The input x and y data are the time and the *difference* in relative frequency shift in between optical paths, respectively. To avoid confusion this difference in relative frequency shift in between optical paths will be described as delta relative frequency shift and in equations as

$$\Delta\frac{\delta f}{f_0} = \frac{f_2 - f_0}{f_0} - \frac{f_1 - f_0}{f_0} \tag{4.14}$$

To compare this difference with the expected profile of equation 4.8 the y_{offset} parameter was added, effectively representing the relative frequency shift of the off-source optical path. Note that both $Ampl.$ and $Const.$ are highly correlated with y_{offset} in this fitting model.

Step 4: Assigning a Temperature profile to the Rotating Grid Measurement

The effective brightness temperature is related linear to the irradiance power. The brightness temperature can therefore be modelled similar to equation 4.6. However, the calculation is adjusted to account for spill-over. The bottom of the chopping envelope of the rotating grid measurement output represents the direct path to the LN2 background and is assumed to be at LN2 boiling temperature $T_{LN2} = 77K$. The top of the chopping envelope represents the gas cell path. See Figure 4.6. Since the minimum top envelope is higher than the bottom of the envelope, it would be incorrect to assume a full transmittance of the gas cell path to be at LN2 temperature. To calculate a more accurate setup temperature T_{setup} corresponding to the gas cell path, one can use the fitting parameters as

$$T_{setup} = \left(\frac{y_{min}}{y_{max}} \left(\sqrt{T_{room}} - \sqrt{T_{LN2}} \right) + \sqrt{T_{LN2}} \right)^2 . \tag{4.15}$$

Using the setup temperature one can find the profile of the effective brightness temperature over rotating angle as

$$T = T_{setup} + \left(T_{room} - T_{setup} \right) \sin^2 \Delta\theta. \tag{4.16}$$

Step 5: Calibrating Delta Relative Frequency shift to Temperature

One now has a delta relative frequency shift - step 3 - and effective brightness temperature - step 4 - for every time data sample of the rotating grid measurement. These can now be plotted against each other and fitted to an expected model to obtain the fitting parameters describing a brightness temperature versus relative frequency shift. See figure 4.6 for an illustration of this profile.

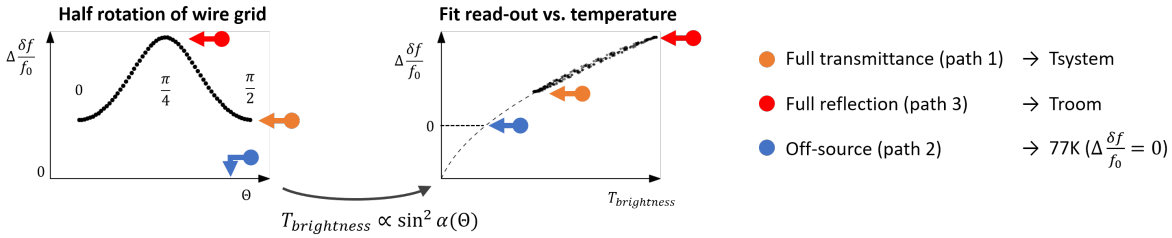

Figure 4.6: The demodulated response of the rotating grid measurement can be mapped to a calculated brightness temperature based on the wire grid rotation using the expected squared sinusoidal profile. The mapped data is fitted to an expected square root profile to obtain the calibration parameters used to convert the data from later measurements to a brightness temperature.

Since a square root relationship is expected from theory, see section 2.1, the fitting model is derived to be

$$\Delta \frac{\delta f}{f_0} = p_0 \sqrt{T + T_0} + p_1 \tag{4.17}$$

where $\Delta \frac{\delta f}{f_0}$ and T are the previously obtained delta relative frequency shift and temperature per data sample. The fitting parameters p_0, p_1 and, T_0 are saved and can be used as calibration parameters to relate a brightness temperature to the data of subsequent measurements. See Figure 4.7 for real frequency vs. temperature data with the fitted profile.

Step 6: Calculating the Brightness Temperature of Data

For subsequent measurements after the rotating grid calibration measurement, one can convert the delta relative frequency shift to a brightness temperature using the fit parameters. It is important to note that the delta relative frequency shift corresponds to a temperature shift from the liquid nitrogen background temperature. One can adapt the fit parameters to work with any background. If one would have a different background at temperature T_{base}, one could compare the delta relative frequency shifts of the on-source signal and the 'base' signal using the previously found fit parameters as

$$\Delta \frac{\delta f}{f_0}\bigg|_T - \Delta \frac{\delta f}{f_0}\bigg|_{T_{base}} = \Delta' \frac{\delta f}{f_0} = p_0 \left(\sqrt{T - T_0} - \sqrt{T_{base} - T_0} \right). \tag{4.18}$$

This can be rewritten to

$$T = \left(\frac{\Delta' \frac{\delta f}{f_0}}{p_0} + \sqrt{T_{base} + T_0} \right)^2 - T_0, \tag{4.19}$$

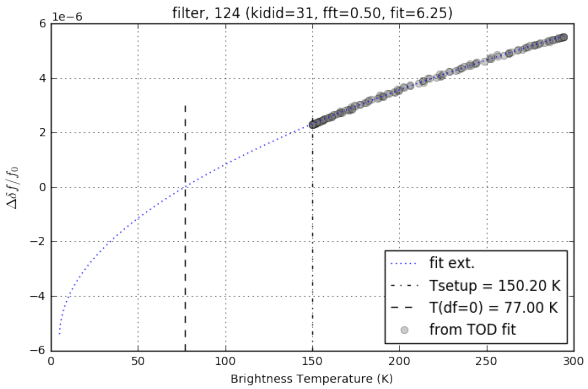

Figure 4.7: Relative frequency shift plotted vs. brightness temperature. The data is fitted to an expected model to obtain the fitting parameters describing a brightness temperature versus relative frequency shift. The data are from a rotating wire grid measurement, run 887. To obtain this profile, a time slice of 0.5 seconds was used for the FFT demodulation and 6.25 seconds for the rotating grid profile fit.

where one now has a relationship to find a brightness temperature using an arbitrary base temperature T_{base} and the relative frequency shift difference $\Delta' \frac{\delta f}{f_0}$ between the on-source path and the background path at temperature T_{base}.

4.3. Processing MKID Time Data to a Best Estimate of the Spectrum

The spectrum of the gas emission is generated by averaging the brightness temperature over time for each MKID data. Frequency stability analysis can show what averaging time will reach the lowest variance by calculating the Allan deviation profile, see section 2.2.3. See Figure 5.13 in the Results & Discussion chapter for a detected spectrum of 30 mbar nitrous oxide.

Extensive post-processing of the MKID time data has been done to improve the detectability of the gas spectrum. In general, a good post-processing procedure has been found to correct the data output of each MKID for its linear drift of the full measurement time. The linear drift correction fits a simple linear profile to the data over time using a least squares regression. It adjusts the data to its baseline as.

$$y'_{i-MKID} = y_{i-MKID} - \alpha_{i-MKID} \cdot x_{i-MKID} \tag{4.20}$$

where the corrected data y' is obtained from the uncorrected data y by subtracting the fitted linear slope α times the time data x.

The overall mean correction is then applied by first normalizing each MKID output profile for its mean value and standard deviation. The overall mean of the normalized profiles for a single measurement run is obtained as

$$\hat{y}_{run} = \frac{1}{n_{MKID}} \sum_{i-MKID} \frac{y'_{i-MKID} - \mu_{y'_{i-MKID}}}{\sigma_{y'_{i-MKID}}} \tag{4.21}$$

for n_{MKID} the number of filterbank MKID output profiles on which the common profile is taken, $\mu_{y_{i-MKID}}$ denotes the arithmetic mean of the MKID data and $\sigma_{y_{i-MKID}}$ its standard deviation value. Each individual MKID output profile is corrected for this overall mean as

$$y"_{i-MKID} = y'_{i-MKID} - \left(\hat{y}_{run} \cdot \sigma_{y'_{i-MKID}} + \mu_{y'_{i-MKID}}\right). \tag{4.22}$$

This scaling for the standard deviation is necessary to determine the common profile affecting the results while retaining the scale information of each MKID profile. Note that this overall common profile correction is done after the linear drift correction. Figure 4.8 shows how these corrections affect real data. The time data of run 889 for MKID 31 showed a distinct stability improvement with the common mean removed. The effect of the linear drift removal was less for this run.

More advanced algorithms (e.g., including machine learning models) to find the common modes over all MKID outputs are believed to be able to further improve the detectability, but have not yet shown a distinct improvement.

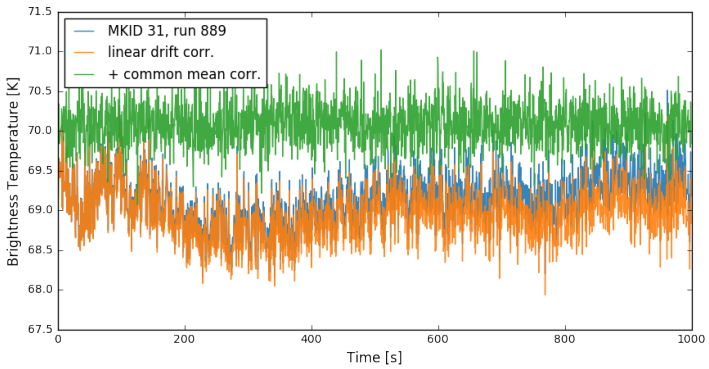

Figure 4.8: The effect of the post-processing on real data (MKID 31 of run 889). For this dataset, the removal of the common profile is well visible. The linear drift removal had less effect.

4.4. Simulation Fitting to Obtain the Frequency Calibration Error

To obtain the absolute frequency shift of the spectrum detected by the DESHIMA instrument, the detected spectrum is compared to simulations. For several shifts, the data for the THz frequency sweep measurement are altered and the expected read-out profile is simulated. See subsection B.3 for an in depth overview of the simulation. To determine the absolute frequency shift, the simulated profiles for the several shifts are fitted to the detected spectrum by finding the lowest residual by altering amplification and offset. The reduced chi square of each best fit per frequency shifted simulation are compared to determine the best overall fit. The absolute frequency shift corresponding to the best overall fit is believed to be the absolute error in the THz frequency sweep measurement.

5

Results & Discussion

The process to improve the gas cell setup to evaluate DESHIMA's performance has been a continuous loop of analysing the measurement data, finding the performance limiting aspects and improving on these. The main result of this research would be the most stable iteration of the gas cell setup in combination with the latest post-processing procedure. The most stable iteration would include the single liquid nitrogen target, a gas cell with anti-reflective coating on its windows and a cryostat system that allows for optimum optical coupling. The post-processing procedure would include the linear drift correction and reduction of the common profile. The most stable iteration of the setup and post-processing procedure have been covered extensively in chapter 4 Data Processing. This chapter aims to quantify the performance of the latest iteration of the gas cell setup and the improvements made during the iterative research.

- Section 5.1 covers the impact of the post-processing procedures on the stability of the output results.
- Section 5.2 covers the noise stability of the setup over time, with a focus on changes made over different iterations, such as the background and window type.
- Section 5.3 covers the spectrum detectability of the gas cell setup with DESHIMA 1.0 as detector. Measured and modelled spectra of nitrous oxide and methanol are reviewed and compared.

5.1. Noise Stability Improvements by Post-Processing

Several post-processing steps have been developed to further stabilize the read-out data of a measurement. This section and the next one cover the stability of the setup over time. This stability analysis will mainly be done based on total deviation (TOTDEV). TOTDEV is a useful metric to investigate the data stability over increasing averaging intervals. See as well section 2.2.3 for more information. In this section, the optimum averaging time will be used as a metric for the setup stability. This optimum averaging time is found in the TOTDEV vs. averaging interval plot as the minimum deviation value for averaging times up to half of the total measurement time. The upper limit of half the total measurement time is used because TOTDEV profiles can generally only be trusted up to this point. Note, the TOTDEV values are not adjusted for low bias compared to Allan deviation (ADEV). This bias is present for certain noises at long averaging times, see section 2.2.3. Here, the bias is of no concern, as the bias does not influence the optimum averaging time or the overall slope of the TOTDEV profile.

In this section, the improvements in TOTDEV behaviour by post-processing are analysed using measurements runs 830 and 865. These runs have been chosen since they have shown good overall stability compared to other runs. The digital demodulation of the chopped signal is technically part of the post-processing, but is not considered here. A stability analysis comparing the main demodulation algorithm with an alternative algorithm can be found in Appendix D The demodulation algorithm was not found to induce unwanted instabilities.

5.1.1. Linear Drift Correction of Single MKID Time Data

Measurements in the Hydra setup have been prone to linear drifts in the read-out data. These drifts were different per MKID in both size and direction, but did show similarities over different measurement runs. The drifts could not be allocated to an actual temperature drift in the background, the overall setup or the

environment. A temperature drift is expected to induce a drift similar for all MKIDs and to differ per run. It was found that these drifts were strongly present for runs where the snout was used for the mounting of the detector in the Hydra cryostat. The removal of the snout reduced these drifts. See Figure 5.1 for the time data of MKID 30. The figure shows the distinct linear drift, especially visible for run 830 with the snout, and reduced for run 865 without the snout. See Figure 5.2 for the linear drift for each MKID over the spectrum for several runs. Note how the drift over the spectrum is similar for the different runs, even though these runs were on separate days with different setups. The assumed explanation is that the snout caused the detector to vibrate inside the cryostat. These resonating vibrations could be influencing each MKID in a reproducible way, resulting in these typical drifts.

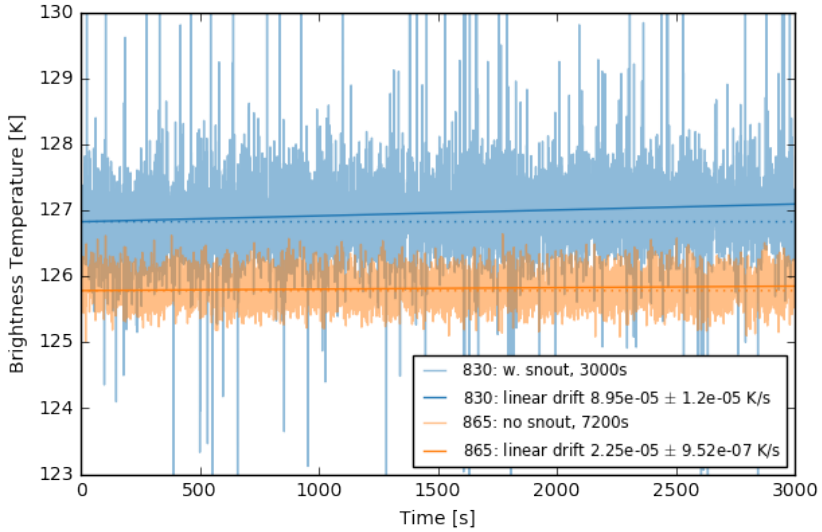

Figure 5.1: Brightness temperature data over time for MKID 30 of relatively stable runs. Both runs show a linear drift in the data over time, indicated by a straight line. These drifts were enhanced when the snout was used for mounting the detector in the Hydra cryostat. The vibrations of the snout are likely to increase the linear drifts in the data. Note the high amount of outliers in run 830. These are due to the vibrating snout by touching the cryostat inner casing, which disturbs the sensitive read-out.

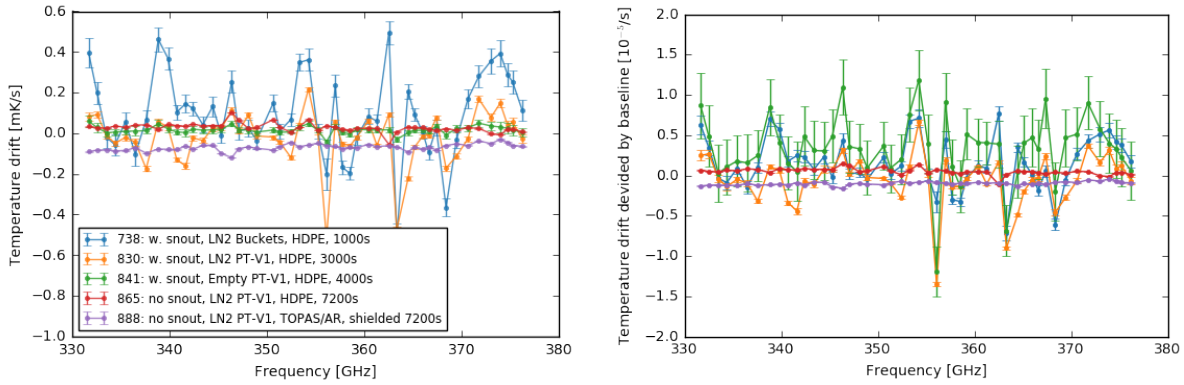

(a) (b)

Figure 5.2: Linear drift versus center frequency of different measurement runs. Note how the drift versus frequency profile is similar for runs 738, 830 and 841, even though these runs were done with different setups on different days. The removal of the snout removed the typical drift profile. **(a)** The linear drift is taken over the full time data of the brightness temperature per MKID and plotted versus its corresponding THz filter frequency. **(b)** The linear drifts divided by the respective baseline (mean of the MKID time data). Due to the square root dependency in the temperature calibration, linear drifts of the same absolute size have a reduced impact at higher temperatures. The plot illustrates that the drift profile versus frequency is present for all background temperatures, especially for the run with room temperature background (run 841).

Removing the drift during post-processing from measurements with the snout has greatly improved the stability in its TOTDEV behaviour. Even for measurements without the snout, it has still been found good

practice to reduce any linear drifts. The cause of linear drifts is not believed to be from the source gas, as long as the pressure is not drifting in a similar way. A linear drift in the read-out could either be from a malfunction in the detector instrument (like the vibrating snout) or by temperature drifts of the setup and its environment. Both are important to be aware of and interesting for further analysing, but offer limited information on detecting the gas emission spectrum. Furthermore, removing the linear drift allows for better visualization of other instabilities in the TOTDEV behaviour. See Figure 5.3 for the total deviations profiles and Table 5.1 for the overall optimum averaging time means for both runs with and without their linear drifts removed. Note that the sudden drop at the end of the TOTDEV behaviour is artificial. The removal of linear drift also reduces the variance of the signal when the averaging interval approaches the total measurement on which the linear drift is calculated.

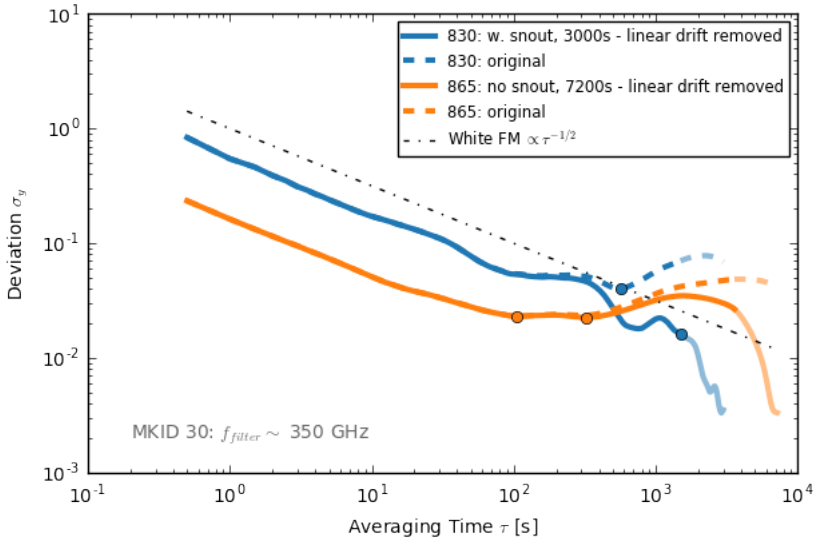

Figure 5.3: Total deviation profiles for MKID 30 of relatively stable runs with and without linear drift removal. Run 830 reacts well to the drift removal compared to run 865. This is in agreement with the read-out profile over time, where run 830 showed a larger drift.

ID: Type	**Mean Optimum τ (s)**	
	Original	**Drift removed**
830: w. snout, 3000s	677 ± 420	1498 ± 2
865: no snout, 7200s	259 ± 496	1531 ± 1650

Table 5.1: Mean optimum averaging time over all filterbank coupled MKIDs with and without linear drift removal. The average optima show a large increase when the linear drift is removed. This is especially notable for run 830, where the average has reached the maximum value within the allowed range of trust at half the total measurement time.

5.1.2. Common Mean Correction of all Simultaneous MKID Time Data

The brightness temperature over time per MKID were found to have common profiles during a run. The common profile was found to be stronger for runs with bad alignment or with the snout removed. A possible explanation is that both misalignment and removal of the snout increase the risk of spill over. This would indicate that the overall drift finds its cause in environmental radiation. Environmental radiation can typically be considered as blackbody radiation and stable over the full frequency range of DESHIMA. That could explain the overall profile seen in all MKIDs. Another explanation of these common profiles could be found inside the setup or cryostat system. Any moving component could cause this drift over time. Further research is needed to find the exact cause. See Figures 5.4a and 5.4b for several brightness temperature datasets over time for different MKIDs of run 865 and 890.

Since the overall profile is present in all read-out data of the MKIDs, the profile could be discerned and removed without altering the differences in between MKIDs. This is important as these differences contain the information on the emission spectrum profile. Figure 5.5 and Table 5.2 show the total deviation behaviour when applying the common profile removal algorithm. Notice how the removal of the common profile im-

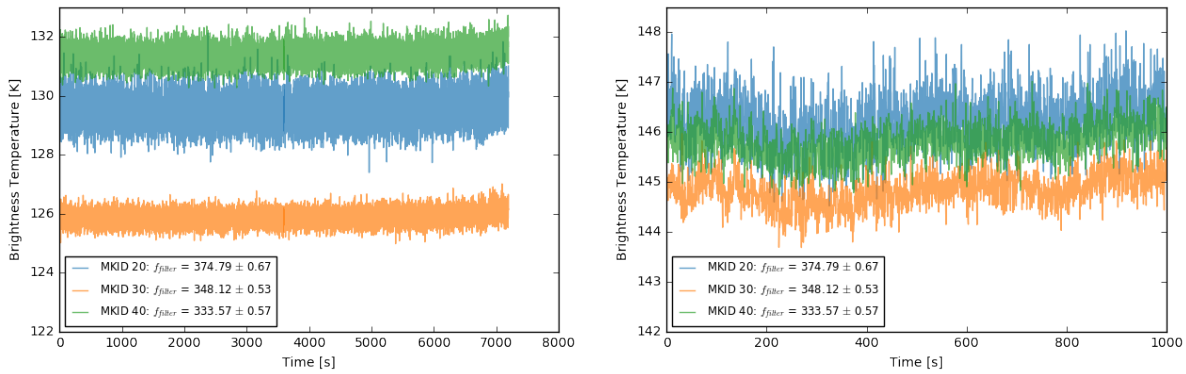

(a) (b)

Figure 5.4: Brightness temperature profiles over time for several MKIDs of run 865 and 890. All profiles for different MKIDs of a single measurement run show a similar common profile. **(a)** Brightness temperature data of three MKIDs from run 865, which had the snout removed. Note the upward curve after 6000s. **(b)** Brightness temperature data of three MKIDs from run 890, which had the snout removed and showed improper alignment. The common profile is clearly visible. The improper alignment can be seen in the higher baseline temperatures compared to run 865.

proves the stability of run 865 as nonlinear environmental drifts that are affecting all MKIDs are successfully removed. It is interesting how run 830, which already had a stable profile after the linear drift removal, still shows an overall TOTDEV reduction. This is likely due to a reduced impact of outliers. The vibrating snout hitting the cryostat casing caused strong outliers in the read-out of every MKID, see for example Figure 5.1 of the previous subsection. These are included in the common profile and subsequently removed. See section 4.3 for more information on how this algorithm works.

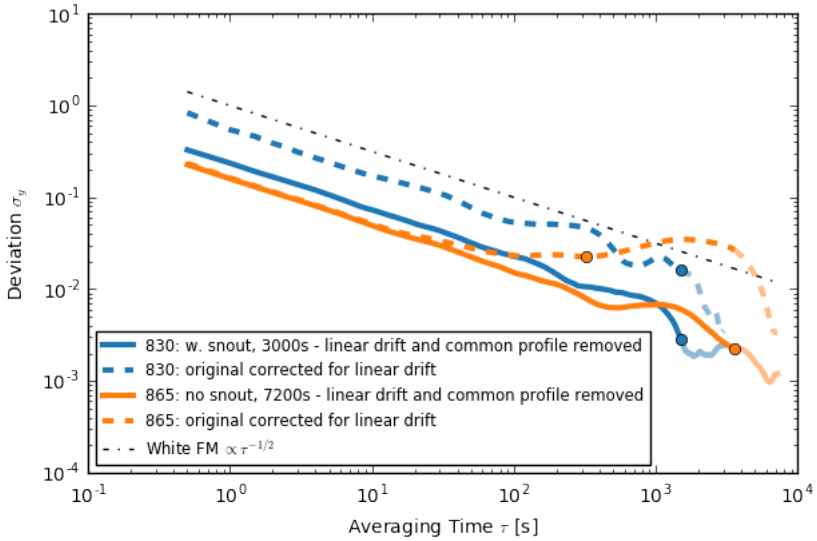

Figure 5.5: Total deviation profiles for MKID 30 of relatively stable runs with and without common profile removal. Note that the stability plot of run 865 improves, while run 830 remains similar. This is in line with the read-out over time, where run 865 showed a strong common profile present in all MKID's read-out data, while run 830 showed no distinct common profile.

ID: Type	Mean Optimum τ (s)		
	Original	Drift removed	+ Common profile removed
830: w. snout, 3000s	677 ± 420	1498 ± 2	1479 ± 61
865: no snout, 7200s	259 ± 496	1531 ± 1650	2417 ± 1580

Table 5.2: Mean optimum averaging time over all filterbank coupled MKIDs per measurement run, with and without common profile removed. The average optimum for run 865 shows a large increase when the common profile is removed. This is in line with expectations, since run 865 had a distinct common profile present in all MKID's read-out over time. Run 830 was already at its maximum value after the linear drift removal. Note how run 830 has its mean reduced and deviation increased, but still falls on the edge of maximum allowed value within the range of trust.

5.2. Noise Stability Impact of Key Setup Components

This section covers the impact of several key components on the stability of the setup over time. The type of background, chopping frequency and effect of gas circulation are investigated. Inside the cryostat, the impact of the snout for mounting the detector and the effect of magnetic shielding are reviewed.

5.2.1. Background Stability

Zhang's research showed the previous gas cell setup design had a noise stability of up to about 20 seconds, after which some MKIDs would have reached their optimum averaging time. Extensive testing has shown the background to be of great importance for the stability over time. Figure 5.6 shows the TOTDEV profiles of a measurement with two separate liquid nitrogen buckets as backgrounds compared to several measurements with a single liquid nitrogen PT-V1 background. The TOTDEV profiles are taken for MKID 31 of DESHIMA 1.0. The filter center frequency coupled to MKID 31 has been measured at ~350 GHz. This is in the middle of the frequency range of DESHIMA 1.0. Figure 5.6 shows that for MKID 31 the setup was stable up to ~30 seconds for the two separate buckets. When using the PT-V1 target as a single background, the setup was stable for the entire range of confidence of the respective measurement. Note, Figure 5.6 also shows a measurement with an empty PT-V1 target, which is essentially a room temperature blackbody as background. The stability at room temperature has not noticeably changed compared to liquid nitrogen (77K) temperatures. The mean and standard deviation of all optimum averaging times for all MKIDs coupled to the filterbank are given in Table 5.3. The overall means show a clear stability improvement when using a single PT-V1 target as background.

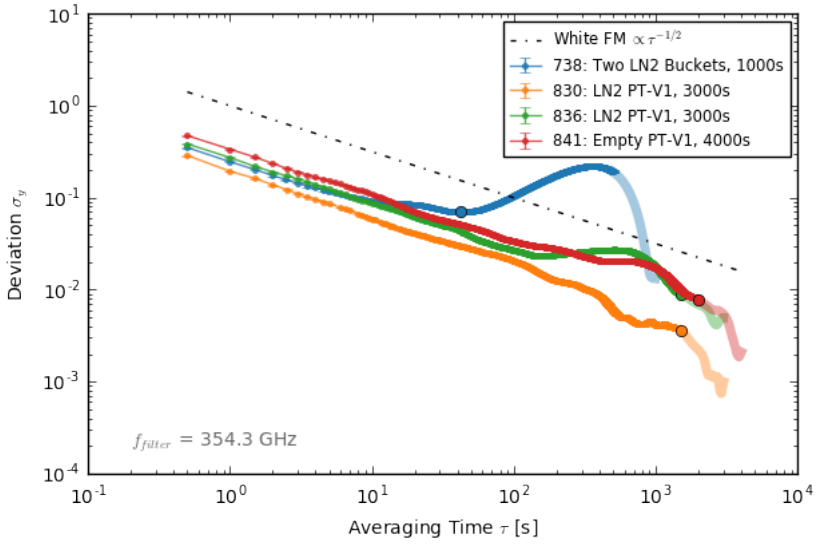

Figure 5.6: TOTDEV profiles of several empty gas cell measurements with different backgrounds. All measurements with the PT-V1 target as single background for both main optical paths, either filled with liquid nitrogen (77K) or empty at room temperature, showed a TOTDEV profile following the white noise integration profile for its respective range of trust. This indicated no systematic errors occurring over time. The double liquid nitrogen bucket background showed an optimum averaging time at only ~30 seconds, after which non-linear drifts in the measurement output are affecting the data. The dash-dotted line represents the TOTDEV profile of integrating frequency modulated white Gaussian noise, which follows an inverse square root dependency.

ID: Type	Mean Optimum τ (s)
738: Two LN2 Buckets, 1000s	87 ± 109
830: LN2 PT-V1, 3000s	1479 ± 61
836: LN2 PT-V1, 3000s	1475 ± 156
841: Empty PT-V1, 4000s	1947 ± 205

Table 5.3: Mean optimum averaging time over all filterbank coupled MKIDs. The error represents the standard deviation. The overall means are in agreement with the results of MKID 31 in Figure 5.6. The single PT-V1 background runs show a stability improvement compared to the double bucket background. Note that the optima are taken on the first half of the measurement time. An optimum averaging time of half the total measurement time indicates no limiting instabilities in the TOTDEV range of trust. This is the case here for all PT-V1 runs.

5.2.2. Impact of Snout and Shielding

To counter strong drifts due to vibrations of the snout and the impact of magnetic interference, recent measurements had the snout removed and magnetic shielding applied in the Hydra cryostat. Figure 5.7 shows the TOTDEV profiles for KID 30 over several runs and Table 5.4 the overall means. This time MKID 31 did not show typical behaviour for all MKIDs, as such MKID 30 is shown which also has a center frequency ~ 350 GHz. The results are inconclusive to determine whether the removal of the snout improved the stability. It is believed that the vibrating snout caused an instability in the setup, but its removal worsened the optical coupling and increased the detection of spillover radiation. From the figure and table, it would seem that the magnetic shielding worsened the stability. However, this could be misalignment of the setup. It is believed that the typical 'bulge' one can see at long averaging times for the shielded TOTDEV profile (run 888) is due to environmental drifts. Misalignment of the setup increases the impact of the environmental drifts since more spill over radiation will be detected. In Figure 5.21 of the next section, one can see the increased baseline for run 888 compared to the unshielded runs 830 and 856, which affirms the misalignment of the shielded run 888.

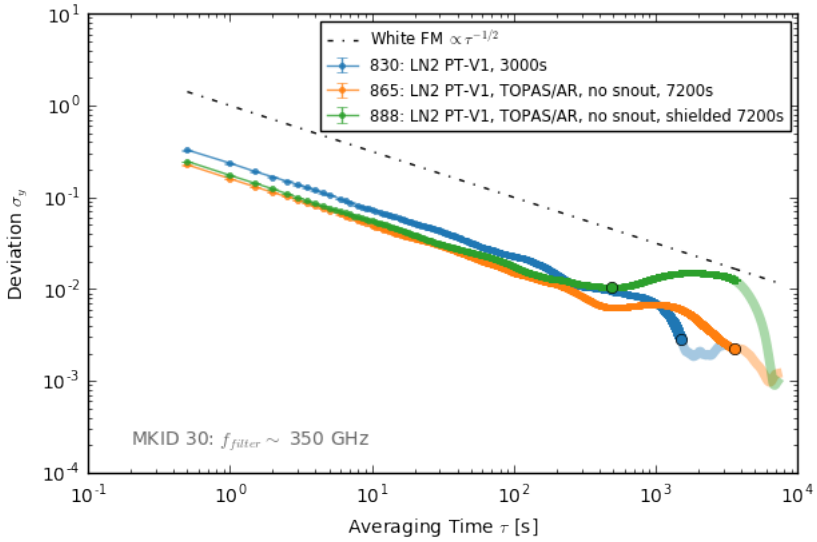

Figure 5.7: Total deviation profiles of MKID 30 of several empty gas cell measurements to compare the impact on stability when removing the snout and applying magnetic shielding. From this TOTDEV profile one can not conclude whether the removal of the snout improved the stability, since no measurements for 7200s with snout were done. The worsened performance with shielding is believed to be due to improper alignment, not due to the shielding itself. However, further testing is necessary to determine the exact shielding performance.

One has to note that the standard deviation of the mean optimum averaging time is large for runs with the snout removed. The post-processing removed the common profile, which was assumed to be from environmental effects due to the worsened optical coupling without the snout. Although the common profile improved the stability, this seems to be insufficient for some MKIDs. The 'bulge' as described earlier and as seen for run 888 in Figure 5.7 is still present for some runs, limiting their optimum averaging time. Figure 5.8 shows the optima versus the MKIDs (ordered for their THz filter frequency). Notice how the 'bad performing MKIDs are not consistent over the two different runs. Extensive analysis has not found a correlation between the bad performing MKIDs over the performed runs. What specific conditions determine whether the MKID

ID: Type	Mean Optimum τ (s)
830: LN2 PT-V1, HDPE, snout, 3000s	1479 ± 61
865: LN2 PT-V1, TOPAS/AR, no snout, 7200s	2417 ± 1580
888: LN2 PT-V1, TOPAS/AR, no snout, shielded 7200s	1161 ± 1418

Table 5.4: Mean optimum averaging time over all filterbank coupled MKIDs. The error represents the standard deviation. The measurement with magnetic shielding showed worsened results. However, this could be due to misalignment. Additional measurement are needed to determine the exact impact of the magnetic shielding.

is facing a limiting bulge in its TOTDEV behaviour remains a question for further research.

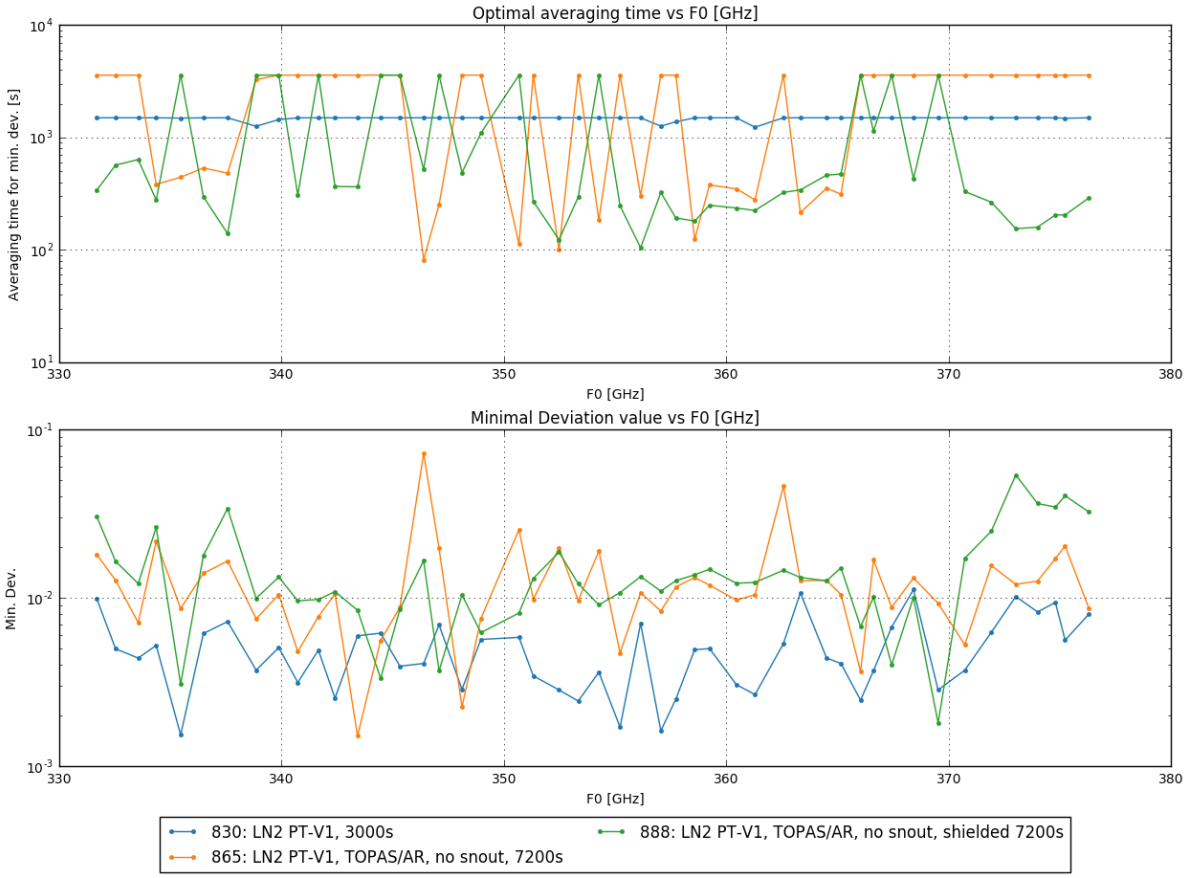

Figure 5.8: **Top**: Optimum averaging time per MKID, ordered by center frequency. For the runs without the snout, some MKIDs show bad performance. No correlation between the bad performing MKIDs was found over several runs. **Bottom**: The minimum TOTDEV value corresponding to the optimum averaging time given in the top figure.

5.2.3. Impact of Circulating Gas

The TOTDEV profiles of runs with gas inside the gas cell were compared with empty gas cell runs. Figure 5.9 and Table 5.5 show the TOTDEV behaviour of several runs used for the emission spectra of Figure 5.13 in the next section. From these TOTDEV profiles, it seems that circulating gas through the gas cell did not affect the stability over time. However, these TOTDEV profiles are only to be trusted up to 500 seconds, due to their total measurement length of 1000 seconds. To quantify the effect of gas circulation on the measurement stability for longer times, additional testing is required. The stability of the pressure was also analysed. Figure 5.10 shows the TOTDEV of the gas pressure recorded during run 889 (0.5 mbar nitrous oxide). From the figure, an optimum stability at a low ~30 seconds is found. Note how this instability in gas pressure was not seen in the signal as measured at the detector.

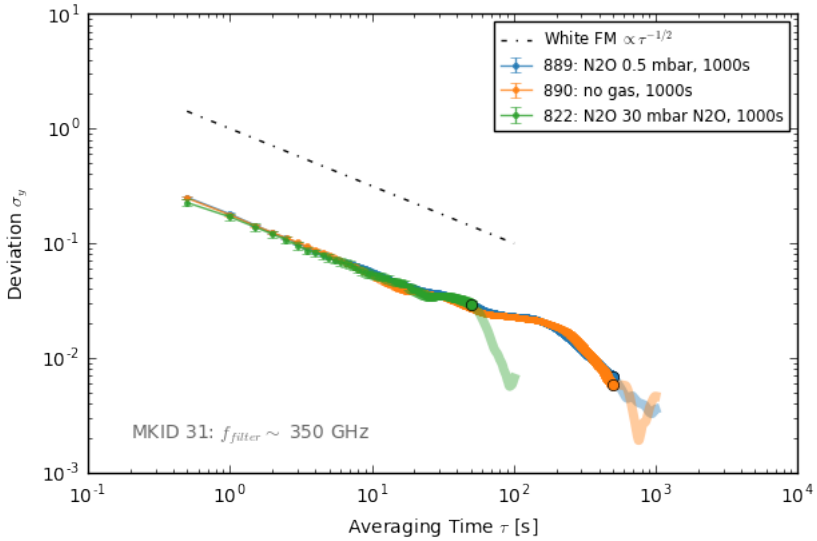

Figure 5.9: TOTDEV profiles of MKID 31 of several nitrous oxide gas measurements to compare the impact on stability when circulating gas through the setup. From these TOTDEV profiles, circulating gas did not seem to affect the stability over time.

ID: Type	**Mean Optimum τ (s)**
822: N2O 30 mbar N2O, 100s	50 ± 2
889: N2O 0.5 mbar, 1000s	436 ± 149
890: no gas, 1000s	494 ± 22

Table 5.5: Mean optimum averaging time over all filterbank coupled MKIDs per measurement run. The circulating of gas did not seem to strongly affect the stability for these runs, but the results remain inconclusive considering the large uncertainty. To quantify the effect of gas circulation on the measurement stability for longer times, additional testing is required

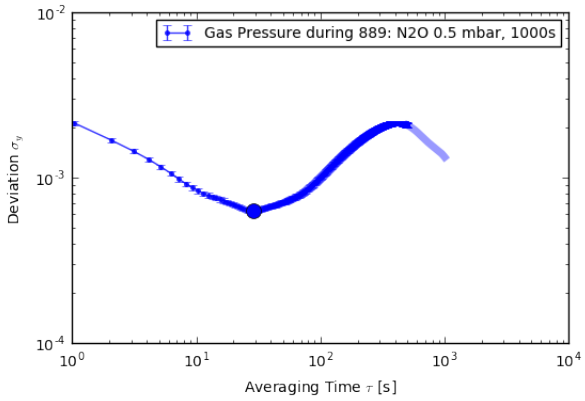

Figure 5.10: TOTDEV of the gas pressure recorded during run 889. The gas pressure has an optimum stability for ~30 seconds. This does not seem to affect the stability of the gas cell results, since no limitations are seen at similar interval lengths for the setup stability analysis.

5.2.4. Impact of Chopping Frequency

The optical chopper forms an important component in the setup, as it removes any noise and errors in between the on- and off-source paths at frequencies lower than the chopping frequency. Unless otherwise specified, all measurements were chopped at 10 Hz by rotating the double-winged chopper disc at 5 Hz. To investigate the effect of a higher chopping frequency a test was done with 20 Hz, see Figure 5.11 and Table 5.6 for the TOTDEV behaviour. From the TOTDEV behaviour, the increase in chopping frequency did not seem to improve the stability over time. One might even argue that the stability has worsened for a higher chopping frequency. Although this might seem counterintuitive, a higher chopping frequency could cause more vibrations in the setup, leading to a slight change in the optical alignment. The measurement with 20 Hz at least showed that it was not beneficial to increase the chopping speed with the current setup.

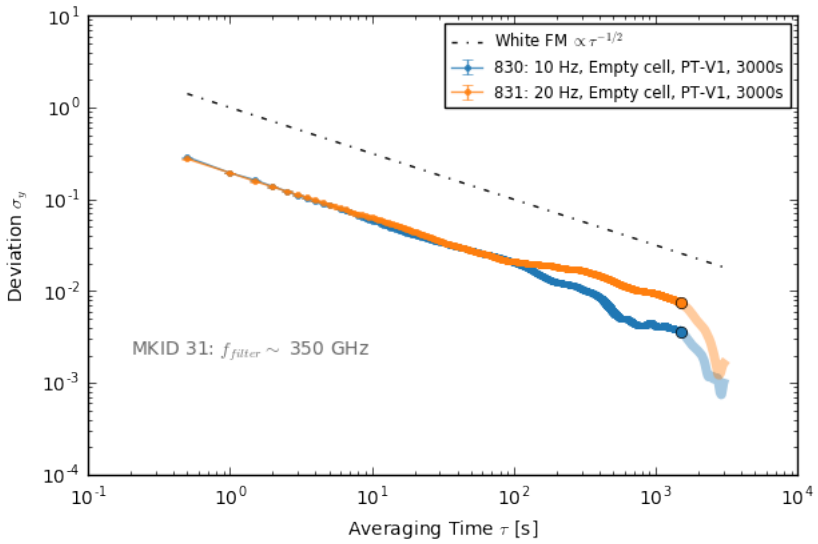

Figure 5.11: TOTDEV profiles of MKID 31 of empty gas cell measurements with either 10Hz or 20Hz chopping. The TOTDEV profiles seem to be similar, with the increased chopper frequency slightly diverging from the ideal white noise profile.

ID: Type	**Mean Optimum τ (s)**
830: 10 Hz, Empty cell, PT-V1, 3000s	1479 ± 61
831: 20 Hz, Empty cell, PT-V1, 3000s	1405 ± 276

Table 5.6: Mean optimum averaging time over all filterbank coupled MKIDs. The increase in optical chopping frequency seemed to have slightly worsened the mean optimum averaging time. However, it is hard to say without additional testing whether this is purely due to the chopping frequency or if a slight change in alignment occurred in between the measurements.

5.3. Low Pressure Detectability and Emission Spectrum Analysis

An ideal version of the gas cell setup would have no impact on the radiation of the gas of interest, resulting in a clean emission profile to be detected. The reality is that the gas cell setup will contaminate the radiation of the gas. To optimize the detectability of the gas emission spectrum, it is important to minimize the impact of the gas cell setup onto the spectrum. One can measure the spectrum without a gas supplied and subtract this 'zero'-measurement from the spectrum obtained with gas supplied. However, this only removes additive errors. Since other errors might influence the spectrum, it is desired to optimize the spectrum to be as clean and flat as possible when no gas is supplied. This section will cover the spectrum results that have been achieved with the setup. First, the lowest detectable pressures are reviewed and compared to simulations. After that, the impact of the windows and magnetic interference on the standing spectrum of the setup is discussed. An analysis of the impact of the rotating wire grid polarizer is covered in Appendix E.

Total Deviation as Error Bars

The error bars in the spectrum results discussed in this section represent the total deviation values at half the total measurement time. The use of total deviation as error bars is motivated by the non-white noises present in typical measurements with the gas cell setup, as analysed in the previous sections. Conventional error bars using the standard deviation do not account for non-white noises. See Figure 5.12 for a comparison of standard deviation, standard error, and total deviation for a typical measurement used in this section.

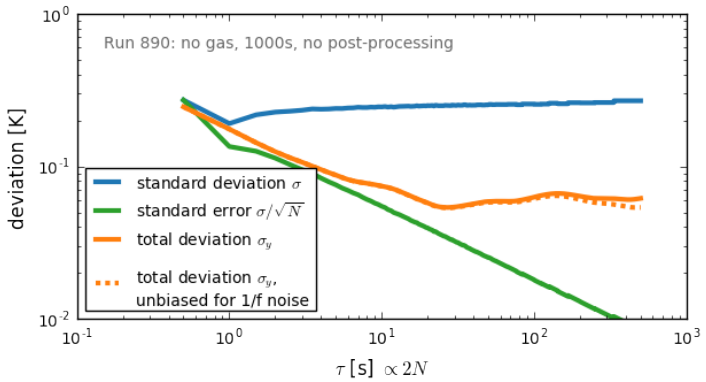

Figure 5.12: Comparison of different error bar implementations for increasing averaging times up to half the total measurement time. Here, run 890 is shown, a 1000s empty gas cell run with no post-processing. A flicker (1/f) noise due to spill-over is limiting the stability. The conventional methods using standard deviation or standard error do not properly account for non-white noises. Total deviation does allow for inclusion of non-white noises, and the presence of flicker noise is seen in its profile. Note, total deviation has a noise-specific low bias to Allan deviation, as is shown here for flicker noise.

The use of the total deviation value at half the total measurement time is motivated by the range of confidence of total deviation calculations. For averaging times above half the total measurement time, the total deviation value is not to be trusted. To reconcile the brightness temperature estimates with this half-measurement-time error bar, only one half of the data is used to obtain an estimate of the average brightness temperature over time. When a gas measurement is compared to a zero-measurement, the subsequent halves of the gas and zero-measurement are used. For example, when a gas measurement is done after a zero-measurement, the first half of the gas measurement and second half of the zero-measurement are used. By averaging only half the record length, one does not use all information available to obtain the best estimate of the mean. However, in this way, the error bars are accurate for the mean estimates shown.

Note, the total deviation values are not corrected for the low bias of total deviation compared to Allan deviation. This bias is dependent on the noise type, and would require an additional noise identification step. For white noise, no bias is present. For flicker and random walk noise, respectively, the error is biased low for 6~21% compared to the Allan deviation value. See section 2.2.3 for more information.

5.3.1. Emission Line Detectability of Nitrous Oxide and Methanol

Both nitrous oxide (N_2O) and methanol (CH_3OH) were used with the gas cell setup. Nitrous oxide has been used in all latest measurements for its clean spectrum in the sub-millimetre frequency range. Old methanol results by Zhang [63] are included in this section for comparison and additional verification of the post-processing procedure. All spectrum results concerned with gas emission spectra shown are brightness tem-

perature *differences* of two measurements. For each spectrum, a measurement with gas is compared to a measurement without gas. This was done to subtract any standing wave features in the spectrum due to the setup itself. Note that the possible multiplicative error due to the standing wave is not removed. The resulting spectra can be non-zero, since environmental temperature drifts can cause differences in the baseline temperatures between both measurements. Note that the post-processing step where the common profile is removed has an effect on the baseline as well, see Section 4.

Nitrous Oxide

The gas cell setup has been able to detect the spectrum of 30 mbar nitrous oxide (N_2O) with a measurement of 100 seconds. A lower pressure of 0.5 mbar over 1000 seconds was not detectable. Several iterations have been tested for detecting the spectrum of 0.5 mbar nitrous oxide, but none resulted in a spectrum with distinct nitrous oxide features. See Figure 5.13 for the output spectra of 30 mbar and 0.5 mbar. In this figure, one can see the nitrous oxide spectral line for 30 mbar and an approximately flat output for 0.5 mbar. The spectra represent the average over half the record length, in accordance with the maximum range of confidence for total deviation.

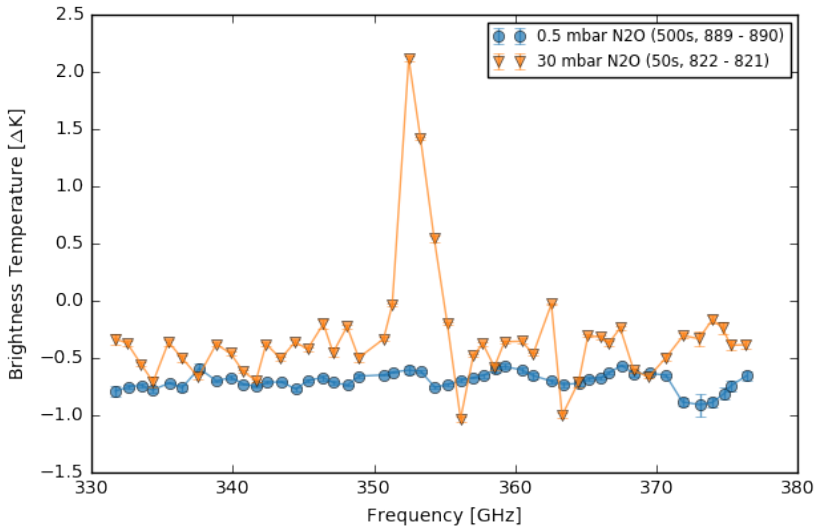

Figure 5.13: The output spectra for nitrous oxide (N_2O) at 30 mbar and 0.5 mbar. The spectra are obtained by subtracting an empty gas cell measurement to remove features caused by the setup, as such the difference in brightness temperature between two measurements is seen here. The negative baseline temperature can be explained by temperature drifts between these measurements, as well as the common profile removal during post-processing. The error bars represent the total deviation of the two runs accounted for subtraction. The data points represent the average over half the record length, in accordance with the maximum range of confidence for total deviation. **Triangles**: 30 mbar nitrous oxide for 50 seconds of averaging of a 1000-second measurement. The main nitrous oxide peak within the frequency band can be discerned distinctly. Note, this spectrum is subtracted with an 0.5 mbar N2O measurement to reduce standing features, since the empty gas cell zero measurement before this gas measurement failed. **Circles**: 0.5 mbar nitrous oxide averaged for half of 1000 seconds of measuring. No typical nitrous oxide features can be discerned.

Methanol

For methanol (CH_3OH) the results are based on data from older setup iterations by Zhang. The resulting spectra show distinct methanol features for 1 mbar over 50 seconds integration, but fail to detect 0.1 mbar over 50 seconds. The spectra for 1 mbar and 0.1 mbar methanol can be seen in Figure 5.14. The error bars are of larger size than in the previous nitrous oxide spectrum. This is believed to be due to the improved stability of the newer iteration of the gas cell setup.

5.3.2. Overall Offset of the Filterbank Center Frequencies

With the detected spectral lines for both nitrous oxide and methanol, the overall frequency offset of the center frequency for each DESHIMA filter could be found. These center frequencies were obtained using the terahertz frequency sweep measurement. This calibration measurement uses a terahertz line source with an unknown offset. See sections B.3 and 3.2.1 and 4.4 for the simulation procedure, frequency sweep measurement and shift selection procedure. With the offset known, the output can be corrected for more accurate

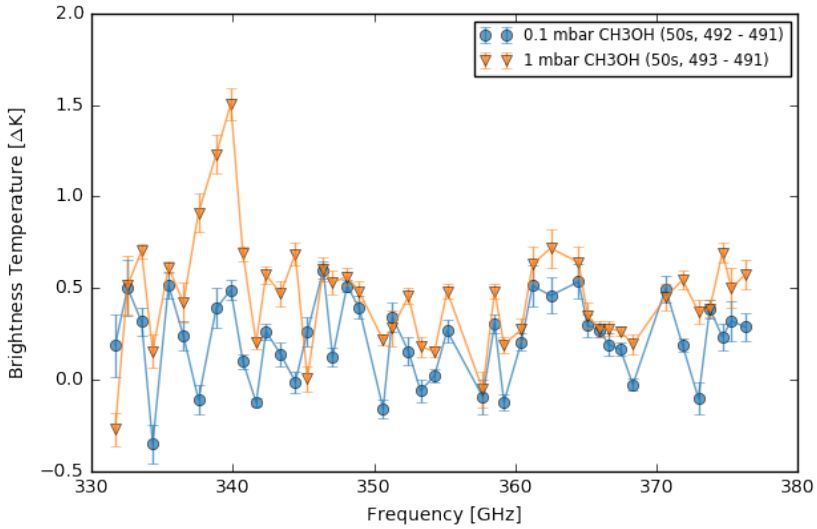

Figure 5.14: The output spectra for methanol (CH_3OH) at 1 mbar and 0.1 mbar. The spectra are obtained by subtracting an empty gas cell measurement to remove features caused by the setup, as such the difference in brightness temperature between two measurements is seen here. The negative baseline temperature can be explained by temperature drifts between these measurements, as well as the common profile removal during post-processing. The error bars represent the total deviation of the two runs accounted for subtraction. The data points represent the average over half the record length, in accordance with the maximum range of confidence for total deviation. **Triangles**: 1 mbar methanol averaged over half of the 100-seconds measurement. The main methanol peak within the frequency band can be discerned. **Circles**: 0.1 mbar methanol averaged over half of the 100-seconds measurement. No typical methanol features can be discerned.

results. The expected spectrum was simulated for a range of frequency offsets and fitted to the measurement data. The best fitted profile was determined based on the chi squared statistic. The offset corresponding to the best fit was taken as the overall frequency offset.

Nitrous Oxide (30 mbar, 50s)

The frequency offset for the detected nitrous oxide (N_2O) emission profile for 30 mbar over 50 seconds was found as Δf = -1.08 GHz. Figure 5.15a shows the data for 50 seconds 30 mbar nitrous oxide with the simulated profile corresponding to the found frequency offset. This offset denotes the shift of the 'true' spectrum with respect to the measured spectrum. For improved accuracy, the shift Δf is to be applied onto the measured spectrum.

Methanol (1 mbar, 50s)

The frequency offset for the detected methanol (CH_3OH) emission profile for 1 mbar over 50 seconds was found as Δf = -0.96 GHz. Figure 5.15b shows the data for 50 seconds 1 mbar methanol with the simulated profile corresponding to the found frequency offset.

5.3.3. Minimum Detectable Pressure Expectations

The sensitivity limits of DESHIMA 1.0 can be translated to minimum detectable gas pressures using the gas cell setup simulation model. This model was initially developed by Zhang and is covered in section B.2. The model showed that for a signal-to-noise ratio of >5 and 8 hours of integration, one could detect the main spectral lines of 0.02 mbar nitrous oxide or 0.0025 mbar methanol. Note, this is assuming perfect setup stability, where the detector is only limited by photon and quasiparticle recombination noise, as described in Equation 2.29. For shorter integration time, the minimum detectable pressure increases, generally following $P \propto 1/\sqrt{t}$, with P either power or pressure, and t the integration time. Several expected detectable pressures under these ideal conditions for different integration times can be seen in Table 5.7.

The typical detectable pressures in the table would show that 0.5 mbar nitrous oxide and 0.1 mbar methanol should have been detectable after averaging about 100 and 10 seconds, respectively. The reality that this is not the case indicates either an incorrect model or the presence of additional noises and errors aside from photon noise. Both modelled spectra for 30 mbar nitrous oxide and 1 mbar methanol show good resemblance to the detected spectra in both overall profile and in absolute brightness temperature. See Figures 5.16a and 5.16b,

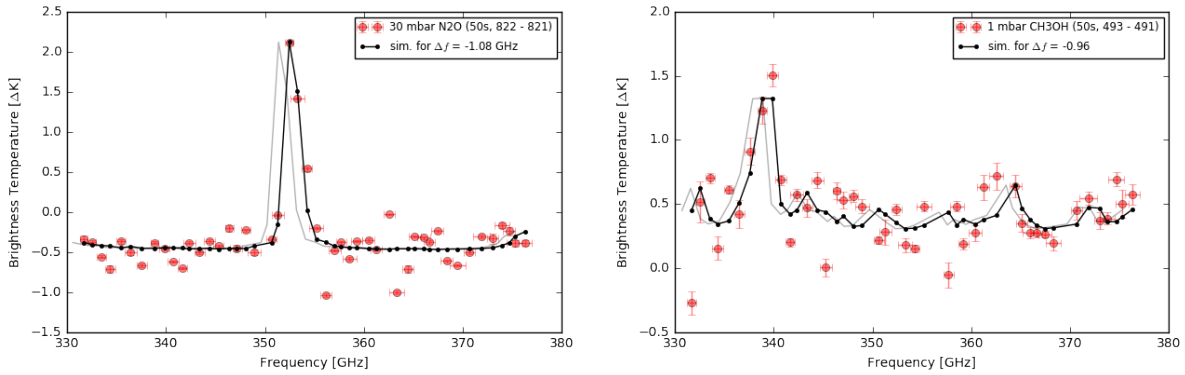

(a) (b)

Figure 5.15: Overall frequency offset of the filterbank center frequencies. Simulated spectra with frequency offsets were fitted to the measured data with distinct spectral features, to determine the overall frequency offset. The light grey lines indicate the response at the 'true' frequencies, by applying the offset onto the simulation. **(a)**: The emission spectrum for 30 mbar nitrous oxide averaged over 50 seconds, with a 0.5 mbar 500-second average of a 1000-second measurement subtracted serving as an empty gas cell baseline. The best fitted simulation profile was found at an overall frequency offset of Δf = -1.08 GHz. **(b)** The emission spectrum for 1 mbar methanol averaged over 50 seconds, with a 50-second average of a 100-second empty gas cell measurement subtracted, serving as a baseline. The best fitted simulation profile corresponded to an overall frequency offset of Δf = -0.96 GHz.

Averaging time	**Modeled detectable pressure**	
	Nitrous oxide (N2O)	**Methanol (CH3OH)**
10 s	1.0 mbar	0.1 mbar
100 s	0.3 mbar	0.03 mbar
1000 s	0.1 mbar	0.01 mbar
8 h	0.02 mbar	0.0025 mbar

Table 5.7: Typical nitrous oxide and methanol pressures corresponding to a >5 signal-to-noise ratio for several averaging times with the gas cell setup. These pressures were obtained with the gas cell simulation model. Note that these pressures serve as a rough indication of pressures needed for a detectable spectrum, not as accurate lower pressure boundaries. The model assumes a photon noise limited detection with perfect system stability.

respectively. The results in the figure indicate that the model is reasonably correct, and that the detectability of the lower pressures is limited by system instabilities. Note, these figures seem similar to the previous shown figures, but show different results. The previous figures showed the best fitted frequency shift. Here, the modelled gas cell setup emission is shown. This gas cell model is different from the previous frequency shift offset simulations. The simulations of frequency shift were concerned with how the cryostat system and DESHIMA filters affects incoming radiation. The gas cell model uses those too, but is in addition a simulation of the emission of the gas cell setup. It does so by considering the frequency dependent blackbody emission of a gas inside a cell with partially transmitting windows in front of a cold background. See Appendix B for detailed information on both simulations.

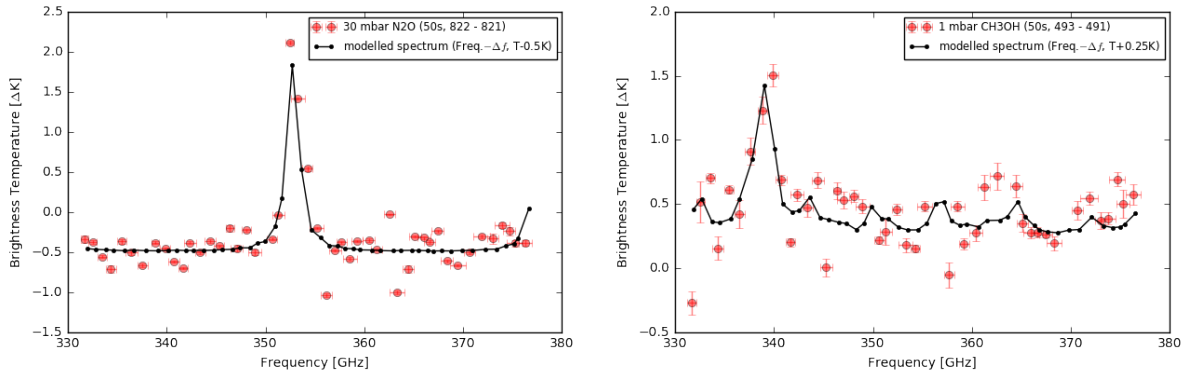

(a) (b)

Figure 5.16: Spectra simulated using the gas cell model compared to measured spectra. The modelled spectra show a good resemblance in profile features and absolute size with the measured spectra. Note, the black line is a different method of simulation than shown in Figures 5.15a and 5.15b. The modelled spectra are shifted in frequency and temperature to account for the offsets in the actual measurements. The frequency offsets are determined by detailed simulations, see section 5.3.2, the temperature baseline offsets are chosen conveniently.**(a)** Modelled 30 mbar nitrous oxide spectrum compared to its measured spectrum. **(b)** Modelled 1 mbar methanol spectrum compared to its measured spectrum.

Since the modelled spectra showed good resemblance with the detected spectra for 30 mbar nitrous oxide and 1 mbar methanol, the modelled spectra for 0.5 mbar nitrous oxide and 0.1 mbar methanol could as well confidently be compared with the measured spectra. This allowed for better understanding as to why the lower pressures were not detectable. Projecting the modelled spectra on the measured spectra showed that the instabilities due to the setup are currently too large to detect the low pressures. See Figures 5.17a and 5.17b for the modelled spectra of nitrous oxide and methanol, respectively.

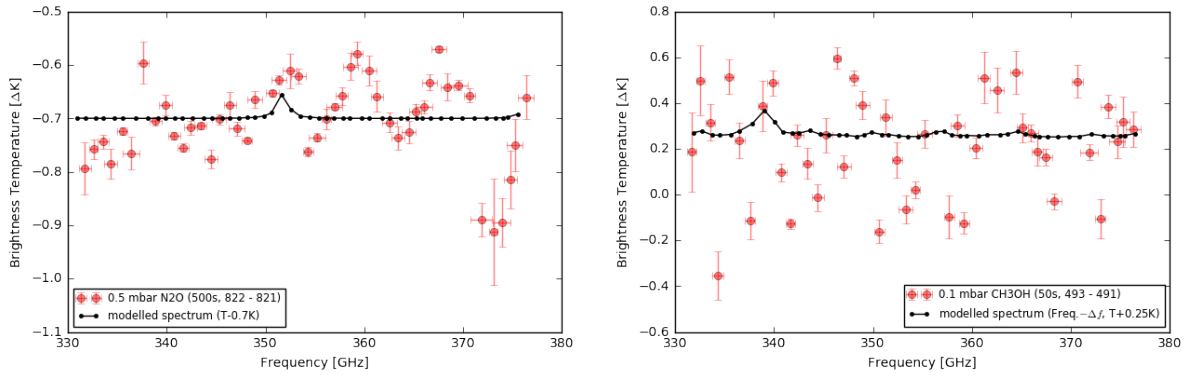

(a) (b)

Figure 5.17: Modelled spectra compared to its measured spectrum. The error in the measured data is too large to detect the 0.5 mbar nitrous oxide and 0.1 mbar methanol spectra. The modelled spectra are shifted in temperature baseline to account for the offset in actual measurements. The temperature baseline offsets are chosen conveniently. No frequency offset in the filterbank calibration is known for these measurements, since the offset determination as of section 5.3.2 requires distinct measured features. **(a)** Modelled 0.5 mbar nitrous oxide spectrum compared to its measured spectrum. **(b)** Modelled 0.1 mbar methanol spectrum compared to its measured spectrum.

5.3.4. Effect of the Gas Cell Windows on the Spectrum

The distinct standing wave in the output spectrum was present in every measurement with a spectral period of ~11.5 GHz. Literature research into optical resonances found Fabry-Pèrot like cavities to be a probable origin for the standing wave. It was found that the spectral period is similar to the free spectral range of a Fabry-Pèrot cavity for 8 mm of HDPE in air. See Figure 5.18 for several measured spectra with HDPE windows inside the gas cell, compared with a simulated profile based on treating the windows as Fabry-Pèrot cavities. See section 2.3.1 for more information on the calculation behind Fabry-Pèrot cavities.

Note that in addition to the Fabry-Pèrot resonance, wave returning features can be seen in the measured spectra. Two peaks are visible in the troughs of the standing wave profile at ~344 GHz and ~356 GHz. The exact origins of these peaks are currently unknown. They could indicate an interference at the respective terahertz frequencies. Another likely explanation is a systematic (read-out) error related to the MKID or coupled filter. Further research is needed to find the exact origin of these peaks.

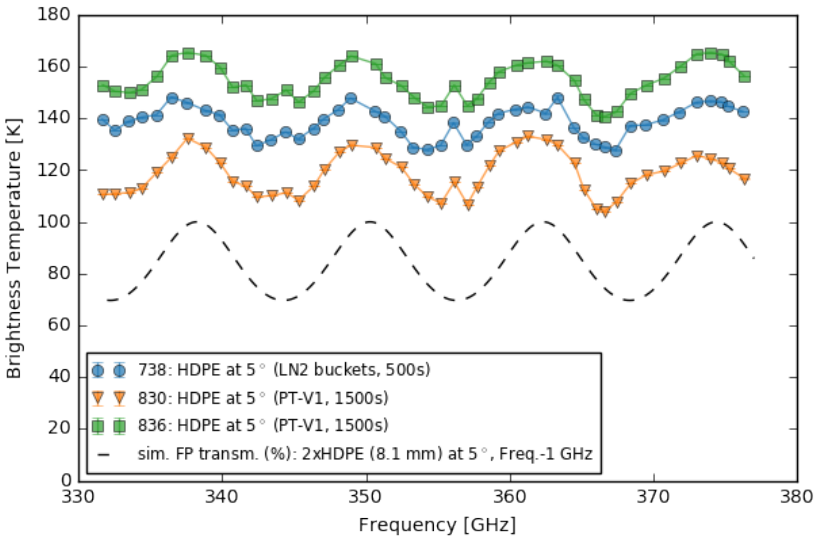

Figure 5.18: Empty gas cell measurements with HDPE windows showed a distinct and reproducible standing wave in the output spectrum. The standing wave follows simulated Fabry-Pèrot behaviour, with constructive and destructive internal reflections, when considering the individual windows as Fabry-Pèrot cavities. Aside from the Fabry-Pèrot profile, small returning peaks in the standing wave troughs at ~344 GHz and ~356 GHz could be seen. Baseline differences were present and are believed to be due to slight misalignment of the optics. **Triangles/Squares**: Empty gas cell measurements with ~8 mm HDPE windows tilted 5°at opposing orientation,PT-V1 LN2 target as background. **Circles**: An empty gas cell measurements with ~8 mm HDPE windows tilted 5°at opposing orientation, two LN2 buckets as background. **Dashed line**: Simulated transmission profile of two subsequent Fabry-Pèrot cavities similar to the angled windows. Cavities of 8.1 mm angled at 5° with refractive index of 1.54 (HDPE) submersed in air were used for the simulations.

The spectra in Figure 5.18 indicate the importance of good alignment of the setup. The risk of spillover detection due to misalignment is high, since the optical paths are narrow in the setup. A slight misalignment typically results in baseline temperature offsets of tens of Kelvins. Even the best aligned measurements with an empty gas cell still showed a ~50 K difference between the on-source and off-source paths. Since the conversion from relative frequency shift to brightness temperature follows a square root dependence, a temperature offset due to misalignment does not only cause incorrect baseline temperatures, but could as well cause a faulty amplification of the spectrum profile.

An anti-reflective grating was designed and milled into TOPAS sheets to counter the standing waves. The TOPAS windows with anti-reflective grating successfully reduced the standing wave in the profile. In Figure 5.19 one can see the distinct standing wave due to the HDPE windows and the elimination of the standing wave with the anti-reflective grating in TOPAS. The improved and stabilized spectra allowed for previously unnoticed features to be visualized. One might argue there is a shallow standing wave in the spectra of the TOPAS measurements. Figure 5.19 also includes a simulation of two Fabry-Pèrot cavities similar to the TOPAS windows with anti-reflective coating. One side of the cavity is now given a reflectivity of 1% instead of the air-to-TOPAS Fresnel reflectivity of 4.26%. The simulation for the Fabry-Pèrot resonance of 10 mm TOPAS does seem to follow the periodicity of the measured profiles, especially for the frequency range above 350 GHz. However, the wave like profile in the measured data is quite shallow compared to other features deviating from a flat spectrum.

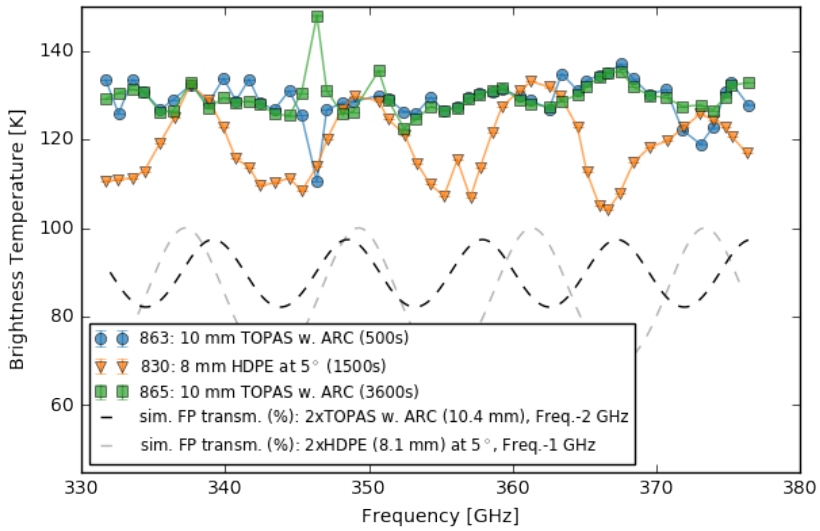

Figure 5.19: Impact of window type on the detected brightness temperature spectrum. The anti-reflective grating in TOPAS successfully removed the distinct standing wave due to the HDPE windows. The newly found stabilized profiled might follow a Fabry-Pèrot profile for 10 mm TOPAS, but this cannot be claimed with certainty. Again, baseline differences can be seen and are believed due to slight misalignment of the optics. **Circles/squares**: Empty gas cell measurements with 10 mm TOPAS windows with their inner sides treated for an anti-reflective grating. The outliers at ~347 GHz are believed to be a misbehaving MKID. **Triangles**: An empty gas cell measurement with 8 mm HDPE windows tilted 5°at opposing orientation. **Dashed line**: Simulated transmission profile of two subsequent Fabry-Pèrot cavities similar to the TOPAS windows. Cavities of 10.4 mm with refractive index of 1.54 (TOPAS) submersed in air with one side a lowered reflectivity were used for the simulations. For comparison simulations of uncoated 8.1 mm HDPE angled at 5° are included.

5.3.5. Effect of Magnetic Shielding on the Spectrum

With the improved spectrum profile due to the reduction of the standing wave, other features that previously went unnoticed can now be seen. These features are limiting for a clean spectrum. During several trials, it became clear that the setup was susceptible to magnetic interference. When magnets or metallic structures were moved within a few meters of the setup, it could be seen in the live MKID outputs. The lack of magnetic shielding of the DESHIMA detector in the Hydra cryostat was found to be a limiting factor for a stable spectrum. A magnetic shield was installed for the DESHIMA detector in the Hydra cryostat, see Figure 5.20. This magnetic shielding stabilized the spectrum further.

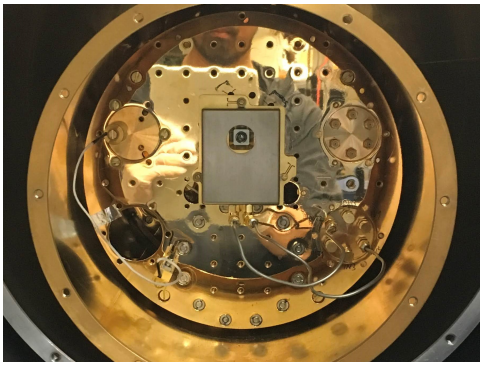

Figure 5.20: Photograph of the DESHIMA chip inside its magnetic shield (grey). The chip with shield is mounted inside the Hydra cryostat (without the snout).

It is difficult to visualize this improvement in data, since the magnetic interference was not as structural as the Fabry-Pèrot resonance. In Figure 5.21 the spectra of pre- and post-magnetic shielding can be seen. The spectrum with shielding seems to be more stable for subsequent measurements. The mean absolute difference of run 865-863 was higher at 2.93K compared to run 890-888 at 0.22K. Stability of the spectrum for subsequent measurements is of importance, since the calibrations and zero-measurements assume a setup stable over time. The shielded spectra are arguably less distorted as the standard deviation of the spectra are slightly reduced compared to the unshielded spectra. However, it is inconclusive whether the lower standard

deviation can be attributed to the shielding, as the impact of other instabilities are as well present. It is however promising that the shielded spectrum is less distorted, even with more spillover detection. The baseline temperature is higher and believed to be indicative of the amount of spillover radiation detected.

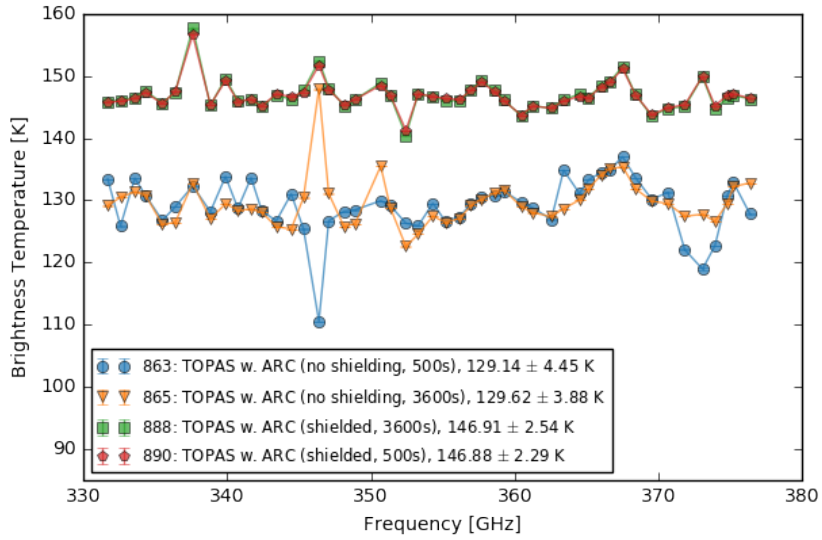

Figure 5.21: Impact of magnetic shielding on the detected brightness temperature spectrum. Magnetic shielding reduced aberrations in the spectrum profile between subsequent measurements. The magnetic shielding is believed to have stabilized the spectra. Again, baseline differences can be seen and are believed due to slight misalignment of the optics. **Circles/Triangles**: Subsequent empty gas cell measurement with TOPAS windows and no magnetic shielding around the DESHIMA detector. **Squares/Diamond**: Subsequent empty gas cell measurement with TOPAS windows and magnetic shielding around the DESHIMA detector.

An empirical formula by [36] can be used to estimate the typical magnetic shielding needed for MKIDs in a similar cryostat setup to reduce the impact of environmental magnetic fluctuations. They found their formula as

$$S \sim 20 \cdot \log_{10}\left(\frac{2.4 \cdot 2.3 \cdot 10^{-14}\ \mathrm{W}/\sqrt{\mathrm{Hz}}}{\mathrm{NEP}}\right). \tag{5.1}$$

For DESHIMA 1.0 the ideal photon noise limited NEP is estimated to be NEP $\sim 3 \cdot 10^{-16}$ W/Hz$^{-0.5}$. According to this formula, a magnetic shielding of $S \sim 45$ dB would be required to sufficiently reduce the environmental magnetic interference. For comparison, the shielding in the Beast cryostat is around 25 dB. The exact shielding of the grey casing used in Hydra is unknown. The influence of magnetic interference might therefore still be present to a degree. Further investigation of magnetic interference and the magnetic shielding of the Hydra cryostat is required to better understand the limiting extent of the magnetic interference.

6

Conclusion

A gas cell measurement setup has been investigated and optimized to evaluate the performance of wideband sub-millimeter spectrometers like DESHIMA (DEep Spectroscopic High-redshift MApper). The use of low pressure gas emission spectra allowed for accurate calibration of the absolute frequency response and to test the detectability of faint emission spectra. The use of gas emission spectra for calibration of spectrometers is not new, but limited research has been done for wideband sub-millimeter detectors.

This thesis work continued on the setup by Zhang with the prototype DESHIMA detector. Zhang was able to detect 1 mbar methanol gas over 100 seconds and to estimate an absolute frequency offset of the DESHIMA filterbank. The setup faced two limiting aspects for testing with lower pressures and longer integration times. The output spectra of measurements showed a dominant standing wave, obscuring the detection of spectral features in a single measurement, and possibly multiplicatively altering the emission profile. A second zero-measurement was therefore required to detect the standing features and subtract them from the initial measurement. Furthermore, Allan deviation analysis showed a system stability of only ~ 10 seconds for some channels, after which noises of unknown origin would limit the stability necessary for longer averaging times.

The research presented here has shown a successful improvement on the setup by addressing the standing wave and the low noise stability. An investigation into optical resonances found reflections inside the gas cell windows to cause the standing wave in the spectrum. A one-dimensional anti-reflective pyramid grating was designed and fabricated into TOPAS sheets. The anti-reflective layer successfully removed the standing wave profile. Extensive system stability testing and total deviation analysis was applied in an iterative research process to improve on the system stability. Several stability-limiting components were found in the setup, such as the background and the method of mounting the detector in the cryostat. The double background was replaced by a single target, and the mounting method in the cryostat was adapted. The detailed analysis deepened the understanding of the stability impact of key components of the setup. As part of the stability testing and analysis, several post-processing algorithms have been written to improve the output stability. The final post-processing procedure developed consists of two stages. First, linear drifts for each MKID output are determined and removed. Second, a common profile over all MKID outputs is removed from the data set. The system stability of the latest iteration of the setup, together with the post-processing procedure, was improved to integration times of $\sim 10^3$.

Even though the standing wave is removed from the output spectrum, the spectrum still showed deviations from a flat spectrum larger than the expected emission spectra. This required the continued use of a second zero-measurement. The system stability improvement of several orders of magnitude was not enough to overcome instabilities occurring over the two separated measurements. The system was not able to detect 0.5 nitrous oxide in 1000 seconds. System simulations of the gas cell setup with the DESHIMA prototype showed that a photon noise limited system should be able to detect 0.5 mbar nitrous oxide in ~ 40 seconds. The lack of detected emission spectrum indicates limiting instabilities still present in the gas cell setup.

Outlook & Recommendations for Further Research

The overall conclusion of this research is therefore that the latest setup has been an improvement on the previous work by Zhang in both stability over time and removing the standing wave features, but does not yet allow for evaluation of wideband sub-millimeter detectors for long integration times. Further improvement

of the setup is required to better characterize the performance of wideband sub-millimeter detectors up until their photon limited behaviour.

A crucial error has been the detection of environmental radiation, which is believed to cause nonlinear drifts and to affect the results more than previously anticipated. To reduce spillover radiation, focus should primarily be on good optical coupling of gas cell setup to the detector inside the cryostat. Care has to be taken for a mechanical stable system as well to limit mechanical resonance affecting the MKID read-out. Once optical coupling between setup and detector is sufficient, focus should be on improving the alignment of the optical paths in the setup. A redesign of the optical setup is likely required, where one should consider the following design guidelines ordered by importance.

1. The optical paths should be given sufficient lateral spacing to limit reflections of neighbouring components.
2. The optical paths should be easy to align to improve the reproducibility of subsequent measurements.
3. Any unwanted reflective surfaces in the optical paths at risk of being detected should be coated with an absorbing material in the wideband range of operation.

In addition to the optical coupling and proper alignment, other directions expected to lead to improvements of the setup and this research are as follows.

- Investigate the environmental radiation in the frequency range of the detector. This is of interest both to better understand possible frequency dependent spectrum errors, as to identify their origins for effective spillover reduction.
- Investigate the magnetic field changes around the cryostat. The MKID based detector was found to be sensitive to moving magnets and metallic objects. A magnetic shield of ~25 dB is applied, but this is likely not sufficient.
- Improve the common profile removal algorithm. Trials have been done with principal component analysis and machine learning regression models, but have not yet shown improved results to the common mean algorithm.
- Investigate the correlation of worse performing MKIDs to its design and read-out parameters. The stability performance was not similar for all MKIDs. Most MKIDs would show good stability over the full measurement, while a few outliers would show an optimum averaging time worse of several orders of magnitude difference. The bad performing MKIDs would be different per measurement and could not be correlated to a measurement parameter.
- Identify additional gas candidates with main spectral lines in different frequency ranges of the spectrum of interest. This would allow for better coverage of detectability testing over all sections of the spectrum.

It is furthermore important to reconsider the assumption made in the introduction on the stability of the DESHIMA detector. For this thesis, the DESHIMA detector used to evaluate the stability of the setup was assumed to be stable for at least 800s of continuous integration. Any instabilities found before that point were therefore allocated to the setup. With the latest setup improvements, the stability over time has reached the point where it becomes harder to pinpoint an instability to originate in the gas cell setup, or in the detector itself. Therefore, on a final note, it would be of great interest to evaluate DESHIMA 2.0 with the setup and compare the results to the results presented in this work. This comparison could indicate whether the instabilities in the experiments were truly due to the gas cell setup or due to unexpected effects inside the DESHIMA prototype detector used.

A

Run Overview

See next page for a table of all runs used in this research. Note:

- ID: The identification number assigned to a measurement run.
- Type: The runs have been assigned types for improved overview of the table, see as well section 3.2 for an in depth overview of measurement types.
  - Gas spectrum measurement (GS)
  - No gas measurement functioning as zero measurement (Z)
  - Stability check measurement (ST)
  - Rotating grid calibration (RG)
  - Terahertz sweeping line calibration (SL)
- t: Measurement duration.
- P: Pressure inside the gas cell.
- T_{room}: The temperature of the room and the setup.
- Background: The background type used, as described in section 3.1.9.
- Cell Window: The gas cell window type, see section3.1.6
- f_{chop}: Chopping frequency. Note that the chopper disc has two wings and rotates at half the chopping frequency.
- f_{sampl}: Sampling rate of the data read-out.
- Cryostat: Cryostat system used. The (*) behind runs with the Hydra cryostat denotes the removal of the 'snout'.
- EM Shield: Electromagnetic shielding of the DESHIMA chip.
- Date: Date of measurement, format: yyyymmdd.

ID	Type	t (s)	P (mbar)	T_{room} (C)	Background	Cell Window	f_{chop} (Hz)	f_{samp}	Cryostat	EM Shield	Date	Comment
491	Z	100	0	?	2x LN2 Bucket	HDPE 5ř	10	1200	Beast	yes	20190418	Base for 492-493
492	GS	100	0,1	?	2x LN2 Bucket	HDPE 5ř	10	1200	Beast	yes	20190418	0.1 mbar CH3OH detected
493	GS	100	1	?	2x LN2 Bucket	HDPE 5ř	10	1200	Beast	yes	20190418	1 mbar CH3OH detected

Table A.1: Measurement runs done by Zhang to detect methanol with the old version of the setup. Zhang was able to detect 1 mbar, but not 0.1 mbar. These runs are included for comparison purposes.

ID	Type	t (s)	P (mbar)	T_{room} (C)	Background	Cell Window	f_{chop} (Hz)	f_{samp}	Cryostat	EM Shield	Date	Comment
733	SL	-	-	-	-	-	-	160	Hydra	no	20201214	
736	NS	1000	0	20,2	2x LN2 Bucket	HDPE 5ř	off	160	Hydra	no	20201214	
738	Z	1000	0	20,4	2x LN2 Bucket	HDPE 5ř	10	160	Hydra	no	20201214	Base for 740-741
739	RG	200	-	21,1	2x LN2 Bucket	HDPE 5ř	10	160	Hydra	no	20201214	
740	GS	1000	0,5	21,6	2x LN2 Bucket	HDPE 5ř	10	160	Hydra	no	20201214	0.5 mbar N2O undetected
741	GS	100	30	22	2x LN2 Bucket	HDPE 5ř	10	160	Hydra	no	20201214	30 mbar N2O detected

Table A.2: Initial measurements with the adopted gas cell setup. Nitrous oxide was detectable for 30 mbar, but not 0.5 mbar. A noise measurement of the setup with no chopping was done for analysis of the noise behaviour in the setup.

ID	Type	t (s)	P (mbar)	T_{room} (C)	Background	Cell Window	f_{chop} (Hz)	f_{samp}	Cryostat	EM Shield	Date	Comment
814	SL	-	-	-	-	-	-	160	Hydra	no	20210325	
815	NS	1000	-	21,4	-	-	-	1200	Hydra	no	20210326	Eccosorb in front of Hydra
816	NS	1000	0	21,6	Eccosorb	HDPE 5ř	off	1200	Hydra	no	20210326	Eccosorb as bg., no chopping
817	ST	1000	0	21,8	Eccosorb	HDPE 5ř	10	1200	Hydra	no	20210326	Eccosorb as bg., w/ chopping
818	RG	200	-	22	LN2 PT-V1	HDPE 5ř	10	1200	Hydra	no	20210326	
819	NS	1000	0	21,4	LN2 PT-V1	HDPE 5ř	off	1200	Hydra	no	20210326	Full setup, without chopping
820	Z	1000	0	21	LN2 PT-V1	HDPE 5ř	10	1200	Hydra	no	20210326	Unusable due to read-out errors
821	GS	1000	0,5	21,5	LN2 PT-V1	HDPE 5ř	10	1200	Hydra	no	20210326	Used as base for 822
822	GS	100	30	21,4	LN2 PT-V1	HDPE 5ř	10	1200	Hydra	no	20210326	30 mbar N2O detected

Table A.3: First measurements with the single LN2 background target PT-V1. This greatly improved the stability over time. Several additional noise measurements using an Eccosorb sheet at room temperature were done to better understand the noise characteristics originating in the setup.

ID	Type	t (s)	P (mbar)	T_{room} (C)	Background	Cell Window	f_{chop} (Hz)	f_{samp}	Cryostat	EM Shield	Date	Comment
825	SL	-	-	-	-	-	-	1200	Hydra	no	20210409	
827	ST	3000	0	22,3	Eccosorb	HDPE 5ř	10	1200	Hydra	no	20210409	Eccosorb as background
829	RG	100	-	21,1	LN2 PT-V1	HDPE 5ř	10	1200	Hydra	no	20210409	
830	ST	3000	0	21,3	LN2 PT-V1	HDPE 5ř	10	1200	Hydra	no	20210409	First 3000s cold run
831	ST	3000	0	20,4	LN2 PT-V1	HDPE 5ř	20	1200	Hydra	no	20210409	Increased chopper frequency
832	Z	1000	0	20,4	LN2 PT-V1	HDPE 5ř	10	1200	Hydra	no	20210409	Base for 833
833	GS	2000	0,5	20,7	LN2 PT-V1	HDPE 5ř	10	1200	Hydra	no	20210409	0.5 mbar N2O undetected

Table A.4: Long integration time behaviour was investigated up to 3000 seconds. A higher chopping frequency was tested to investigate the impact of chopping frequency. A longer 0.5 mbar measurement was tried for 2000 seconds, but was undetectable.

ID	Type	t (s)	P (mbar)	T_{room} (C)	Background	Cell Window	f_{chop} (Hz)	f_{samp}	Cryostat	EM Shield	Date	Comment
834	ST	3000	0	21	Eccosorb	HDPE 5ř	10	1200	Hydra	no	20210511	
835	RG	100	-	20,9	LN2 PT-V1	HDPE 5ř	10	1200	Hydra	no	20210511	
836	ST	3000	0	20,9	LN2 PT-V1	HDPE 5ř	10	1200	Hydra	no	20210511	
837	ST	4000	0	21,1	Eccosorb	HDPE 5ř	10	1200	Hydra	no	20210517	
839	ST	4000	0	21,4	Empty PT-V1	HDPE 5ř	10	1200	Hydra	no	20210517	
840	ST	4000	0	21	Empty PT-V1 (rot.)	HDPE 5ř	10	1200	Hydra	no	20210518	PT-V1 rotated (other window)
841	ST	4000	0	21,5	Empty PT-V1	HDPE 5ř	10	1200	Hydra	no	20210518	All paths aligned to blackbody in PT-V1
842	ST	3000	0	21,7	LN2 PT-V1	HDPE 5ř	10	1200	Hydra	no	20210518	Same alignment as 841
843	ST	3000	0	21,7	LN2 PT-V1 (rot.)	HDPE 5ř	10	1200	Hydra	no	20210518	PT-V1 rotated (other window)

Table A.5: Several alignment tests were done in order to improve the alignment of the optical paths. This included aligning the paths with the blackbody inside the PT-V1 target and investigating the impact of the different sides of the PT-V1 target to rule out unwanted polarization effects of the LN2 target.

ID	Type	t (s)	P (mbar)	T_{room} (C)	Background	Cell Window	f_{chop} (Hz)	f_{samp}	Cryostat	EM Shield	Date	Comment
860	SL	-	-	-	-	-	-	1200	Hydra	no	20210621	
862	RG	100	-	21	LN2 PT-V1	TOPAS, ARC	10	1200	Hydra	no	20210621	Failed, rot. grid asymmetric
863	ST	3000	0	21,1	LN2 PT-V1	TOPAS, ARC	10	1200	Hydra	no	20210621	
864	RG	100	-	21,1	LN2 PT-V1	TOPAS, ARC	10	1200	Hydra	no	20210623	Half rotations only
865	ST	7200	0	21,2	LN2 PT-V1	TOPAS, ARC	10	1200	Hydra*	no	20210623	Rot. grid motor off, first 7200s run
866	ST	3000	0	21,3	LN2 PT-V1	TOPAS, ARC	10	1200	Hydra*	no	20210623	**Rot. grid removed**

Table A.6: Testing of the new anti-reflective coated TOPAS windows. Magnetic influences were found and the motor of the rotating grid seemed to be influencing the results. Several tests on the impact of the rotating grid were performed. System stability was tested up to 7200 seconds.

ID	Type	t (s)	P (mbar)	T_{room} (C)	Background	Cell Window	f_{chop} (Hz)	f_{samp}	Cryostat	EM Shield	Date	Comment
885	RG	100	-	21,4	LN2 PT-V1	TOPAS, ARC	10	1200	Hydra*	yes	20210714	**Failed, bad alignment**
886	ST	3000	0	21,4	LN2 PT-V1	TOPAS, ARC	10	1200	Hydra*	yes	20210714	Bad alignment
887	RG	100	-	21,1	LN2 PT-V1	TOPAS, ARC	10	1200	Hydra*	yes	20210715	
888	ST	7200	0	21,2	LN2 PT-V1	TOPAS, ARC	10	1200	Hydra*	yes	20210715	Rot. grid motor off
889	GS	1000	0,5	21,1	LN2 PT-V1	TOPAS, ARC	10	1200	Hydra*	yes	20210715	Rot. grid motor off
890	Z	1000	0	21,2	LN2 PT-V1	TOPAS, ARC	10	1200	Hydra*	yes	20210715	0.5 mbar undetected, rot. grid motor off

Table A.7: Long time stability tests with magnetic shielding and the snout removed. These were expected to be the most stable runs. Several system check measurements were done. A final try to detect 0.5 mbar nitrous oxide failed.

B

Setup Output Simulations

This chapter covers the simulation programs used for cross-validation of detected spectra, as well as obtaining sensitivity and efficiency expectations of the power propagation through the setup.

- Both programs use molecule opacity spectra as input. These spectra are generated with the AM Atmospheric Model software package [42]. This software allows for the simulation of detailed emission spectra of molecules in the sub-millimeter range. More information on the AM atmospheric Model software can be found in section B.1.
- One program was originally written by D. Zhang as part of her research designing the initial version of the gas cell setup. This program aims to find the power propagation per MKID through the setup. This simulation program is covered in section B.2 and is useful to find out which pressures are possible to be measured with the gas setup.
- Another program was originally written by K. Karatsu and aims to simulate the profile of a gas spectrum adapted for the detector and cryostat response. This simulation program is covered in section B.3.

B.1. The AM Atmospheric Model Software

The AM Atmospheric Model [42] is an extensive software tool for radiative transfer calculations in the range of millimeter to sub-millimeter wavelengths written by Scott Paine of the Smithsonian Astrophysical Observatory. Although its main focus is on atmospheric calculations covering layers of kilometers in depth, it can as well be used for laboratory testing simulations with layer depths of centimeters. The AM Atmospheric Model allows for simulating gas spectra for their use in DESHIMA's frequency range. For the gas cell setup the main interest was in simulating the transmittance of pure gas layers of 10 cm in depth.

The AM atmospheric model assumes plane waves travelling through plane-parallel layers. Radiation is assumed to be unpolarized, and multiple scattering is neglected. The layers are assumed to be in local thermodynamic equilibrium. The transmittance in The AM atmospheric model of single molecule gas is calculated based on the optical depth as

$$t(\nu) = e^{-\tau(\nu)}, \tag{B.1}$$

where $t(\nu)$ and $\tau(\nu)$, respectively, denote the transmittance and optical depth of the single molecule gas layer over the frequency spectrum. The optical depth is calculated for line by line absorption as

$$\tau(\nu) = N \cdot \sec(\theta_z) \cdot k(\nu, P, T), \tag{B.2}$$

where N is the molecular column density of the layer, θ_z the angle of propagation in the layer, and $k(\upsilon, P, T)$ a molecular absorption coefficient dependent on the pressure P and temperature T of the layer. With the length l of the layer known, the column density can be calculated from the temperature and pressure using the ideal gas law as

$$N = \frac{l}{k_B} \cdot \frac{P}{T}. \tag{B.3}$$

The radiative transfer of the layer can be found as

$$I_i(\nu) = B(\nu, T) \cdot (1 - t(\nu)) + I_{i-1}(\nu) \cdot t(\nu), \tag{B.4}$$

where $I_{i-1}(\upsilon)$ and $I_i(\upsilon)$ are the radiance power before and after the layer. Planck's radiance function $B_\nu(T)$ describes the spectral power of a body at absolute temperature T per unit area per unit solid angle for a particular radiation frequency as

$$B(\nu, T) = \frac{2h\nu^3}{c^2} \frac{1}{e^{\frac{h\nu}{k_B T}} - 1}, \tag{B.5}$$

where h is the Planck constant, and c is the speed of light in the medium, k_B is the Boltzmann constant. In the low frequency regime $h\nu \ll k_B T$ - including DESHIMA's frequency range - one can simplify Plank's law to the Rayleigh-Jeans law as

$$B(\nu, T) \approx \frac{2\nu^2 k_B T}{c^2}, \tag{B.6}$$

which essentially is a first order Taylor polynomial approximation of the exponential. The effective brightness temperature T_b can now be found using the inverse of the Rayleigh-Jeans approximation Plank's law and substituting the radiant power for the blackbody emission as,

$$T_{R-J}(\nu) = \frac{c^2}{2k\nu^2} \cdot I(\nu), \tag{B.7}$$

which shows one can also work with the brightness temperature directly instead of radiative power.

B.2. Simulating Power Propagation through the Gas Cell Setup

The program by Zhang allowed for simulating the power propagation through the setup. These simulations give a good estimate of the pressures detectable with the setup under ideal conditions. For further details, one is advised to visit Zhang's thesis [63]. The main steps consist of:

1. The gas opacity spectrum is simulated with The AM Atmospheric Model.
2. The radiative power spectrum after passing through the gas cell is calculated. The blackbody spectra of all components are combined and adjusted for subsequent transmission media.
3. The power spectrum reaching the detector inside the cryostat is obtained. The emission of the cryostat window is added, and the total is convoluted cryostat quasi-optical filterstack transmission.
4. The power coupled to each MKID is determined by convoluting the power spectrum at the detector with the MKID specific sub-millimeter filter response, and multiplied with several efficiencies representing the antenna and microchip performance.

B.2.1. Simulated Gas Opacity for the DESHIMA Spectrum

The transmission of a 10 cm layer of single molecule gas is simulated using The AM Atmospheric Model. The software allows for a pressure, layer thickness and frequency range as input. It will output the transmission factor over frequency. See subsection B.1 for more information on The AM Atmospheric Model. The transmittance spectrum is used to calculate the brightness temperature spectrum of the room temperature gas in front of the liquid nitrogen cold background, as

$$T_{signal}(f) = T_{background} + \left(T_{room} - T_{background}\right)\left(1 - t_{gas}(f)\right). \tag{B.8}$$

See Figure B.1 for a simulated nitrous oxide and methanol spectrum using The Atmospheric Model.

B.2.2. Emission power by the gas cell

The simulation of the emission power due to the gas cell setup is obtained by calculating the blackbody radiation of all transmission media using Planck's law. Since all gas cell components are at room temperature, one can simulate the emitted power in DESHIMA's spectrum using Planck's law at room temperature and adjust the emission power for the subsequent component transmission profiles. The combined power emission per frequency of the gas cell transmission media adjusted for the frequency dependent transmission $t(\nu)$ of each subsequent medium can then be formulated as

$$\begin{aligned}
P_{gas-cell}(\nu) = {} & B_\nu(T) && \cdot \eta_{spill-over} t_{window}^2 t_{gas} && \text{Background emission} \\
& + (1 - t_{window}) B_\nu(T_{room}) && \cdot \eta_{spill-over} t_{window} t_{gas} && \text{1st Window emission} \\
& + \left(1 - t_{gas}\right) B_\nu(T_{room}) && \cdot \eta_{spill-over} t_{window} && \text{Gas emission} \\
& + (1 - t_{window}) B_\nu(T_{room}) && \cdot \eta_{spill-over} && \text{2nd Window emission} \\
& + \left(1 - \eta_{spill-over}\right) B_\nu(T_{room}). && && \text{Spill-over}
\end{aligned} \tag{B.9}$$

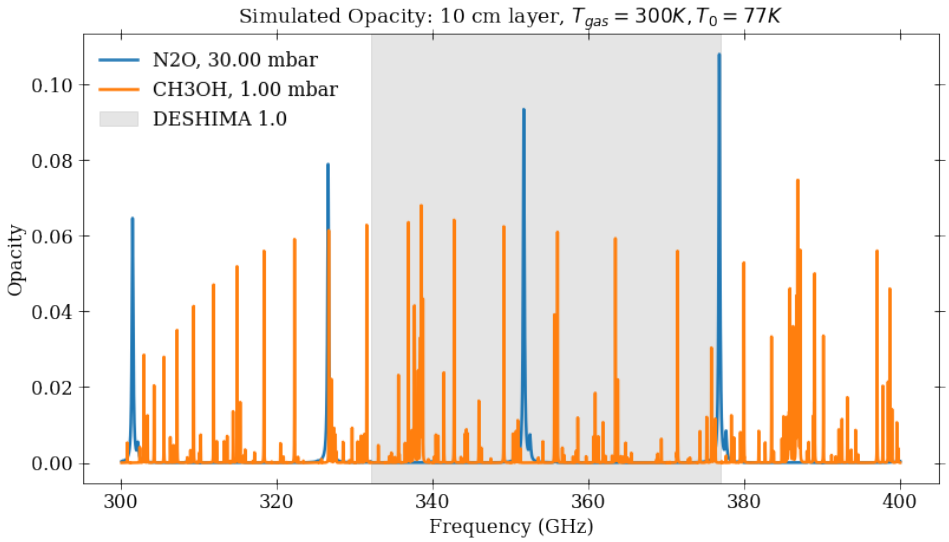

Figure B.1: Simulated opacity spectra for 30 mbar nitrous oxide and 1 mbar methanol at room temperature (300K) in front of a cold (77K) background. The spectra are simulated for a 10 cm layer for a frequency band from 300 to 400 GHz, with a line resolution of 0.001 GHz. The frequency range of DESHIMA 1.0 is indicated as a grey area.

The spill-over efficiency $\eta_{spill-over}$ of the gas cell setup has a unitary efficiency for no spillover radiation and optimal source propagation. Zhang approximated a spill-over efficiency of $\eta_{spill-over} \approx 0.74$ based on optical reflection simulations using the GRASP software by TICRA. This efficiency value has been used for the recent setup simulations as well, since the Gaussian beam shape propagation model used in the GRASP simulations is believed to still be in agreement with the newer gas cell setup.

B.2.3. Radiative power reaching the detector

To obtain the effective power of the gas cell setup reaching the detector, one has to account for the cryostat system response. The previous found gas cell emission is adapted for propagating through the cryostat window. The combined emission after the cryostat window is adapted for the quasi-optical filterstack transmission. The filterstack transmission is considered in more detail in section B.3.2 and visualized in Figure B.2. A polarization efficiency of $\eta_{pol.} = 1/2$ is included to account for the single polarization sensitivity of the detector. The wire grid in front of the cryostat window is aligned to this polarization limiting spill-over. This combines the simulation of the power reaching the detector to

$$\begin{aligned} P_{det.}(\nu) = P_{gas-cell} &\cdot t_{cryo-win.} t_{filterst.} \eta_{pol.} && \text{Gas Cell emission} \\ + \left(1 - t_{cryo-win.}\right) B_\nu(T_{room}) &\cdot t_{filterb.} \eta_{pol.} && \text{Cryostat Window emission} \end{aligned} \tag{B.10}$$

B.2.4. Power coupled to each MKID

To finally obtain the power coupled to an MKID one has to integrate over the antenna solid angle, the antenna area and the band-pass filter response of the respective MKID. The final power is as well factored for the efficiency of the DESHIMA microchip. For a single-mode antenna such as the antenna of the DESHIMA detector, the solid angle and area is given as

$$\Omega_A \cdot A_{antenna} = \frac{c^2}{\nu^2}. \tag{B.11}$$

The sub-millimeter filter response per MKID is designed to follow a Lorentzian profile. The Lorentzian profiles are obtained by reconstructing a normalized Lorentzian profile L_{i-MKID} based on the center frequency ν_0 and quality factor Q of each band-pass filter as

$$L_{i-MKID} = \frac{1}{1 + \left(\frac{\nu - \nu_0}{\mathrm{FWHM}/2}\right)^2} \quad \text{with} \quad \mathrm{FWHM} = \frac{\nu_0}{Q} \tag{B.12}$$

For the simulations with DESHIMA 1.0 the center frequencies and quality factors were derived from actual terahertz frequency sweep measurements, see 3.2.1. For DESHIMA 2.0 the designed filter center frequencies

and an overall quality factor Q = 500 were used. The Lorentzian profiles are multiplied with an antenna efficiency $\eta_{antenna}$ and a chip efficiency η_{chip} to account for losses inside the antenna and on the chip. These overall efficiencies are obtained as

$$\eta_{antenna} = \eta_{antenna-radiation} \cdot \eta_{antenna-spill-over} \tag{B.13}$$

where $\eta antenna - radiation$ is the radiation efficiency of the lens antenna and $\eta antenna - spill - over$ is the spill-over efficiency for optical coupling to the antenna on the chip,

$$\eta_{chip} = \eta_{submm} \cdot \eta_{ohmic-loss} \tag{B.14}$$

where η_{submm} represents the efficiency of the sub-millimeter filter, $\eta_{radiation-loss}$ the radiation losses in the chip transmission lines. The power coupled to an MKID is then

$$P_{i-MKID} = \eta_{antenna}\eta_{chip} \int \frac{c^2}{\nu^2} \cdot L_{i-MKID}(\nu) \cdot P_{detector}(\nu)\, d\nu \tag{B.15}$$

For DESHIMA 1.0 the overall antenna and chip efficiency were found to be $\eta_{antenna}$=55% and an overall chip efficiency η_{chip}=7%. See [17] for more information on all efficiencies mentioned. For DESHIMA 2.0 $\eta_{antenna}$=45% and η_{chip} = 50% was assumed.

B.2.5. Simulated SNRs over measurement times

With the effective power reaching the MKIDs, one can calculate the signal-to-noise ratio (SNR) per MKID based on the noise equivalent power (NEP). The power when no gas is supplied $P_{0,\, i-MKID}$ is simulated by taking unitary gas transmission t_{gas} = 1 in equation B.9 instead of a gas spectrum by the AM Atmospheric Model. The NEP can then be calculated using the formula for photon noise limited MKIDs as described by Equation 2.29 to be

$$\mathrm{NEP}_{i-MKID} = \sqrt{2P_{0,\, i-MKID}\left(h\nu_0 + \frac{P_{0,\, i-MKID}}{\Delta\nu}\right) + 4\Delta E_{Al}\frac{P_{0,\, i-MKID}}{\eta_{pb}}} \quad \text{with} \quad \Delta\nu = \mathrm{FWHM} \cdot \frac{\pi}{2}, \tag{B.16}$$

where ΔE_{Al} is the aluminium gap energy, η_{pb} is the Cooper pair breaking efficiency and $\Delta\nu$ the effective band-with of the respective sub-millimeter filter.

With both the NEP and power from gas emission simulated per MKID one can find the SNR over integration time τ per MKID as

$$\mathrm{SNR}_{i-MKID}(\tau) = \sqrt{2\tau \cdot \eta_{chop}} \cdot \frac{P_{i-MKID}}{\mathrm{NEP}_{i-MKID}}, \tag{B.17}$$

where the square root of double the effective integration time is used since the NEP is defined for the inverse square root of a half second. The chopping efficiency η_{chop} represents the on-source efficiency due to the optical on- and off-source chopping during the measurement.

B.3. Simulating the Detector Output Profile

The simulated output by Karatsu's program can be compared to measured spectra to determine absolute frequency shifts in the terahertz frequency sweep measurement. This is achieved by comparing the measured results of a gas with simulated profiles for several absolute frequency shifts. This section will cover the steps taken to obtain the simulated spectrum. For the method to compare the simulated spectra with the detected spectrum, see section 4.4.

The process to obtain a simulated detected spectrum from a simulated gas emission spectrum can be split in four steps:

1. The AM Atmospheric Model is used to simulate the gas opacity spectrum.
2. The combined effective transmission of all quasi-optical filters and media is calculated for the cryostat system.
3. The MKID response obtained from the THz frequency sweep measurement is normalized to the wide-band filter response.
4. The detector output is calculated by convolution of the gas opacity with the detector and quasi-optical filterstack response.

Note that this calculation model is only considering the effect of the cryostat system and detector itself onto the emission spectrum, and not the impact of the gas cell setup. It assumes an ideal gas cell setup performance where the effective background behind the gas has a flat 77K brightness temperature.

B.3.1. Simulated gas opacity for the DESHIMA spectrum

This simulation step is identical to step 1 of subsection B.3. See the relevant subsection for more information.

B.3.2. Quasi-Optical Filterstack Transmission

The transmission through all filters and optical media from the HDPE cryostat window up until the detector is obtained by multiplying the transmittance profile of each subsequent component as

$$t_{filterstack}(f) = \prod_{layers} t_{layer}(f). \tag{B.18}$$

The filterstack used in the simulations for both the Hydra and Beast configuration ordered from outside the cryostat window up until the detector is formed by:

- 8 mm HDPE window
- 2x Goretex Foam
- 6x RTMLI
- Several low-pass filters (K2329, W963)
- A bandpass filter covering the DESHIMA frequency band (K1817)

See subsection 3.1.1 for more information on these filters. See Figure B.2 for the transmission profile for each layer and the combined product of all layers. Note that this calculation assumes no re-emittance of absorbed radiation and no reflections in between layers. In reality, the re-emission might add spectral features and reflections could cause optical resonance effects.

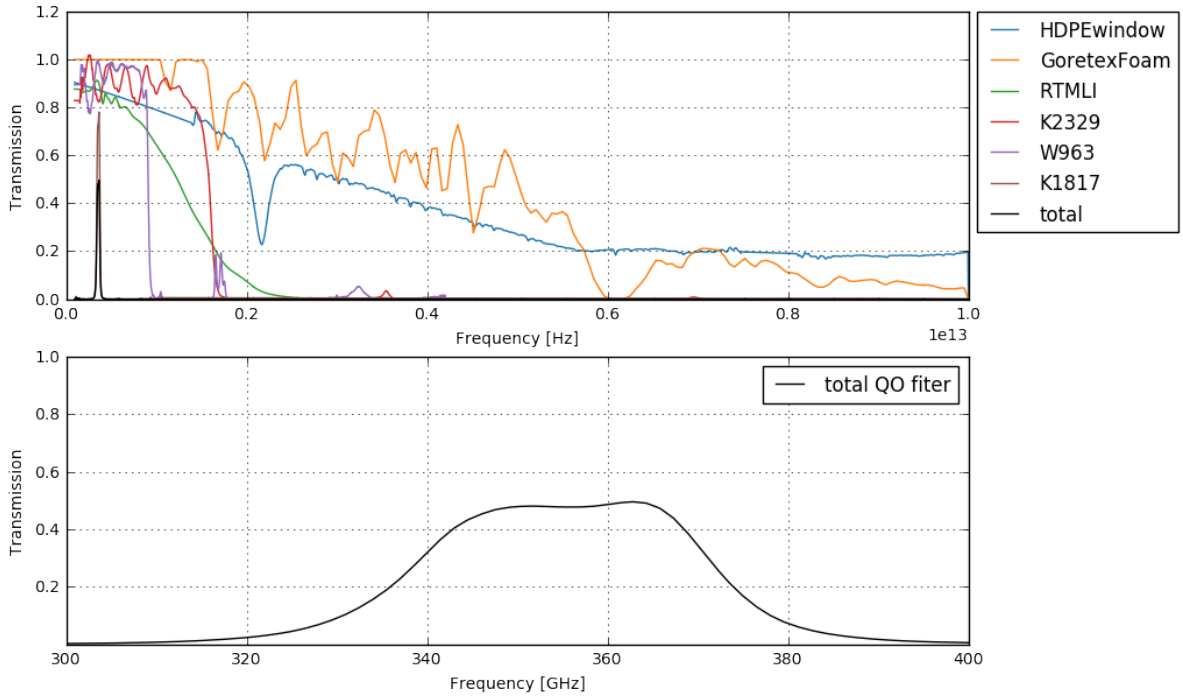

Figure B.2: The transmission spectra used for the cryostat filterstack. **Top** Individually measured layer transmittance of each layer used in the filterstack. **Bottom** Total combined quasi-optical transmission for the frequency band used in the simulations

B.3.3. MKID Spectrum Response

Both the sub-milimeter filter MKID spectra and the wideband spectrum are taken from a THz frequency sweep measurement. One can calculate the MKID brightness temperature response normalized for the wideband response as

$$R_{i-MKID}(f) = \frac{\mathcal{T}\{r_{i-MKID}(f)\}}{\mathcal{T}\{r_{wideband-MKID}(f)\}}, \tag{B.19}$$

where $\mathcal{T}\{r_{i-MKID}(f)\}$ represents the conversion of the MKID's relative frequency shift to brightness temperature. See Figure B.3 for a typical sub-mm filter MKID response profile, and the resulting wideband normalized response. Note, this MKID response calculation will follow any errors and uncertainties present in the THz frequency sweep measurement, as well as errors in the fit parameters obtained by the rotating grid measurement.

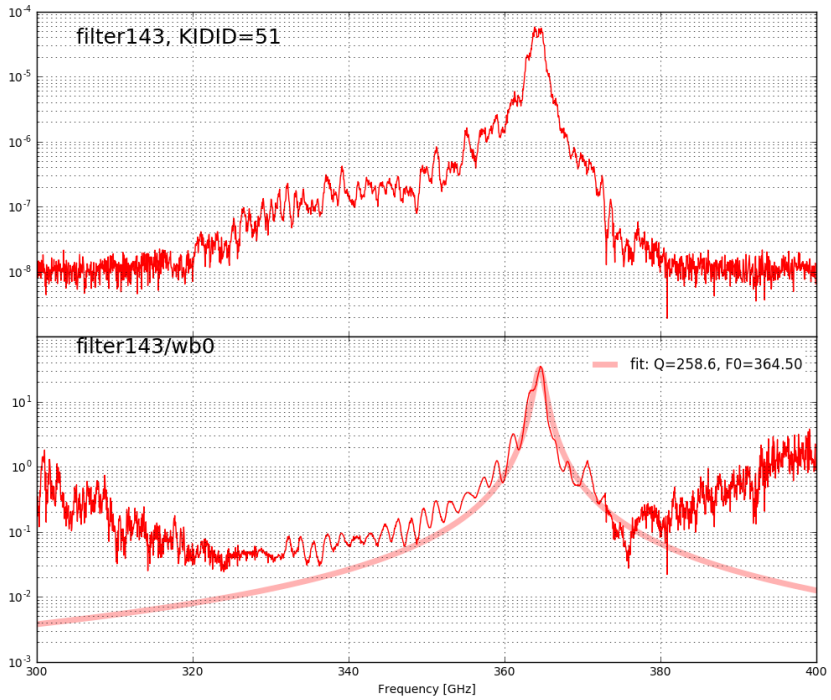

Figure B.3: Typical full frequency band MKID response profile for a terahertz frequency sweep measurement. **Top** Response for MKID ID 51 coupled to filter 143. **Bottom** The same response divided by the response obtained for another MKID coupled to a wideband filter. This normalized response is fitted to a Lorentzian shape to obtain the center frequency and quality factor.

B.3.4. Convolution of Gas Emission with System Transmission

The simulated output to the gas emission spectrum is calculated by convoluting the input emission with the MKID response and filterstack transmission. One can consider the convolution as applying two transfer functions: an MKID specific transfer function representing the MKID performance and corresponding filter behaviour, and a general transfer function representing the quasi-optical filterstack.

The general filterstack transfer function is calculated by normalizing the previous found total quasi-optical transmittance as

$$H_{filterstack}(f) = \frac{t_{filterstsck}(f)}{\max\{t_{filterstack}(f)\}}. \tag{B.20}$$

The MKID specific transfer function is calculated similarly by normalizing the MKID brightness temperature response as

$$H_{i-MKID}(f) = \frac{R_{i-MKID}(f)}{\max\{R_{i-MKID}(f)\}}. \tag{B.21}$$

The simulated output brightness temperature per MKID is now found by taking the sum of the input spectra convoluted with both transfer functions, as

$$T_{i-MKID} = \sum_{f} T_{signal}(f) \cdot H_{filterstack}(f) \cdot H_{i-MKID}(f) \tag{B.22}$$

Each MKID sub-mm filter has a corresponding center frequency found as well with the THz frequency sweep measurement. Using this, all simulated brightness temperatures can be linked to their center frequencies. See Figure B.4 for the simulated output.

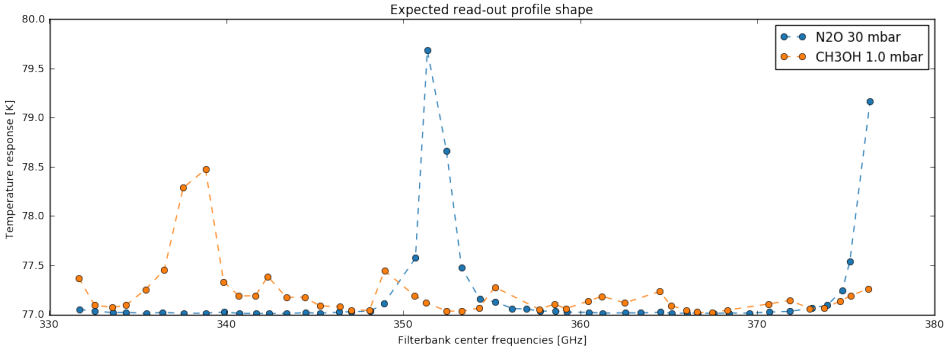

Figure B.4: Simulated output spectrum by the DESHIMA 1.0 detector for 30 mbar nitrous oxide and 1 mbar methanol.

C

Cracked Windows of First Fabrication Trial

A first fabrication trial with the anti-reflective pattern drilled into both sides of the TOPAS sheet resulted in circular cracks in the window close to opposing screw holes. Likely, too high loads were exerted onto the TOPAS material during fabrication, probably related to clamping the window during drilling using the holes. See figure C.1 for photographs of the fabricated window with the circular cracks. The figure as well shows a second photograph of the same window after vacuum testing. One can see the crack have enlarged, indicating the instabilities of these cracks and the potential risk of failing with continued use.

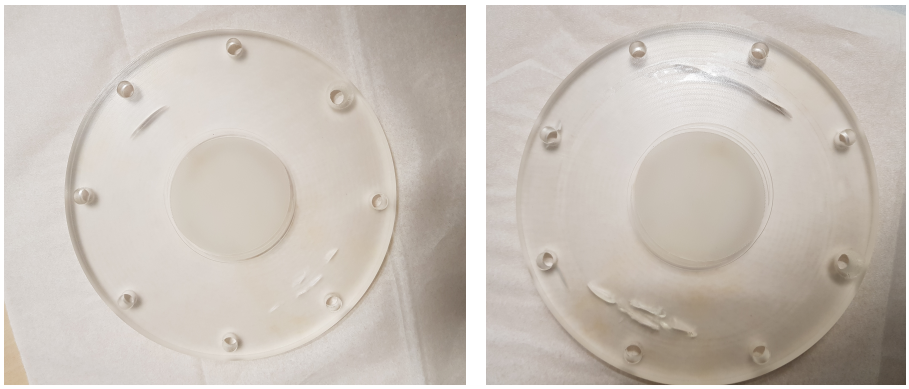

(a) (b)

Figure C.1: Photographs of the first trial to fabricate the designed anti-reflective pyramid grating onto the TOPAS window. (a) The window showed circular cracks after fabricating the grating. The cracks are located near the screwing holes which are believed to have been used as clamping points during drilling, indicating too much stress during fabrication. (b) The same TOPAS window after testing it in the gas cell for high vacuum. The increase of the cracks is visible, indicating the potential danger of cracks present in the windows.

D

Demodulation: Cross-Verification using the Hilbert Transform

The demodulation of the chopped data was done using the Fourier transform method as described in section 4.1. An alternative demodulation method based on the Hilbert transform was developed to cross-verify the performance of the Fourier transform demodulation method.

D.1. Demodulation using Hilbert Transform

The Hilbert Transform can be used to obtain the instantaneous amplitude of the chopped signal. This method is inspired by digital demodulation techniques of amplitude modulated signals. The Hilbert Transform of the input signal in combination with the original signal forms the complex valued analytical representation of the real valued input signal. This analytical representation can be used to find both the instantaneous envelope and instantaneous frequency, see as well figure D.1.

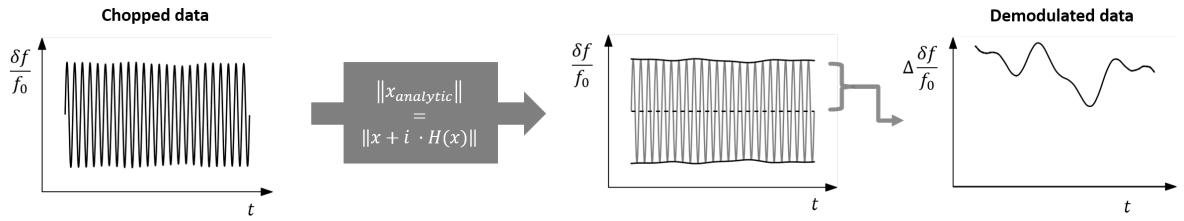

Figure D.1: Schematic of the demodulation method based on the Hilbert Transform. **Left** The optical chopper modulates the signal reaching the detector by rapidly alternating the on-source and off-source path. **Middle** The envelope of the modulated signal representing the instantaneous amplitude is calculated by taking the absolute value of the complex valued analytic signal. The definition of the analytic signal is presented in Eq. 4.26. **Right** The instantaneous envelope plotted together with the input signal. An additional plot of just the instantaneous amplitude is added to better illustrate the demodulated profile

The analytical representation $x_{analytic}$ and Hilbert Transform $\mathscr{H}$ of the input signal $x(t)$ are found as

$$x_{analytic} = \mathscr{F}^{-1}\{\mathscr{F}\{x\}\,2U(x)\} = x + i \cdot \mathscr{H}\{x\} \tag{D.1}$$

where $\mathscr{F}$ denotes the Fourier Transform and $U(x)$ the unit step function with its step at $x = 0$. The basic idea of this analytical representation is to drop the information of the negative frequencies in the frequency spectrum. Due to the symmetry of the spectrum, all its information is assumed to be also contained in the positive frequencies. This allows for combining the original signal as the real part and the half π phase shifted signal as the imaginary part in a single complex representation. The instantaneous amplitude can then be found in the absolute value of the analytic representation as

$$A_x(t) = \left|x_{analytic}(t)\right|, \tag{D.2}$$

the instantaneous (unwrapped) phase as

$$\phi_x(t) = \arg\{x_{analytic}(t)\}, \tag{D.3}$$

and the instantaneous frequency as

$$f(t) = \frac{1}{2\pi}\frac{d\phi_x(t)}{dt} \tag{D.4}$$

The main advantage of this approach compared to the Fourier Transform demodulation is the instantaneous sampling resolution. The analytical representation and its instantaneous amplitude and frequency retain the original sampling rate of the chopped input data. The Fourier Transform would downsample a time slice of half a second (600 samples) to a single value for a typical measurement with the gas cell setup. Note has to be taken that this instantaneous method is prone to noise. A high pass filter has to be applied first onto the instantaneous amplitude before further use. Alternative ways of reducing the noise impact on Hilbert Transform demodulation have also been found, by convolution with sinc functions [48].

This alternative demodulation method is generally not used in this research, as the Fourier Transform demodulation was found to be sufficient. This alternative's main use was in verifying the code implementation of the Fourier Transform demodulation method. An additional advantage was its high resolution of instantaneous frequency. The Fourier Transform demodulating method did not allow for a sufficient resolution of the carrier wave frequency over time to investigate the carrier frequency stability. The Hilbert Transform demodulating did and was used to analyse the chopper frequency stability, see Figure 3.7 in section 3.1.4.

D.2. Stability Impact of Demodulation Method

Figure D.2 and Table D.1 show the total deviation profiles and optima means of run 830 and 865 demodulated with both methods. Both show the original results and the results with removal of linear drifts in the time data. Note that the data presented here differs slightly from the data seen in 5.1 since the time data have been downsampled and the total deviation profile calculated for a lower resolution. Specifically, the data is downsampled 100x for the Hilbert method, where the Fourier method has a ~600x downsampling implemented due to the slicing mechanic. A 1000 data points long logarithmically spaced array from 10s to the total measurement time was used for the total deviation profile. This was done for improved computational speeds.

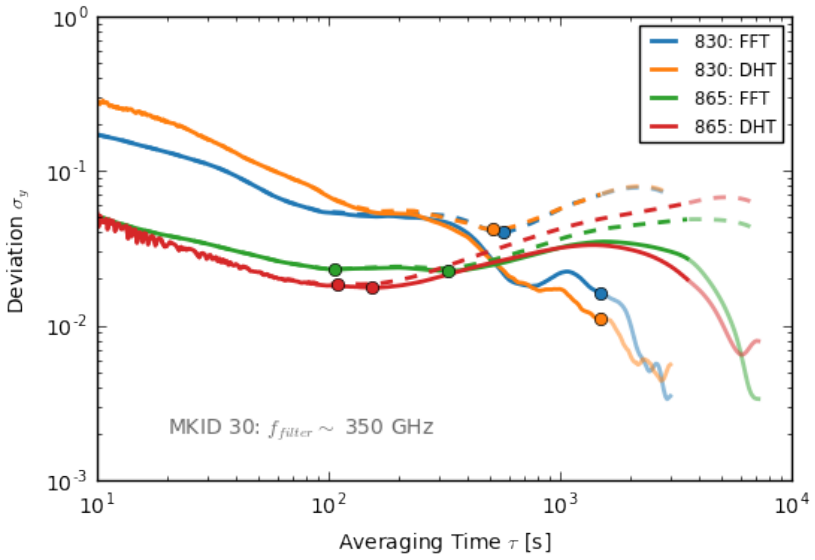

Figure D.2: Total deviation profiles for MKID 30 showing the behaviour when analysed with the Fourier transform demodulation method (FFT) or the Hilbert transform (DHT). Note that the FFT and DHT results are similar. The FFT method being slightly higher is believed to be due to the increased downsampling and averaging compared to the DHT method. **Solid lines**: The results with linear drifts removed. **Dashed lines**: Original results without post-processing after demodulation.

Since the demodulation methods performed reasonably similar, the Fourier transform demodulation method is not believed to induce unwanted aberrations. The Fourier transform method remained the main

Measurement	**Demod.**	**Mean Optimum τ (s)**	
		Original	**Drift removed**
830: w. snout, 3000s	FFT	675 ± 415	1421 ± 122
	DHT	788 ± 426	1466 ± 50
865: no snout, 7200s	FFT	189 ± 91	1529 ± 1631
	DHT	180 ± 495	1631 ± 1703

Table D.1: Mean optimum averaging time over all filterbank coupled MKIDs per measurement run either demodulated using the Fourier transform (FFT) or the Hilbert transform (DHT). In addition, the results after removal of linear drifts are included. The mean results do not indicate distinct deviations among the demodulation methods

demodulation method. Note, however, that the Hilbert transform does allow for total deviation analysis for averaging times as low as the original sampling frequency, where the Fourier method is limited by the slice-length used for a demodulated data point. This still made it a viable tool for verifying the performance of individual measurements, as well as checking the stability of the modulation frequency.

E

Impact of the Rotating Wire Grid Polarizer on the Spectrum

In the design of the setup, it is assumed that the two wire grids operate as a combined beam splitter and polarizer. In reality the wire grids are prone to absorption, inaccuracies, higher order reflections and diffraction. [61] [53] To assess the impact of the two wire grids on the setup, two subsequent measurements were done with and without the rotating wire grid. All other aspects of the setup were kept untouched, except for refilling of the liquid nitrogen background. Figure E.1 shows the two spectra and their difference. The difference in the spectra showed no distinct frequency dependent spectrum, only an overall ~7K offset. This overall offset is to be expected due to some absorption and thermal emission of the wire grid and the wire grid casing.

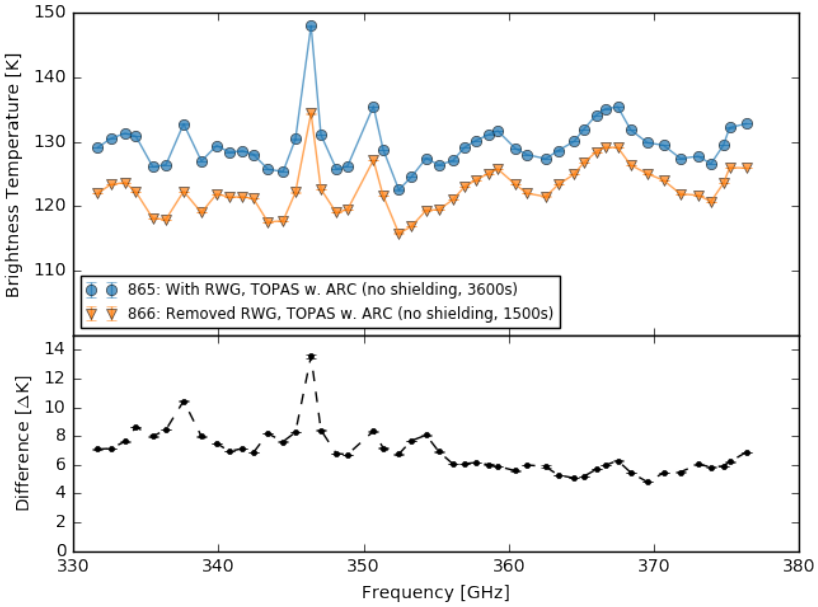

Figure E.1: Impact of the rotating wire grid polarizer (RWG) on the detected brightness temperature spectrum. Subsequent measurements with only the rotating wire grid either present or removed and otherwise no changes showed that the wire grid does not cause frequency dependent effects. Only an overall baseline difference was found. This overall difference is to be expected due to absorption of the wire grid as well as re-emitting of the wire grid and the wire grid casing. **Circles/Triangles**: Subsequent empty gas cell measurements with TOPAS windows and no magnetic shielding around the DESHIMA detector. Either the wire grid removed or present. **Dashed line**: The spectra subtracted for improved visual representation of the spectrum difference. The spectra difference slightly follows the overall contour of the measured spectra, but is mainly a stable difference of ~7 K.

Since no dominant frequency dependent effects are caused due to the wire grid polarizer, it is assumed that the wire polarizer is sufficiently stable for the setup. It is, however, interesting why the contour of the spectra can be seen in the difference of those spectra. This shows that somehow the profile shape is amplified

for the profile with a higher baseline. An explanation could be that the shape of these spectra is mainly formed by environmental radiation reflected into the setup. The addition of the wire grid increases the environmental reflection slightly, as such the difference in these spectra would as well show the increase in environmental reflections. Additional research into the environmental radiation would be required to make this conclusive.

F

Python Code Implementations

F.1. LMFIT Package: Least Squares Fitting in Python

All fitting described in this thesis was done using the LMFIT open source package for python [40]. The residual is calculated by subtracting the expected profile with altering parameters from the data and weighting it for the errors in the data. The best fit is determined by minimizing the residual using the least squares algorithm by LMFIT. LMFIT allows for extensive fitting customization. Care has to be taken in choosing the initial values and boundaries. The package approaches the minimization problem by departing locally from the initial values, and tends to find extraordinary results if the initial values are too far off. Human verification of the fit profiles is necessary.

F.2. AllanTools: Allan Deviation and Related Statistics in Python

The computations to obtain the Allan deviation and alike were done with the AllanTools python library. [57] This library integrates the fractional frequency data back to phase data and uses the respective phase data definitions of the deviations discussed in this section. The phase data definitions are generally faster to compute. After the phase data calculations, the phase data is differentiated back to fractional frequency.

Bibliography

[1] David W. Allan. Should the classical variance be used as a basic measure in standards metrology? *IEEE Transactions on Instrumentation and Measurement*, IM-36(2):646–654, jun 1987. ISSN 0018-9456. doi: 10.1109/TIM.1987.6312761. URL http://ieeexplore.ieee.org/document/6312761/.

[2] Marta Arias Campo. *On the Design of Fly's Eye Lenses at Sub-THz Frequencies for Wideband Communications*. Delft University of Technology, 2021. ISBN 9789055841745. doi: https://doi.org/10.4233/uuid:a9bb41e0-3d2a-4028-a218-bd85f2053545. URL https://doi.org/10.4233/uuid:a9bb41e0-3d2a-4028-a218-bd85f2053545.

[3] Marta Arias Campo, Giorgio Carluccio, Darwin Blanco, Simona Bruni, Oliver Litschke, and Nuria Llombart. Dielectric-Grating In-Lens Polarizer for Beyond 5G Communications. In *2019 44th International Conference on Infrared, Millimeter, and Terahertz Waves (IRMMW-THz)*, pages 1–2. IEEE, sep 2019. ISBN 978-1-5386-8285-2. doi: 10.1109/IRMMW-THz.2019.8874265. URL https://ieeexplore.ieee.org/document/8874265/.

[4] J. Benson, J. Fischer, and D. A. Boyd. Submillimeter and millimeter optical constants of liquid nitrogen. *International Journal of Infrared and Millimeter Waves*, 4(1):145–152, jan 1983. ISSN 0195-9271. doi: 10.1007/BF01008973. URL http://link.springer.com/10.1007/BF01008973.

[5] Jarosław Bomba, Jarosław Suszek, Michał Makowski, Artur Sobczyk, and Maciej Sypek. 3-D Printed Anti-Reflection Structures for the Terahertz Region. *Journal of Infrared, Millimeter, and Terahertz Waves*, 39 (1):24–35, jan 2018. ISSN 18666906. doi: 10.1007/s10762-017-0435-5. URL http://link.springer.com/10.1007/s10762-017-0435-5.

[6] Claudia Brückner, Boris Pradarutti, Olaf Stenzel, Ralf Steinkopf, Stefan Riehemann, Gunther Notni, and Andreas Tünnermann. Broadband antireflective surface-relief structure for THz optics. *Optics Express*, 15(3):779, 2007. ISSN 1094-4087. doi: 10.1364/OE.15.000779. URL https://www.osapublishing.org/oe/abstract.cfm?uri=oe-15-3-779.

[7] Claudia Brückner, Thomas Käsebier, Boris Pradarutti, Stefan Riehemann, Gunther Notni, Ernst-Bernhard Kley, and Andreas Tünnermann. Broadband antireflective structures applied to high resistive float zone silicon in the THz spectral range. *Optics Express*, 17(5):3063, mar 2009. ISSN 1094-4087. doi: 10.1364/OE.17.003063. URL https://www.osapublishing.org/oe/abstract.cfm?uri=oe-17-5-3063.

[8] J. Burnett, L. Faoro, I. Wisby, V. L. Gurtovoi, A. V. Chernykh, G. M. Mikhailov, V. A. Tulin, R. Shaikhaidarov, V. Antonov, P. J. Meeson, A. Ya Tzalenchuk, and T. Lindström. Evidence for interacting two-level systems from the 1/f noise of a superconducting resonator. *Nature Communications*, 5(1):4119, sep 2014. ISSN 2041-1723. doi: 10.1038/ncomms5119. URL http://www.nature.com/articles/ncomms5119.

[9] Bin Cai, Haitao Chen, Gongjie Xu, Hongwei Zhao, and Okihiro Sugihara. Ultra-Broadband THz Antireflective Coating with Polymer Composites. *Polymers*, 9(11):574, nov 2017. ISSN 2073-4360. doi: 10.3390/polym9110574. URL http://www.mdpi.com/2073-4360/9/11/574.

[10] Yuting W. Chen and Xi-Cheng Zhang. Anti-reflection implementations for terahertz waves. *Frontiers of Optoelectronics*, 7(2):243–262, jun 2014. ISSN 2095-2759. doi: 10.1007/s12200-013-0377-z. URL http://link.springer.com/10.1007/s12200-013-0377-z.

[11] J. Choi, H. Ishitsuka, S. Mima, S. Oguri, K. Takahashi, and O. Tajima. Radio-transparent multi-layer insulation for radiowave receivers. *Review of Scientific Instruments*, 84(11):114502, nov 2013. ISSN 0034-6748. doi: 10.1063/1.4827081. URL http://aip.scitation.org/doi/10.1063/1.4827081.

[12] Tamara M. Davis. Superluminal recession velocities. In *AIP Conference Proceedings*, volume 555, pages 348–351. AIP, 2001. doi: 10.1063/1.1363540. URL http://aip.scitation.org/doi/abs/10.1063/1.1363540.

[13] Peter K. Day, Henry G. LeDuc, Benjamin A. Mazin, Anastasios Vayonakis, and Jonas Zmuidzinas. A broadband superconducting detector suitable for use in large arrays. *Nature*, 425(6960):817–821, oct 2003. ISSN 0028-0836. doi: 10.1038/nature02037. URL http://www.nature.com/articles/nature02037.

[14] Pieter Jan de Visser. *Quasiparticle dynamics in aluminium superconducting microwave resonators*. Phd thesis, Delft University of Technology, 2014. URL https://repository.tudelft.nl/.

[15] J. A. Dobrowolski, Daniel Poitras, Penghui Ma, Himanshu Vakil, and Michael Acree. Toward perfect antireflection coatings: numerical investigation. *Applied Optics*, 41(16):3075, jun 2002. ISSN 0003-6935. doi: 10.1364/AO.41.003075. URL https://www.osapublishing.org/abstract.cfm?URI=ao-41-16-3075.

[16] Virgil-Florin Duma. Prototypes and modulation functions of classical and novel configurations of optical chopper wheels. *Latin American Journal of Solids and Structures*, 10(1):5–18, jan 2013. ISSN 1679-7825. doi: 10.1590/S1679-78252013000100003. URL http://www.scielo.br/scielo.php?script=sci_arttext&pid=S1679-78252013000100003&lng=en&tlng=en.

[17] Akira Endo, Kenichi Karatsu, Alejandro Pascual Laguna, Behnam Mirzaei, Robert Huiting, David J. Thoen, Vignesh Murugesan, Stephen J. C. Yates, Juan Bueno, Nuri van Marrewijk, Sjoerd Bosma, Ozan Yurduseven, Nuria Llombart, Junya Suzuki, Masato Naruse, Pieter J. de Visser, Paul P. van der Werf, Teun M. Klapwijk, and Jochem J. A. Baselmans. Wideband on-chip terahertz spectrometer based on a superconducting filterbank. *Journal of Astronomical Telescopes, Instruments, and Systems*, 5(03):1, jun 2019. ISSN 2329-4124. doi: 10.1117/1.JATIS.5.3.035004. URL http://dx.doi.org/10.1117/1.JATIS.5.3.035004.

[18] Akira Endo, Kenichi Karatsu, Yoichi Tamura, Tai Oshima, Akio Taniguchi, Tatsuya Takekoshi, Shin'ichiro Asayama, Tom J. L. C. Bakx, Sjoerd Bosma, Juan Bueno, Kah Wuy Chin, Yasunori Fujii, Kazuyuki Fujita, Robert Huiting, Soh Ikarashi, Tsuyoshi Ishida, Shun Ishii, Ryohei Kawabe, Teun M. Klapwijk, Kotaro Kohno, Akira Kouchi, Nuria Llombart, Jun Maekawa, Vignesh Murugesan, Shunichi Nakatsubo, Masato Naruse, Kazushige Ohtawara, Alejandro Pascual Laguna, Junya Suzuki, Koyo Suzuki, David J. Thoen, Takashi Tsukagoshi, Tetsutaro Ueda, Pieter J. de Visser, Paul P. van der Werf, Stephen J. C. Yates, Yuki Yoshimura, Ozan Yurduseven, and Jochem J. A. Baselmans. First light demonstration of the integrated superconducting spectrometer. *Nature Astronomy*, 3(11):989–996, nov 2019. ISSN 2397-3366. doi: 10.1038/s41550-019-0850-8. URL http://www.nature.com/articles/s41550-019-0850-8.

[19] Christian Enz and Assim Boukhayma. Recent trends in low-frequency noise reduction techniques for integrated circuits. In *2015 International Conference on Noise and Fluctuations (ICNF)*, pages 1–6. IEEE, jun 2015. ISBN 978-1-4673-8335-6. doi: 10.1109/ICNF.2015.7288622. URL http://ieeexplore.ieee.org/document/7288622/.

[20] Patricio A. Gallardo, Brian J. Koopman, Nicholas F. Cothard, Sarah Marie M. Bruno, German Cortes-Medellin, Galen Marchetti, Kevin H. Miller, Brenna Mockler, Michael D. Niemack, Gordon Stacey, and Edward J. Wollack. Deep reactive ion etched anti-reflection coatings for sub-millimeter silicon optics. *Applied Optics*, 56(10):2796, apr 2017. ISSN 0003-6935. doi: 10.1364/AO.56.002796. URL https://www.osapublishing.org/abstract.cfm?URI=ao-56-10-2796.

[21] Jiansong Gao. *The Physics of Superconducting Microwave Resonators*. Phd thesis, California Institute of Technology, 2008.

[22] S. C. O. Glover and M.-M. Mac Low. On the relationship between molecular hydrogen and carbon monoxide abundances in molecular clouds. *Monthly Notices of the Royal Astronomical Society*, 412(1):337–350, mar 2011. ISSN 00358711. doi: 10.1111/j.1365-2966.2010.17907.x. URL https://academic.oup.com/mnras/article-lookup/doi/10.1111/j.1365-2966.2010.17907.x.

[23] T. Guruswamy, D. J. Goldie, and S. Withington. Quasiparticle generation efficiency in superconducting thin films. *Superconductor Science and Technology*, 27(5):055012, may 2014. ISSN 0953-2048. doi: 10.1088/0953-2048/27/5/055012. URL https://iopscience.iop.org/article/10.1088/0953-2048/27/5/055012.

[24] S. Hähnle, J. Bueno, R. Huiting, S. J. C. Yates, and J. J. A. Baselmans. Large Angle Optical Access in a Sub-Kelvin Cryostat. *Journal of Low Temperature Physics*, 193(5-6):833–840, dec 2018. ISSN 0022-2291. doi: 10.1007/s10909-018-1940-1. URL https://doi.org/10.1007/s10909-018-1940-1http://link.springer.com/10.1007/s10909-018-1940-1.

[25] Peter C. Hargrave and Giorgio Savini. Anti-reflection coating of large-format lenses for sub-mm applications. In Wayne S. Holland and Jonas Zmuidzinas, editors, *Millimeter, Submillimeter, and Far-Infrared Detectors and Instrumentation for Astronomy V*, volume 7741, page 77410S, jul 2010. ISBN 9780819482310. doi: 10.1117/12.856919. URL http://proceedings.spiedigitallibrary.org/proceeding.aspx?doi=10.1117/12.856919.

[26] Ralph Hofferbert and Ulrich Groezinger. A cold focal plane chopper for Herschel-PACS-critical components and reliability. In R.A. Harris, editor, *Proceedings of the 9th European Space Mechanisms and Tribology Symposium, 19-21 September 2001, Liège, Belgium.*, pages 221 – 229, Noordwijk, Netherlands, 2001. ESA Publications Division. URL https://www.researchgate.net/publication/234211019.

[27] D.A. Howe. The total deviation approach to long-term characterization of frequency stability. *IEEE Transactions on Ultrasonics, Ferroelectrics and Frequency Control*, 47(5):1102–1110, sep 2000. ISSN 0885-3010. doi: 10.1109/58.869040. URL http://ieeexplore.ieee.org/document/869040/.

[28] D.A. Howe. Interpreting oscillatory frequency stability plots. In *Proceedings of the 2002 IEEE International Frequency Control Symposium and PDA Exhibition (Cat. No.02CH37234)*, pages 725–732. IEEE, 2002. ISBN 0-7803-7082-1. doi: 10.1109/FREQ.2002.1075976. URL http://ieeexplore.ieee.org/document/1075976/.

[29] D.A. Howe and T.K. Peppler. Very long-term frequency stability: estimation using a special-purpose statistic. In *IEEE International Frequency Control Sympposium and PDA Exhibition Jointly with the 17th European Frequency and Time Forum, 2003. Proceedings of the 2003*, pages 233–238. IEEE, 2003. ISBN 0-7803-7688-9. doi: 10.1109/FREQ.2003.1275095. URL http://ieeexplore.ieee.org/document/1275095/.

[30] D.A. Howe and T.N. Tasset. Theo1: characterization of very long-term frequency stability. In *18th European Frequency and Time Forum (EFTF 2004)*, pages 581–587. IEE, 2004. ISBN 0-86341-384-6. doi: 10.1049/cp:20040933. URL https://digital-library.theiet.org/content/conferences/10.1049/cp_20040933.

[31] David A. Howe. Frequency Stability. In *Encyclopedia of RF and Microwave Engineering*. John Wiley & Sons, Inc., Hoboken, NJ, USA, apr 2005. doi: 10.1002/0471654507.eme134. URL http://doi.wiley.com/10.1002/0471654507.eme134.

[32] Md Saiful Islam, Cristiano M. B. Cordeiro, Md J. Nine, Jakeya Sultana, Alice L. S. Cruz, Alex Dinovitser, Brian Wai-Him Ng, Heike Ebendorff-Heidepriem, Dusan Losic, and Derek Abbott. Experimental Study on Glass and Polymers: Determining the Optimal Material for Potential Use in Terahertz Technology. *IEEE Access*, 8:97204–97214, 2020. ISSN 2169-3536. doi: 10.1109/ACCESS.2020.2996278. URL https://ieeexplore.ieee.org/document/9097587/.

[33] Nur Ismail, Cristine Calil Kores, Dimitri Geskus, and Markus Pollnau. Fabry-Pérot resonator: spectral line shapes, generic and related Airy distributions, linewidths, finesses, and performance at low or frequency-dependent reflectivity. *Optics Express*, 24(15):16366, jul 2016. ISSN 1094-4087. doi: 10.1364/OE.24.016366. URL https://www.osapublishing.org/abstract.cfm?URI=oe-24-15-16366.

[34] R. M. J. Janssen, J. J. A. Baselmans, A. Endo, L. Ferrari, S. J. C. Yates, A. M. Baryshev, and T. M. Klapwijk. High optical efficiency and photon noise limited sensitivity of microwave kinetic inductance detectors using phase readout. *Applied Physics Letters*, 103(20):203503, nov 2013. ISSN 0003-6951. doi: 10.1063/1.4829657. URL http://aip.scitation.org/doi/10.1063/1.4829657.

[35] N. Küchler, D. D. Turner, U. Löhnert, and S. Crewell. Calibrating groundbased microwave radiometers: Uncertainty and drifts. *Radio Science*, 51(4):311–327, apr 2016. ISSN 0048-6604. doi: 10.1002/2015RS005826. URL https://onlinelibrary.wiley.com/doi/10.1002/2015RS005826.

[36] Hiroki Kutsuma, Makoto Hattori, Kenji Kiuchi, Satoru Mima, Taketo Nagasaki, Shugo Oguri, Junya Suzuki, and Osamu Tajima. Optimization of Geomagnetic Shielding for MKIDs Mounted on a Rotating Cryostat. *Journal of Low Temperature Physics*, 193(3-4):203–208, nov 2018. ISSN 0022-2291. doi: 10.1007/s10909-018-2036-7. URL https://doi.org/10.1007/s10909-018-2036-7.

[37] G. Maschwitz, U. Löhnert, S. Crewell, T. Rose, and D. D. Turner. Investigation of ground-based microwave radiometer calibration techniques at 530 hPa. *Atmospheric Measurement Techniques*, 6(10):2641–2658, oct 2013. ISSN 1867-8548. doi: 10.5194/amt-6-2641-2013. URL https://amt.copernicus.org/articles/6/2641/2013/.

[38] Benjamin A Mazin. *Microwave Kinetic Inductance Detectors*. Phd thesis, California Institute of Technology, 2004. URL https://thesis.library.caltech.edu/3910/.

[39] Mira Naftaly and Richard Dudley. Terahertz reflectivities of metal-coated mirrors. *Applied Optics*, 50(19):3201, jul 2011. ISSN 0003-6935. doi: 10.1364/AO.50.003201. URL https://www.osapublishing.org/abstract.cfm?URI=ao-50-19-3201.

[40] Matt Newville, Renee Otten, Andrew Nelson, Antonino Ingargiola, Till Stensitzki, Dan Allan, Austin Fox, Faustin Carter, Michał, Dima Pustakhod, Lneuhaus, Sebastian Weigand, Ray Osborn, Glenn, Christoph Deil, Mark, Allan L. R. Hansen, Gustavo Pasquevich, Leon Foks, Nicholas Zobrist, Oliver Frost, Alexandre Beelen, Stuermer, Kwertyops, Anthony Polloreno, Shane Caldwell, Anthony Almarza, Arun Persaud, Ben Gamari, and Benjamin F. Maier. LMFIT: Non-Linear Least-Square Minimization and Curve-Fitting for Python, 2014. URL https://zenodo.org/record/4516651.

[41] Tom Nitta, Shigeyuki Sekiguchi, Yutaro Sekimoto, Kenji Mitsui, Norio Okada, Kenichi Karatsu, Masato Naruse, Masakazu Sekine, Hiroshi Matsuo, Takashi Noguchi, Masumichi Seta, and Naomasa Nakai. Antireflection Coating for Cryogenic Silicon and Alumina Lenses in Millimeter-Wave Bands. *Journal of Low Temperature Physics*, 176(5-6):677–683, sep 2014. ISSN 0022-2291. doi: 10.1007/s10909-013-1059-3. URL http://link.springer.com/10.1007/s10909-013-1059-3.

[42] Scott Paine. The am atmospheric model, 2019. URL https://doi.org/10.5281/zenodo.640645.

[43] Scott N. Paine, David D. Turner, and Nils Küchler. Understanding Thermal Drift in Liquid Nitrogen Loads Used for Radiometric Calibration in the Field. *Journal of Atmospheric and Oceanic Technology*, 31(3):647–655, mar 2014. ISSN 0739-0572. doi: 10.1175/JTECH-D-13-00171.1. URL http://journals.ametsoc.org/doi/10.1175/JTECH-D-13-00171.1.

[44] Alejandro Pascual Laguna, Kenichi Karatsu, David Thoen, Vignesh Murugesan, Bruno Buijtendorp, Akira Endo, and Jochem Baselmans. Terahertz Band-Pass Filters for Wideband Superconducting On-chip Filter-bank Spectrometers. *IEEE Transactions on Terahertz Science and Technology*, X(X):1–1, 2021. ISSN 2156-342X. doi: 10.1109/TTHZ.2021.3095429. URL https://ieeexplore.ieee.org/document/9477186/.

[45] Daniel H. Raguin and G. Michael Morris. Antireflection structured surfaces for the infrared spectral region. *Applied Optics*, 32(7):1154, mar 1993. ISSN 0003-6935. doi: 10.1364/AO.32.001154. URL https://www.osapublishing.org/abstract.cfm?URI=ao-32-7-1154.

[46] Hemant Kumar Raut, V. Anand Ganesh, A. Sreekumaran Nair, and Seeram Ramakrishna. Anti-reflective coatings: A critical, in-depth review. *Energy & Environmental Science*, 4(10):3779, oct 2011. ISSN 1754-5692. doi: 10.1039/c1ee01297e. URL http://xlink.rsc.org/?DOI=c1ee01297e.

[47] William J Riley and David Howe. *Handbook of Frequency Stability Analysis*, volume 31. Special Publication (NIST SP), National Institute of Standards and Technology, Gaithersburg, MD, 2008. ISBN 3019753058. URL https://tsapps.nist.gov/publication/get_pdf.cfm?pub_id=50505.

[48] Indrajit G. Roy. On robust estimation of discrete Hilbert transform of noisy data. *GEOPHYSICS*, 78(6):V239–V249, nov 2013. ISSN 0016-8033. doi: 10.1190/geo2013-0007.1. URL https://library.seg.org/doi/10.1190/geo2013-0007.1.

[49] Gordon J. Stacey. THz Low Resolution Spectroscopy for Astronomy. *IEEE Transactions on Terahertz Science and Technology*, 1(1):241–255, sep 2011. ISSN 2156-342X. doi: 10.1109/TTHZ.2011.2159649. URL http://ieeexplore.ieee.org/document/6005346/.

[50] Ieee Standards and Coordinating Committee. *1139-2008 IEEE Standard Definitions of Physical Quantities for Fundamental Frequency and Time Metrology–Random Instabilities*. IEEE, 2009. ISBN 978-0-7381-6855-5. doi: https://doi.org/10.1109/IEEESTD.2008.4797525. URL https://ieeexplore.ieee.org/servlet/opac?punumber=4797523.

[51] Paul Szypryt. *Development of Microwave Kinetic Inductance Detectors for Applications in Optical to Near-IR Astronomy*. PhD thesis, University of California, 2017. URL http://web.physics.ucsb.edu/$\sim$bmazin/Papers/szypryt_dissertation.pdf.

[52] Tatsuya Takekoshi, Kenichi Karatsu, Junya Suzuki, Yoichi Tamura, Tai Oshima, Akio Taniguchi, Shin'ichiro Asayama, Tom J. L. C. Bakx, Jochem J. A. Baselmans, Sjoerd Bosma, Juan Bueno, Kah Wuy Chin, Yasunori Fujii, Kazuyuki Fujita, Robert Huiting, Soh Ikarashi, Tsuyoshi Ishida, Shun Ishii, Ryohei Kawabe, Teun M. Klapwijk, Kotaro Kohno, Akira Kouchi, Nuria Llombart, Jun Maekawa, Vignesh Murugesan, Shunichi Nakatsubo, Masato Naruse, Kazushige Ohtawara, Alejandro Pascual Laguna, Koyo Suzuki, David J. Thoen, Takashi Tsukagoshi, Tetsutaro Ueda, Pieter J. de Visser, Paul P. van der Werf, Stephen J. C. Yates, Yuki Yoshimura, Ozan Yurduseven, and Akira Endo. DESHIMA on ASTE: On-Sky Responsivity Calibration of the Integrated Superconducting Spectrometer. *Journal of Low Temperature Physics*, 199(1-2):231–239, apr 2020. ISSN 0022-2291. doi: 10.1007/s10909-020-02338-0. URL http://link.springer.com/10.1007/s10909-020-02338-0.

[53] Martin J. Tauc, Wataru Nakagawa, and Joseph A. Shaw. Influence of second-order reflections during polarimetric calibration with two wire-grid polarizers. *Optical Engineering*, 58(08):1, mar 2019. ISSN 0091-3286. doi: 10.1117/1.OE.58.8.082412. URL https://doi.org/10.1117/1.OE.58.8.082412.

[54] TOPAS Advances Polymers. TOPAS Product Catalog, 2019. URL https://topas.com/sites/default/files/PRODUCTS-E-28.04.20.pdf.

[55] Carole E. Tucker and Peter A. R. Ade. Thermal filtering for large aperture cryogenic detector arrays. In Jonas Zmuidzinas, Wayne S. Holland, Stafford Withington, and William D. Duncan, editors, *SPIE Astronomical Telescopes + Instrumentation, 2006, Orlando, Florida , United States*, page 62750T, jun 2006. doi: 10.1117/12.673159. URL http://proceedings.spiedigitallibrary.org/proceeding.aspx?doi=10.1117/12.673159.

[56] Joris van Rantwijk, Martin Grim, Dennis van Loon, Stephen Yates, Andrey Baryshev, and Jochem Baselmans. Multiplexed Readout for 1000-Pixel Arrays of Microwave Kinetic Inductance Detectors. *IEEE Transactions on Microwave Theory and Techniques*, 64(6):1876–1883, jun 2016. ISSN 0018-9480. doi: 10.1109/TMTT.2016.2544303. URL http://ieeexplore.ieee.org/document/7445881/.

[57] Anders E.E. Wallin, Danny C Price, Cantwell G Carson, and Frédéric Meynadier. AllanTools: Allan deviation calculation, apr 2014. URL https://pypi.org/project/AllanTools/.

[58] N. Wehres, J. Maßen, K. Borisov, B. Schmidt, F. Lewen, U. U. Graf, C. E. Honingh, D. R. Higgins, and S. Schlemmer. A laboratory heterodyne emission spectrometer at submillimeter wavelengths. *Physical Chemistry Chemical Physics*, 20(8):5530–5544, 2018. ISSN 1463-9076. doi: 10.1039/C7CP06394F. URL http://xlink.rsc.org/?DOI=C7CP06394F.

[59] Withawat Withayachumnankul, Bernd M. Fischer, Samuel P. Mickan, and Derek Abbott. Retrofittable antireflection coatings for T-rays. *Microwave and Optical Technology Letters*, 49(9):2267–2270, sep 2007. ISSN 08952477. doi: 10.1002/mop.22664. URL http://doi.wiley.com/10.1002/mop.22664.

[60] S. J. C. Yates, J. J. A. Baselmans, A. Endo, R. M. J. Janssen, L. Ferrari, P. Diener, and A. M. Baryshev. Photon noise limited radiation detection with lens-antenna coupled microwave kinetic inductance detectors. *Applied Physics Letters*, 99(7):073505, aug 2011. ISSN 0003-6951. doi: 10.1063/1.3624846. URL http://aip.scitation.org/doi/10.1063/1.3624846.

[61] X. J. Yu and H. S. Kwok. Optical wire-grid polarizers at oblique angles of incidence. *Journal of Applied Physics*, 93(8):4407–4412, apr 2003. ISSN 0021-8979. doi: 10.1063/1.1559937. URL http://aip.scitation.org/doi/10.1063/1.1559937.

[62] Xi Yu, Michiharu Ohta, Nobuhito Takizawa, Kazuhisa Mikame, Shingo Ono, and Jongsuck Bae. Femtosecond-laser-fabricated periodic tapered structures on a silicon substrate for terahertz antireflection. *Applied Optics*, 58(35):9595, dec 2019. ISSN 1559-128X. doi: 10.1364/AO.58.009595. URL https://www.osapublishing.org/abstract.cfm?URI=ao-58-35-9595.

[63] Zhongyue Zhang. *Gas Cell Experiment for the Calibration of DESHIMA (MSc Thesis)*. 2019. URL http://repository.tudelft.nl/.

[64] Guozhong Zhao, Maarten ter Mors, Tom Wenckebach, and Paul C. M. Planken. Terahertz dielectric properties of polystyrene foam. *Journal of the Optical Society of America B*, 19(6):1476, jun 2002. ISSN 0740-3224. doi: 10.1364/JOSAB.19.001476. URL https://www.osapublishing.org/abstract.cfm?URI=josab-19-6-1476.